THESIS FOR THE DEGREE OF DOCTOR OF PHILOSOPHY

CO Oxidation over Oxide Supported Platinum Catalysts

Mengqiao Di

Department of Chemistry and Chemical Engineering
CHALMERS UNIVERSITY OF TECHNOLOGY
Göteborg, Sweden 2023

CO Oxidation over Oxide Supported Platinum Catalysts

Mengqiao Di

ISBN 978-91-7905-804-3

Doktorsavhandlingar vid Chalmers tekniska högskola

Ny serie Nr. 5270

ISSN 0346-718X

Department of Chemistry and Chemical Engineering
Chalmers University of Technology
SE-412 96 Göteborg
Telephone +46 31 772 1000

Cover:
Cover Design is credited to Zhe Zhang

Printed by Chalmers Digitaltryck

Göteborg, Sweden 2023

CO Oxidation over Oxide Supported Platinum Catalysts

Mengqiao Di
Department of Chemistry and Chemical Engineering
Chalmers University of Technology

Abstract

Catalytic oxidation of carbon monoxide (CO) is one of the most studied reactions that still needs to be improved because of its practical use in the chemical industry including feedstock purification and applications such as emission control, in-door air cleaning, improvement of fuel cell efficiency etc. Concerning CO emissions, the transportation sector is a large contributor. The development of modern powertrains and driving patterns lead to cold exhausts. Thus catalysts must be active for CO oxidation at low temperatures, which is a challenge. Further, CO oxidation is influenced by other compounds in the exhausts that may either promote or inhibit essential catalytic functions. For combustion exhausts, water is definitely inevitable and nitrogen oxides are common components.

This work scrutinizes the kinetics of CO oxidation over Pt/alumina and Pt/ceria catalysts through analysis of reaction orders obtained experimentally from flow-reactor measurements and theoretically by kinetic Monte Carlo simulations, and connects this to kinetic model formulation. Further, the catalytic structure-function relationship is explored by *operando* infrared and X-ray absorption spectroscopy. The influence of water and nitrogen oxide on the CO oxidation kinetics is investigated with *in situ* infrared spectroscopy. Finally, iron oxide is explored as an active support for platinum with focus on the structural dynamics of Pt/FeO_x under reaction conditions.

The results show that reaction orders depend on reaction conditions and operating mechanism, and the adsorbate-adsorbate interactions plays a crucial role. Pt/ceria is active at lower temperatures than Pt/alumina thanks to lattice oxygen in the ceria support that participates according to a Mars-van Krevelen mechanism. This mechanism is promoted by water but inhibited by nitrogen oxide through nitrate formation. On Pt/alumina, the reaction proceeds via the Langmuir-Hinshelwod mechanism, which is also promoted by water and inhibited by nitrates. Finally, using iron oxide as support for Pt opens for a catalyst design with a support even more interacting with Pt than ceria in terms of redox properties at low temperatures.

Keywords: CO oxidation, low-temperature activity, active catalyst support, *operando* spectroscopy, nitrogen oxide inhibition, water promotion

Research is to see what everybody else has seen and to think about what nobody else has thought

—Albert Szent-Györgyi

List of Publications

This thesis is based on the following appended papers, referred to by Roman numerals in the text:

I. How does adsorbate-adsorbate interactions affect reaction orders for CO oxidation over Pt?

M. Di, N. Bosio, A. Schaefer, E. Dietze, M. Skoglundh, H. Grönbeck and P.-A. Carlsson
Manuscript.

II. Interface reactions dominate low-temperature CO oxidation activity over Pt/CeO_2

N. Bosio, M. Di, M. Skoglundh, P.-A. Carlsson and H. Grönbeck
The Journal of Physical Chemistry C **126** (2022) 16164-16171.

III. Chasing PtO_x species in ceria supported platinum during CO oxidation extinction with correlative *operando* spectroscopic techniques

M. Di, K. Simmance, A. Schaefer, Y. Feng, F. Hemmingsson, M. Skoglundh, T. Bell, D. Thompsett, L. I. Ajakaiye Jensen, S.- Blomberg and P.-A. Carlsson
Journal of Catalysis **409** (2022) 1-11.

IV. Influence of nitrogen oxide and water on carbon monoxide oxidation over highly dispersed platinum ceria catalysts

M. Di, A. Schaefer, F. Hemmingsson, M. Skoglundh, T. Bell, Y. Feng, D. Thompsett and P.-A. Carlsson
Manuscript

V. Design of iron oxide supported catalysts for low-temperature CO oxidation

M. Di, A. Schaefer, F. Hemmingsson, R. R. D. Silva, M. Skoglundh, Ann-Christin Dippel, Ida Gjerlevsen Nielsen and P.-A. Carlsson,
Manuscript

My Contributions to the Publications

Paper I

I planned, carried out and analysed all experiments except XRF measurements. I wrote the first draft the manuscript.

Paper II

I planned, carried out and analyzed all experiments. I wrote the first draft of the experimental section and co-authored the manuscript.

Paper III

I carried out all experimental work and data analysis except catalyst preparation and XRF measurements. I wrote the first draft of the manuscript and was responsible for the submission.

Paper IV

I carried out all experimental work and data analysis except catalyst preparation and XPS measurements. I wrote the first draft of the manuscript.

Paper V

I planned and carried out the physisorption, XRD, SEM, STEM, TPR, TPO measurements and analysed the corresponding data as well as the HE-XRD measurements. I wrote the first draft of the manuscript.

Additional publications which are not included in the thesis:

Synthesis and Characterization of Catalytically Active Au Core-Pd Shell Nanoparticles Supported on Alumina

Yanyue Feng, Andreas Schaefer, Anders Hellman,Mengqiao Di , Hanna Härelind, Matthias Bauer, and Per-Anders Carlsson

Langmuir, 38 **(2022)**, 12859–12870

Insight into hydrothermal aging effect on Pd sites over Pd/LTA and Pd/SSZ-13 as PNA and CO oxidation monolith catalysts

Aiyong Wang, Kristina Lindgren,Mengqiao Di , Diana Bernin, Per-Anders Carlsson, Mattias Thuvander and Louise Olsson

Applied Catalysis B: Environmental, 278 **(2020)**, 0926-3373

Explanation of anomalous rate capability enhancement by manganese oxide incorporation in carbon nanofiber electrodes for electrochemical capacitors

Qi Li, Volodymyr Kuzmenko, Mohammad Mazharul Haque,Mengqiao Di, Anderson David Smith, Per Lundgren and Peter Enoksson

Electrochimica Acta, 340 **(2020)**, 0013-4686

Contents

List of Publications vii

Contents xi

Abbreviations, acronyms and terms xvii

1 Introduction 1
- 1.1 Emission concerns and environmental protection . . . 1
- 1.2 Why catalysis is important? . . . 2
- 1.3 Motivation of the thesis . . . 3

2 Background 5
- 2.1 Principles of heterogeneous catalysis . . . 5
- 2.2 CO oxidation on platinum . . . 6
- 2.3 CO oxidation on supported Pt . . . 7
- 2.4 Development of CO oxidation catalysts . . . 10
- 2.5 Specific objective . . . 10

3 Catalytic synthesis and characterisation methods 13
- 3.1 Catalyst synthesis . . . 13
- 3.2 Flow reactor measurements . . . 14
  - 3.2.1 Reactor configuration . . . 14
  - 3.2.2 Mass spectrometry . . . 16
  - 3.2.3 Data evaluation . . . 17
- 3.3 Gas Sorption . . . 19
  - 3.3.1 Physisorption . . . 19
  - 3.3.2 Chemisorption . . . 20
- 3.4 Electron microscopy . . . 22
  - 3.4.1 Scanning electron microscopy . . . 22
  - 3.4.2 Transmission electron microscopy . . . 22
- 3.5 Spectroscopy . . . 24
  - 3.5.1 Infrared spectroscopy . . . 24
  - 3.5.2 X-ray absorption spectroscopy . . . 28
- 3.6 Scattering . . . 31
  - 3.6.1 X-ray diffraction . . . 32
  - 3.6.2 High-energy X-ray diffraction . . . 32

4 Results and discussion 35
- 4.1 Catalyst physicochemical properties . . . 35
- 4.2 Kinetic behaviour . . . 39
  - 4.2.1 Ignition and extinction behaviours . . . 39
  - 4.2.2 Linking to microscopic reaction mechanisms . . . 40
- 4.3 Catalytic functionality . . . 43

4.3.1 Evolution of surface species 43
4.3.2 Local structure and long-range order 52
4.4 How to design CO oxidation catalysts? 57

5 Conclusions and future work **59**
5.1 Extended understanding on industrial relevant catalysts 60
5.2 Further improvements in catalytic design 60

Bibliography **63**

List of Figures

1.1 Diagram of historical development of catalysis based on specific achievements. 3

2.1 Potential energy diagram of a catalytic reaction (solid line) and homogeneous reaction (dashed line), where E^a, E^r, E^d and E^h are the activation energy barrier for adsorption, reaction, desorption and homogeneous reaction, respectively. 5
2.2 Scheme of catalytic performance of different catalysts for CO oxidation. 10
2.3 Structure of the appended papers for the objective of the thesis. . 11

3.1 A schematic representation of the support material before and after loading the precursor material by incipient wetness impregnation and freeze drying. 13
3.2 A schematic setup of flow reactor for CO oxidation, where MFC represents for mass flow controller, PG, for pressure gauge, PSU, for power supply unit, MS, for the mass spectrometer. The setup design is credited to Felix Hemmingsson. 14
3.3 A schematic setup of flow reactor for CO/H_2O and CO/NO oxidation, where MFC is for mass flow controller, PG, for pressure gauge, MS, for the mass spectrometer. The setup design is credited to Felix Hemmingsson. 15
3.4 A schematic representation of transport processes on porous catalysts, where R and P represent reactants and products, respectively. 17
3.5 N_2 adsorption (solid line) and desorption (dash line) isotherms of Pt/alumina. 19
3.6 BET plot of Pt/alumina. 20
3.7 CO adsorption isotherms at 35 °C for Pt/alumina. Blue squares describe the first analysis containing *physisorption* and *chemisorption*, and the black ones depict only *physisorption* in the repeated analysis. The orange ones give the chemisorption after the subtraction of the repeated analysis from the first one. 20
3.8 The incident electrons interact with the sample, where different types of electrons are produced from different sample volumes. . 22
3.9 Simplified TEM scheme. 23
3.10 Simplified STEM scheme. 23
3.11 TEM (a) and STEM (b) image of Pt/alumina. 23
3.12 Normal modes of vibration of linear and bent YXY, and planar XY_3 molecules. O and X represent the molecules vibrating perpendicular to the plane upward and downward. 25

3.13 Adsorption configurations of surface carbonates with related species, surface nitrates with related species on metal oxides, as well as CO adsorption configuration on metals or metal oxides, where H represents for a hydrogen atom, O, for an oxygen atom, C, for a carbon atom, N, for nitrogen atom and M, for metal oxides and/or metals. 26
3.14 A schematic setup of DRIFTS, where M abbreviates for mirror with a movable mirror of M4, BS, for beam splitter, and MCT, for mercury-cadmium-telluride, FS, for fast switch, MFC, for mass flow controller, and MS, for the mass spectrometer. The setup design is credited to Felix Hemmingsson. 27
3.15 Infrared spectrum of CO adsorbed on Pt/alumina. 28
3.16 A schema of multiple events after X-ray absorption. 29
3.17 X-ray absorption spectroscopy (XAS) spectra of PtO_2 powder sample in *fluorescence* mode (a) and its Fourier transformation with a fit (b). 30
3.18 Scheme of Bragg's law. 32

4.1 XRD patterns of the spent Pt/ceria in (a) and Pt/alumina in (b) after CO oxidation with H_2O (blue) and NO (orange), and as-prepared Pt/ceria and Pt/alumina catalysts (black). Reflection assignments are assigned using reference patterns (blue) from the Powder Diffraction File^{TM} (PDF) database for CeO_2 (PDF 00-004-0593) and γ-Al_2O_3 (PDF 00-010-0425). 36
4.2 High-resolution TEM and STEM-HAADF micrographs of the as-prepared Pt/ceria (panel a) and Pt/alumina (panel b), the spent Pt/ceria (panel c) and Pt/alumina (panel d) catalysts after CO oxidation with H_2O, and the spent Pt/ceria (panel e) and Pt/alumina (panel f) after CO oxidation with NO. 37
4.3 XRD patterns of the iron oxide without calcination and calcined at different temperatures, and subsequent calcination at different temperatures after loading Pt. Reflection assignments are assigned using reference patterns from the Powder Diffraction File^{TM} (PDF) database for Pt (PDF 00-004-0802), magnetite (PDF 00-065-0731), and hematite (PDF 04-003-2900). 38
4.4 Ignition (dashed lines) and extinction (solid lines) profile over Pt/ceria (panel a) and Pt/alumina (panel b) for dry CO oxidation (black) with 0.2 vol.% CO and 1 vol.% O_2, CO oxidation with 2 vol.% H_2O (blue) and 300 ppm NO (orange). Ignition profile over Pt/ceria (panel c) and Pt/alumina (panel d) with pre-adsorbed H_2O (blue) and NO (orange) followed by dry CO oxidation with 0.2 vol.% CO and 1 vol.% O_2. 39
4.5 CO and O_2 pressure dependencies of the turnover frequency over Pt/ceria (panel a) performed at 125 °C and Pt/alumina (panel b) at 145 °C. The reaction orders were obtained by linear fitting. . . 40

4.6 CO, O_2 and H_2O pressure dependencies of the reaction rates over Pt/ceria (panel a,b) performed at 45 °C and Pt/alumina (panel c,d) at 127 °C. The reaction orders were obtained by linear fitting. . . 41
4.7 *Operando* spectroscopic results for Pt/ceria (panel a,b) and Pt/alumina (panel c,d) during catalytic CO oxidation extinction. CO_2 gas phase spectra with noted CO conversions measured with mass spectrometry (panel a,c) and spectral region for CO adsorbed on Pt (panel b,d) with sample temperatures in °C in presence of 0.2 vol.% CO and 1 vol.% O_2. 44
4.8 *In situ* infrared difference spectra (hydrogen treated sample as reference) collected at indicated sample temperatures while increasing (panel a and c) and decreasing (panel b and d) the sample temperature in steps in the presence of 0.2 vol.% CO, 1 vol.% O_2 and 2 vol.% H_2O (Ar as balance). The measured global CO conversion is indicated at each temperature. 46
4.9 CO oxidation with NO from Pt/ceria (panel a) and Pt/alumina (panel b) at 35 °C with time-resolved spectral region for CO adsorbed on Pt and nitrates/carbonates. This is followed by increasing (panel a and c) and decreasing (panel b and d) the sample temperature in steps in the presence of 0.2 vol.% CO, 1 vol.% O_2 and 300 ppm NO Ar as balance). 49
4.10 XANES spectra (panel a,c) and FT k^2-weighted EXAFS spectra with corresponding CO conversions (panel b,d) in the presence of 5 vol.% CO and 5 vol.% O_2. The spectrum for PtO_2 and Pt black were recorded *ex-situ* in ambient air at room temperature as a reference. 52
4.11 The whiteline intensity (WLI) for Pt/alumina and Pt/ceria (panel a) against temperature, coordination number (CN), and radial distance (R) without phase correction for Pt-O and Pt-Pt scattering of Pt/ceria (panel b) and Pt/alumina (panel c and d). 53
4.12 *in-situ* HEXRD of 2 vol.% O_2 and 2 vol.% H_2 pulsing at 350 °C (panel a,b,e,f), and O_2 modulation with 1 vol.% CO and 4 vol.% O_2 (panel c,d,g,h) over Pt/maghemite and Pt/hematite. 56

List of Tables

1.1 EU emission standards for light-duty vehicles M_1, table reproduced from [7]. 1

4.1 Specific surface area (SSA) of catalysts and metal (SSA_{Pt}), Pt loading (X_{Pt}), metal dispersion (D_{Pt}), Pt particle size (d_{Pt}), and support particle size ($d_{support}$) for Pt/ceria and Pt/alumina. 35

4.2 Reaction orders over Pt_{small}/alumina and Pt_{large}/alumina under lean and rich conditions. 43
4.3 Assignment of Species in wavenumber range of 1000-2200 cm^{-1} the over Pt/ceria and Pt/alumina during CO/NO oxidation . . . 50

Abbreviations, acronyms and terms

δ bending stretch

ν_{as}) asymmetric stretch

ν_s) symmetric stretch

$\tilde{\nu}$ wavenumber

$\tilde{\nu}^{CO}$(Ce^{3+}) wavenumber of CO adsorption on reduced ceria

$\tilde{\nu}_{CO_2}$) wavenumber of carbon dioxide stretch

$\tilde{\nu}_{br}^{CO}$(Pt) wavenumber of bridge bonded CO adsorption on reduced Pt particles

$\tilde{\nu}_{br}^{NO}$(Pt0) wavenumber of bridge bonded CO adsorption on reduced Pt particles

$\tilde{\nu}_{lin}^{CO}$(Pt^0) wavenumber of linear CO adsorption on reduced Pt particles

$\tilde{\nu}_{lin}^{CO}$(Pt^{2+}) wavenumber of linear CO adsorption on oxidised Pt particles

$\tilde{\nu}_{lin}^{CO}$($Pt^{\delta+}$) wavenumber of linear CO adsorption on partially oxidised Pt particles

$\tilde{\nu}_{lin}^{CO}$(Pt(OH)) wavenumber of linear CO adsorption on Pt particles surrounded by OH

$\tilde{\nu}_{lin}^{CO}$(Pt-Ce^{3+}) wavenumber of CO adsorbed on interface site of Pt/ceria

$\tilde{\nu}_{lin}^{NO}$(Pt^{2+}) wavenumber of linear NO adsorption on oxidised Pt particles

$\tilde{\nu}_{NCO}$) wavenumber of isocyanate stretch

ADF Annular Dark-Field

b-X X adsorbed in bidentate configuration

BF Bright-Field

br-X X adsorbed in bridged configuration

BSE back scattered electrons

CEM Controlled Evaporation Mixer

DF Dark-Field

DFT Density Functional Theory

DRIFTS Diffuse Reflectance Infrared Fourier Transform Spectroscopy

EDX Energy-Dispersive X-ray Spectroscopy

EELS Electron Energy Loss Spectroscopy

EXAFS Extended X-ray Absorption Fine Structure

FTIR Fourier Transformed Infrared

HAADF High-Angle Annular Dark-Field

HEXRD High Energy X-ray Diffraction

HRTEM High Resolution Transmission Electron Microscopy

IWI Incipient Wetness Impregnation

l-MFCs Liquid Mass Flow Controllers

lin-X-Y X linearly adsorbed on Y

m-X X adsorbed in monodentate configuration

MARI Most Abundant Reaction Intermediate

MFCs Mass Flow Controllers

MS Mass Spectrometry

p-X X adsorbed in polydentate configuration

PFR plug flow reactor

PSD Pore Size Distribution

SAD Selected-Area Diffraction

SE secondary electrons

SEM Scanning Electron Microscopy

SSA Specific Surface Area

STEM Scanning Transmission Electron Microscopy

STP Standard Temperature and Pressure

TEM Transmission Electron Microscopy

TEM/EDX Transmission Electron Microscopy/Energy-dispersive X-ray spectroscopy

TOF turnover frequency

WLI Whiteline Intensity

XAFS X-ray Absorption Fine Structure

XANES X-ray Absorption Near Edge Structure

XAS X-ray Absorption Spectroscopy

XPS X-ray Photoelectron Spectroscopy

XRD X-ray diffraction

1 Introduction

1.1 Emission concerns and environmental protection

1.1 Emission concerns and environmental protection 1
1.2 Why catalysis is important? 2
1.3 Motivation of the thesis 3

Fossil fuels have been through large-scale exploitation since the industrial revolution until nowadays. Combustion is the most common way of converting chemically stored energy in fossil fuels to other forms. Carbon dioxide (CO_2) and water (H_2O) are the major products from the burning of fossil fuels but unburned hydrocarbons (HC), oxygenates and carbon monoxide (CO) are also generated due to incomplete combustion [1, 2]. In addition, as impurities in the fuels are burned as well, sulfur oxides (SOx) and nitrogen oxides (NOx) are produced during the combustion. The emissions from the combustion of fossil fuels cause climate, environmental, and health problems. Increased global warming is in part due to the depletion of non-renewable sources [3, 4] forming CO_2 emissions. Lower CO_2 emissions can only be achieved by decreasing the usage of fossil fuels and substituting with renewable sources [5]. Among the pollutants, CO and NOx are toxic to humans even at low concentrations [6]. Moreover, the interaction between hydrocarbons and NOx under sunlight can produce photochemical smog including ground-level ozone which is detrimental to most of living species.

Table 1.1: EU emission standards for light-duty vehicles M_1, table reproduced from [7].

Stage	CO	HC	HC+NOx	NOx	PM	PN
Positive Ignition (Gasoline)			g/km			
Euro 1	2.72		0.97			
Euro 2	2.2		0.5			
Euro 3	2.30	0.20		0.15		
Euro 4	1.0	0.10		0.08		
Euro 5	1.0	0.10		0.06	0.005	
Euro 6	1.0	0.10		0.06	0.005	6.0×10^{11}[a]
Compression Ignition (Diesel)						
Euro 1	2.72		0.97		0.14	
Euro 2	1.0		0.7		0.08	
Euro 3	1.0		0.56	0.50	0.05	
Euro 4	0.64		0.30	0.25	0.025	
Euro 5a	0.50		0.23	0.18	0.005	
Euro 5b	0.50		0.23	0.18	0.005	6.0×10^{11}
Euro 6	0.50		0.17	0.08	0.005	6.0×10^{11}

[a] only to DI engines

The transportation sector is one of the major consumers of fossil fuels and a significant contributor to atmospheric pollution. Around 30% of the global primary energy demand and around 50% of the global diesel consumption occurs within the transportation

sector [8]. Furthermore, the transportation sector contributes to around 30% of the global greenhouses gas (GHG) emissions, 77% of CO emissions, 50% of NOx emissions, 12% of SOx, and 7% of particulate matter (PM) [9]. It is estimated that 6.5 million of deaths globally are caused by air pollution [10]. This drives the regulation of vehicle emissions through legislation on specific emissions. The first legislation was initiated in California (1966) to limit the CO and HC emissions from vehicles [11]. Nowadays, more strict regulations are introduced by the California Air Resources Board (CARB) in order to achieve zero emissions from vehicles [12]. In Europe, similar legislations are introduced and the emission standards for light-duty vehicles, including passenger cars and light commercial vehicles, are summarized in Table 1.1. The introduction of PM standards for gasoline engines with positive ignition starts from Euro 5, which is equivalent to the situation for diesel. The particle number (PN) emission is further imposed in Euro 5/6. Moreover, Real Driving Emissions (RDE) with a portable emission monitoring system (PEMS) and On-Board Diagnostics (OBD) are required for the emission testings, which makes the measurements more accurate and closer to reality. Recently, the upcoming emission standards, Euro 7, have been proposed with more stringent requirements on emissions, a broader range of conditions for RDE testings including cold emissions, and longer after-treatment system durability [13]. In order to meet future legislation, the development of more effective catalytic after-treatment systems able to operate at low temperatures is needed.

1.2 Why catalysis is important?

Chemical reactions depend on temperature, concentration, pressure, and residence time [14]. Increasing temperature and the pressure will shift the thermodynamic equilibrium, which sometimes can be used to shift a reaction towards the product side. Catalysts make it possible to operate the reactions in the thermodynamically favorable regime at much lower temperatures (and reactant pressures), and increase the rate of the reaction by orders of magnitude. Chemical processes can therefore become more economical, especially when combined with optimized reactors and plant designs [15]. Catalysis, however, is more than that. The history of catalysis development can be divided into five time periods, each associated with specific achievements as summarized in Figure 1.1. In 1835, Jöns Jacob Berzelius systematically discovered and documented observations of catalytic phenomena and defined such reactions to be driven by a catalytic force, i.e., catalysis [14, 16]. This was followed by not only new discoveries of the new catalytic processes but also an increased understanding (interpretation) in

terms of the kinetics of chemical reactions in the development of catalysis [17]. After the practical implementation of catalysts in industrial processes for the manufacture of bulk chemicals, it became obvious that this means considerable economic benefits, for example, the significant expansion in sulfuric acid production [16]. Noteworthy to mention is that the technology for fixation of nitrogen from the air to produce fertilizers led to the growth in population [14, 18]. However, ammonia also turned out to be the major bulk chemical that allowed for the production of explosives, and thus it played a significant role in the First World War [19]. When the need for explosives became less urgent, catalytic processes shifted to the synthetic fuel processes, e.g., Fisher-Tropsch and Fluid Catalytic Cracking processes, due to the demand for the fuels to the fighters during the Second World War [11, 20]. The development of the automobile industry after the war increased the demand for petroleum, not only for fuels but also for polymers. Nowadays, the development of catalysis is not only economical but also largely driven by environmental concern and climate change based on emission control and renewable energy processes.

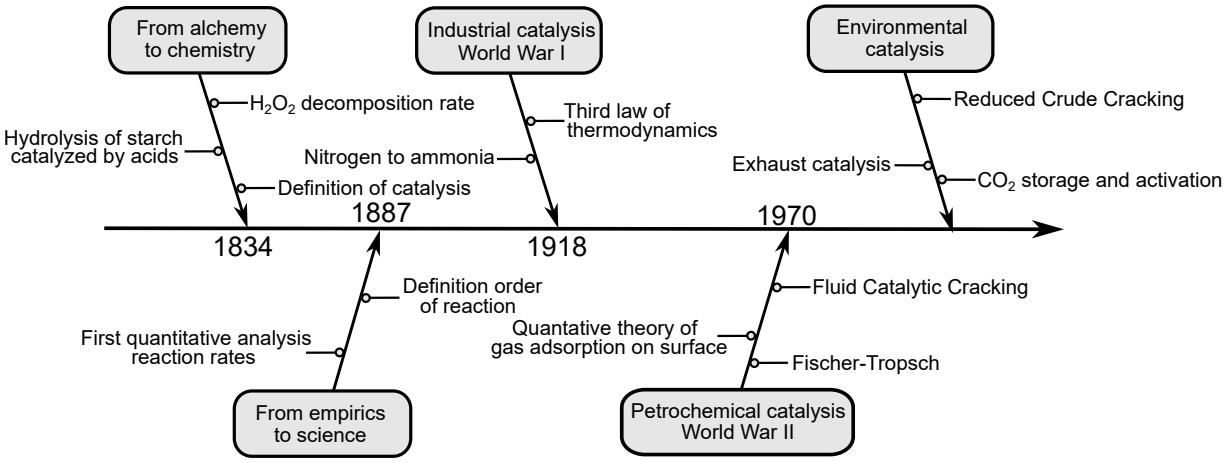

Figure 1.1: Diagram of historical development of catalysis based on specific achievements.

1.3 Motivation of the thesis

One of the important applications of catalysis is for automotive emission control. The catalytic converter is a good example of the possibility of adapting the technology construction from large-scale industrial processes to new smaller-scale applications [14]. The three-way catalytic converter (TWC) is generally used for after-treatment of emissions, i.e., CO, NOx and HCs, from stoichiometric engine exhausts [21]. Still, the efficiency, or full functionality, of TWCs at low temperatures needs to improve as to meet new efficient combustion engines and/or electrical hybridisation [22]. The

challenges at low temperatures are not only the cold-start period during the start-up of vehicles but also during the deceleration and the off-road driving pattern including the start-and-stop engine operation and switching between different propulsion modes [23, 24].

This thesis focuses on the investigation of the kinetic bottlenecks for oxidation of CO over catalysts prepared using industrially relevant methods. The reaction is studied in absence and presence water and nitrogen oxide.

Background 2

2.1 Principles of heterogeneous catalysis

2.1 Principles of heterogeneous catalysis 5
2.2 CO oxidation on platinum 6
2.3 CO oxidation on supported Pt 7
2.4 Development of CO oxidation catalysts . . . 10
2.5 Specific objective 10

The concept of heterogeneous catalysis means that the catalyst is in a different phase compared to that of reactants and products. For automotive exhaust aftertreatment systems, the catalysts are solids, while the reactants are in a fluid phase, often gaseous species. A catalyst facilitates a chemical reaction without being consumed itself. By stabilizing reaction intermediates and creating alternative reaction paths that are energetically favorable and the speed of the reaction increases [11, 25]. A catalytic cycle starts from the bond formation between reactants and the catalyst surface, termed adsorption, and then proceeds with the reaction between adsorbed reactants to form products, which detach from the catalyst surface, called desorption. This closes the catalytic cycle and leaves the catalysts in a state equal to their initial state. The reaction accelerated by the catalyst can be visualized by the potential energy diagram as shown in Figure 2.1. Each elementary step is correlated with an activation barrier. The formation of the bonding of the reactants is exothermic for a spontaneous reaction, which leads to lower energy. The activation barrier, $\triangle E_{cat}$ for the reaction between adsorbed reactants on the catalyst surface is significantly lower than the homogeneous gas phase reaction. Eventually, the desorption of products from the catalyst surface is involved in an endothermic process. As can be seen, the overall enthalpy change is the same for the catalytic and the uncatalyzed reaction leading to unaltered free energy, and thus a catalyst only promotes the kinetics but not thermodynamics [11, 25].

From the figure, one can also sense that the bonding between the reactants and the surface should be neither too weak nor too strong [15]. When the bonding is too weak, the reaction is similar to the homogeneous reaction with a high activation barrier, and thus barely any conversion to products can be observed. When the bonding is too strong for one of the reactants, the catalyst surface is mainly occupied by that reactant, and the other reactant has no place to adsorb on, thus no reaction. This is also called self-poisoning. When both reactants are strongly adsorbed, the intermediate becomes too stable to react. When the product is strongly adsorbed, the desorption becomes difficult to recover the catalyst surface for the next catalytic cycle. Therefore, the factors governing the overall reaction kinetics can be summarized as [26]:

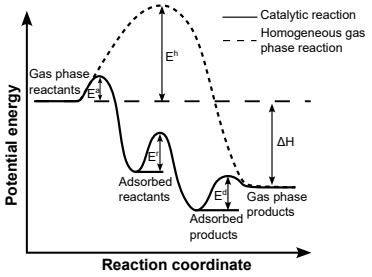

Figure 2.1: Potential energy diagram of a catalytic reaction (solid line) and homogeneous reaction (dashed line), where E^a, E^r, E^d and E^h are the activation energy barrier for adsorption, reaction, desorption and homogeneous reaction, respectively.

- the total number of active sites on the catalyst surface,
- the surface coverage dependent sticking coefficients of reactants describing the probability for the reactants to adsorb,
- the activation energy for adsorption of reactants and desorption of products,
- the activation barrier for the reaction,
- the mobility of surface species.

2.2 CO oxidation on platinum

Platinum is active for total oxidation reactions and robust towards CO_2, H_2O and sulfur deactivation, which makes it a preferred element in various applications [11, 22, 27]. Further, CO oxidation on platinum is one of the most widely studied catalytic reactions. As first proposed by Langmuir and summarized by Engel and Ertl [28, 29], CO oxidation over platinum above room temperature proceeds through a three-step reaction scheme where CO adsorbs associatively, while O_2 adsorbs dissociatively. Then adsorbed CO diffuses to react with O to produce CO_2, which desorbs immediately. However, at low temperatures, the active sites may be mainly occupied by CO, which blocks oxygen adsorption. This is called CO self-poisoning. One reason for this is that the sticking coefficient[1] of CO is around eight times higher than that for O_2, and the corresponding coverage dependency is much weaker for CO than for O_2 [30, 31]. Another reason is that CO adsorption only occupies one site, whereas O_2 adsorption requires two sites next to each other for dissociation. The different kinetic states, i.e., low and high reaction rates, can be described as kinetic bistability, which depends on the reaction conditions, e.g., temperature and reactant ratio between CO and O_2 [32]. When scanning the reactant pressure from O_2 excess to CO excess and from CO excess to O_2 excess, the bistable regions, called hysteresis, can be obtained [33]. The hysteresis originates from kinetic phase transitions between two distinct kinetic regimes at critical mixing ratio or temperature, one is the CO self-poisoned region with low activity and the other is the region with a high activity where the catalyst surface predominately is covered by chemisorbed oxygen. When scanning temperature from low to high and high to low, the ignition and extinction processes can be observed [34, 35]. When passing a critical temperature, ignition occurs with a sudden increase in both reaction rate and catalyst temperature, which self-accelerates the reaction rate. The critical temperature, termed ignition temperature, was defined by Frank-Kamenetskii as a point where the heat generated from the chemical reaction exceeds the heat losses to the surroundings [34]. Further, the ignition temperature shifts the reaction rate from a regime controlled by the surface kinetics at low

1: the ratio between the number of adsorbates adsorbed on a surface and the total number of atoms impinged upon the surface within the same time period.

temperatures to a diffusion-controlled regime where the reaction rate is largely influenced by the transport of reactants to the active sites on the catalyst surface [34, 35]. A reverse transition from a regime controlled by diffusion to a kinetically controlled regime is called extinction. CO oxidation over platinum exhibits a clear ignition-extinction hysteresis. This hysteresis is not only due to the inherent kinetic bistability, but also the coupling of diffusion and heat balances [36].

The kinetic information can be obtained from the analysis in the kinetically controlled region of ignition and extinction processes. The theoretical reaction order can be deduced from a proposed reaction mechanism, and thus a measured reaction order can be used to infer a reaction mechanism, however, not unique. The elementary steps of CO oxidation over platinum can be expressed as:

$$\mathrm{CO(g)} + * \underset{\mathrm{k_1^-}}{\overset{\mathrm{k_1^+}}{\rightleftharpoons}} \mathrm{CO*} \tag{2.3}$$

$$\mathrm{O_2(g)} + 2* \underset{\mathrm{k_2^-}}{\overset{\mathrm{k_2^+}}{\rightleftharpoons}} 2\mathrm{O*} \tag{2.4}$$

$$\mathrm{O*} + \mathrm{CO*} \xrightarrow{k_r} \mathrm{CO_2(g)} + 2* \tag{2.5}$$

where * denote free sites, k_i^+, the adsorption rate constant, and k_i^-, the desorption rate constant for different steps. The CO and O coverage under steady-state conditions can be obtained, when Eq 2.5 is considered as a rate-determining step, $k_\mathrm{r} \ll k_1^+$ and $k_\mathrm{r} \ll k_2^+$:

$$\theta_\mathrm{CO} = K_1 P_\mathrm{CO} \theta_* \tag{2.6}$$

$$\theta_\mathrm{O} = K_2 P_{\mathrm{O_2}} \theta_* \tag{2.7}$$

where $K_i = k_i^+ / k_i^-$ defines the equilibrium constant for species i, and k_r, the reaction rate constant. Assuming CO as the most abundant reaction intermediate (MARI) at low temperatures where θ_*+θ_CO=1, the reaction rate can be expressed as:

$$r = k_r \frac{\sqrt{K_2 P_{\mathrm{O_2}}}}{K_1 P_\mathrm{CO}} \tag{2.8}$$

The reaction orders are −1 for CO and 0.5 for O_2, respectively.

Herein the rate equations are:

$$\frac{d\theta_\mathrm{CO}}{dt} = k_1^+ p_\mathrm{CO} \theta_* - k_1^- \theta_\mathrm{CO} - k_\mathrm{r} \theta_\mathrm{CO} \theta_\mathrm{O} \tag{2.1}$$

$$\frac{d\theta_\mathrm{O}}{dt} = 2k_2^+ p_{\mathrm{O_2}} \theta_*^2 - 2k_2^- \theta_\mathrm{O}^2 - k_\mathrm{r} \theta_\mathrm{CO} \theta_\mathrm{O} \tag{2.2}$$

2.3 CO oxidation on supported Pt

Supported Pt catalysts with high dispersion have been widely used in automotive exhaust after-treatment systems thanks to their superior catalytic performance and robustness. Platinum is not only a

robust element towards gas components but also towards sintering by sufficiently strong interactions with the support materials [11, 22, 27]. Metal oxides are normally used as supports including "inert" support materials and active support materials, such as alumina and ceria, respectively. The "inert" support materials cannot be reduced reversibly, however, active support materials are generally reducible with dynamic redox properties, and they can work as an oxygen buffer participating in the catalytic reaction. Also, reducible supports may interact with platinum through electron transfer and active sites at the platinum-support boundary. Thereby, the support material selection is crucial as it not only influences the dispersion of platinum but the catalytic properties as well as the overall catalytic performance [37–39]. Support material can play an important role in stabilizing platinum particles to achieve a high dispersion, even enabling catalysts with atomically dispersed platinum, which would allow for maximum utilization of platinum. However, CO adsorbed on atomically dispersed platinum has been shown to be spectators, thus resulting in low catalytic activity [40, 41]. Instead, platinum nanoparticles of 1.4 nm have been proven to be the most active ones [42]. Thus, the kinetics on smaller platinum particles, 1-5 nm, clearly depend on the interacting support [42, 43]. The actual system thereby can be complicated by the variation of platinum particle sizes, which exhibits the interaction with the support material distinctively.

Small platinum particles definitely provide more available sites for CO adsorption, but also give more flexibility on the reaction paths. The support material could also contribute to the catalytic activity by providing complementary reaction paths via interfacial sites at the platinum-support boundary. A molecular O_2 adsorption on a single site, rather than two sites, has been proposed, and the corresponding elemental steps are as follows [44]:

$$\mathrm{CO(g)} + * \underset{\mathrm{k_1^-}}{\overset{\mathrm{k_1^+}}{\rightleftharpoons}} \mathrm{CO*} \tag{2.13}$$

$$\mathrm{O_2(g)} + * \underset{\mathrm{k_2^-}}{\overset{\mathrm{k_2^+}}{\rightleftharpoons}} \mathrm{O_2*} \tag{2.14}$$

$$\mathrm{O_2*} + \mathrm{CO*} \xrightarrow{k_{r3}} \mathrm{CO_2(g)} + \mathrm{O*} + * \tag{2.15}$$

$$\mathrm{O*} + \mathrm{CO*} \xrightarrow{k_{r4}} \mathrm{CO_2(g)} + 2* \tag{2.16}$$

Assuming a low atomic oxygen coverage at steady-state ($k_{r3} \ll k_{r4}$)

The corresponding rate equations:

$$\frac{d\theta_{CO}}{dt} = k_1^+ p_{CO}\theta_* - k_1^-\theta_{CO} - k_{r3}\theta_{CO}\theta_{O_2} - k_{r4}\theta_{CO}\theta_O \tag{2.9}$$

$$\frac{d\theta_{O_2}}{dt} = k_2^+ p_{O_2}\theta_* - k_2^-\theta_{O_2} \tag{2.10}$$

$$- k_{r3}\theta_{CO}\theta_{O_2} \tag{2.11}$$

$$\frac{d\theta_O}{dt} = k_{r3}\theta_{CO}\theta_{O_2} - k_{r4}\theta_{CO}\theta_O \tag{2.12}$$

and CO as MARI, the coverage can be derived:

$$\theta_{CO} = \frac{K_1 P_{CO}}{1 + K_1 P_{CO}} \tag{2.17}$$

$$\theta_{O_2} = K_2 P_{O_2} \frac{1}{1 + K_1 P_{CO}} \tag{2.18}$$

Given K_1P_{CO}, the reaction rate is given by:

$$r = k_{r3} \frac{\sqrt{K_2 P_{O_2}}}{K_1 P_{CO}} \tag{2.19}$$

The reaction orders are -1 for CO and 1 for O_2. Moreover, the reaction on a reducible metal oxide support could proceed via the Mars-van Krevelen mechanism where non-competitive adsorption of CO and O_2 on the Pt particles and oxide are considered at low temperatures, respectively [45]. The elementary steps are listed in below [46, 47]:

$$CO(g) + *_1 \underset{k_1^-}{\overset{k_1^+}{\rightleftharpoons}} CO*_1 \tag{2.23}$$

$$O_2(g) + *_2 \underset{k_2^-}{\overset{k_2^+}{\rightleftharpoons}} O_2*_2 \tag{2.24}$$

$$O_2*_2 + CO*_1 \overset{k_{r3}}{\rightarrow} CO_2(g) + O*_2 + *_1 \tag{2.25}$$

$$O*_2 + CO*_1 \overset{k_{r4}}{\rightarrow} CO_2(g) + *_1 + *_2 \tag{2.26}$$

where $*_1$ are the free sites on platinum, $*_2$, free sites on support. There is no competitive adsorption between CO and O_2 at steady-state [2], then we obtain:

$$\theta_{CO} = \frac{K_1 P_{CO}}{1 + K_1 P_{CO}} \tag{2.27}$$

$$\theta_{O_2} = \frac{K_2 P_{O_2}}{1 + K_2 P_{O_2}} \tag{2.28}$$

$$\theta_O = \frac{k_{r3}}{k_{r4}} \frac{K_2 P_{O_2}}{1 + K_2 P_{O_2}} \tag{2.29}$$

With the assumption of Eq. 2.25 as RDS ($k_4 \ll k_3$), and $K_1P_{CO} \gg 1$ and $K_2P_{O_2} \gg 1$, the reaction rate is:

$$r \approx k_{r3} \tag{2.30}$$

Eventually, this leads to the reaction order of 0 for both CO and O_2 at low temperatures.

The time-dependent rate equations:

$$\frac{d\theta_{CO}}{dt} = k_1^+ p_{CO} \theta_{*1} - k_1^- \theta_{CO} - k_{r3} \theta_{CO} \theta_{O_2} - k_{r4} \theta_{CO} \theta_O \tag{2.20}$$

$$\frac{d\theta_{O_2}}{dt} = k_2^+ p_{O_2} \theta_{*2} - k_2^- \theta_{O_2} - k_{r3} \theta_{CO} \theta_{O_2} \tag{2.21}$$

$$\frac{d\theta_O}{dt} = k_{r3} \theta_{CO} \theta_{O_2} - k_{r4} \theta_{CO} \theta_O \tag{2.22}$$

2: $\theta_{CO}+\theta_{*1}=1$, $\theta_{O_2}+\theta_{*2}=1$

2.4 Development of CO oxidation catalysts

The main challenge of designing new catalysts is to identify the active components and their role in catalytic reactions, such as bimetallic, unsupported, and supported catalysts with different functionalities [15]. Except for metal-support interaction, acidity, basicity, and electronic effects could also play important roles. Developing new catalysts is a rather complicated task. It may require fundamental knowledge about the reaction, e.g., understanding and circumventing the CO self-poisoning effect, and empirical experience [15]. It may also require elemental screening to find the optimal catalysts and further improvement on the long-term performance and suppression of deactivation from the presence of other gas components. Another difficulty lies in the dynamic catalyst structure under the reaction conditions, thus, further progress together with the characterisation techniques might be needed. To be worth mentioning is to design new catalysts by theoretical modeling, which has been shown to work for some bi- or tri-metallic catalysts [35, 48, 49].

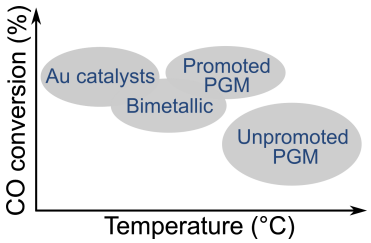

Figure 2.2: Scheme of catalytic performance of different catalysts for CO oxidation.

Screening the catalysts for CO oxidation, they can be practically divided into several groups, gold (Au) catalysts, unpromoted and promoted platinum group metals (PGM), e.g., platinum, palladium and rhodium, bimetallic catalysts, and nanosized metal oxides are displayed in Figure 2.2. Au catalysts are generally very active at low temperatures but sinter easily at high temperatures [50, 51] and are inactive. The PGM catalysts exhibit high activity at temperatures slightly higher than Au catalysts, with high resistance towards sintering and deactivation [52, 53]. PGM can be dispersed on non-reducible and reducible supports to achieve smaller particles with more catalytic active sites, and improved low-temperature activity, possibly due to interaction with the support. An improved sulfur tolerance, higher thermal stability, and higher hydrothermal durability could also be expected [54, 55]. The main limitations for PGM are the cost and the availability, the amount can be thus lowered by using supports to achieve high dispersion with low loading or forming bimetallic catalysts, or even nanosized metal oxides are shown to be promising for the future development [56–59].

2.5 Specific objective

The objective of this thesis is to elucidate how CO oxidation proceeds on industrial-relevant Pt/ceria catalysts with Pt/alumina as a reference and an attempt to design Pt/FeO_x catalysts for this reaction. A summary of the appended paper is shown in Figure

2.3. The relation between reaction order and reaction mechanisms is investigated by experimental reaction order measurements on small and large Pt particles supported on alumina, denoted as Pt_{small}/alumina and Pt_{large}/alumina, as well as microkinetic modeling from theoretical calculation in Paper I. A further Density Functional Theory (DFT) calculations are performed for the reaction over Pt/ceria to explore the reaction mechanism supplemented with experimental kinetic studies on Pt/ceria in Paper II. Paper III scrutinizes how the catalytic activity is associated with catalyst structure and species adsorbed on the surface by *operando* spectroscopic techniques and provides a thorough *ex-situ* examination of physicochemical properties. Furthermore, the influence of NO and H_2O on the reaction over Pt/ceria and Pt/alumina is probed spectroscopically and kinetically, and the properties of spent catalysts after the reactions are carefully inspected in Paper IV. Eventually, a catalytic design of utilizing different types of iron oxides as support materials is attempted for CO oxidation, and the catalysts are evaluated with their redox properties and structure dynamics by high-energy X-ray diffraction (HEXRD).

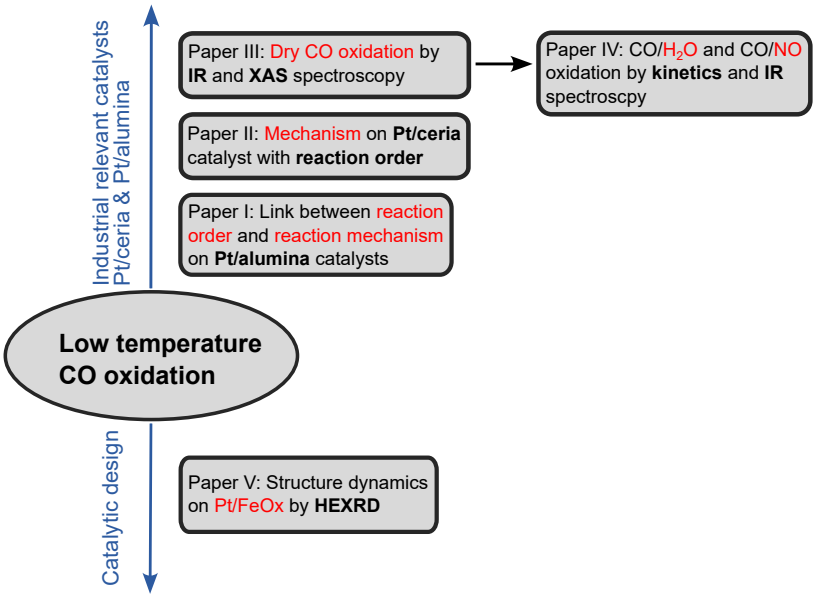

Figure 2.3: Structure of the appended papers for the objective of the thesis.

Catalytic synthesis and characterisation methods

3

Characterisation is of importance in the field of catalysis in terms of building knowledge about the catalysts so as to better understand the catalytic function and eventually to improve the design of catalysts. Methods based on adsorption and desorption, microscopy, spectroscopy, and diffraction provide tools for the characterisation of the catalysts.

3.1 Catalyst synthesis . . . 13
3.2 Flow reactor measurements 14
3.2.1 Reactor configuration . 14
3.2.2 Mass spectrometry . . 16
3.2.3 Data evaluation 17
3.3 Gas Sorption 19
3.3.1 Physisorption 19
3.3.2 Chemisorption 20
3.4 Electron microscopy . 22
3.4.1 Scanning electron microscopy 22
3.4.2 Transmission electron microscopy 22
3.5 Spectroscopy 24
3.5.1 Infrared spectroscopy . 24
3.5.2 X-ray absorption spectroscopy 28
3.6 Scattering 31
3.6.1 X-ray diffraction 32
3.6.2 High-energy X-ray diffraction 32

3.1 Catalyst synthesis

Two major approaches, top-down and bottom-up, are used for synthesizing the nanomaterials, which can be used as catalysts [60, 61]. In top-down approaches, one way is to machine the bulk materials to obtain fine powders made of nanoparticles [60]. Massive bottom-up approaches have been developed to produce the nanoparticles, and one of them is self-assembly under certain chemical and temperature conditions [62]. Furthermore, the nanoparticles can be loaded onto support materials. As for support materials, a high surface area and proper thermal stability are needed to carry and stabilise the active particles during reaction conditions. The well-defined nanoparticles can be first synthesized via various methods, such as sol-gel and seeded-growth, or can be formed directly on the support material by the incipient wetness impregnation (IWI) of the precursor material together with drying. The resultant catalyst is shown in Figure 3.1. IWI is commonly used for the preparation of heterogeneous catalysts thanks to its simplicity, low costs, and waste produced. The volume of pores equals the amount of the precursor solution, which is dragged into the pores due to the capillary action. The following drying and calcination are applied to drive off the volatile solution and deposit the active material on the catalyst surface. However, the solubility of the precursor solution together with the pore volume limits the maximum loading of metal on the support.

In this work, a bottom-up approach was applied with co-precipitation for the support material, different types of iron oxide, and IWI for the deposition of active metal particles, platinum. Iron(II) chloride tetrahydrate ($FeCl_2{\cdot}4H_2O$, 99.99%, Sigma Aldrich) of 0.36 M was mixed with iron(III) chloride hexahydrate ($FeCl_3{\cdot}6H_2O$, ≥99% Sigma Aldrich) of 0.72 M under N_2 atomosphere. 4 mL of hydrochloric acid (HCl, 37% Sigma Aldrich) was added, and after 15 min, 30 mL of ammonium hydroxide solution (NH_4OH,

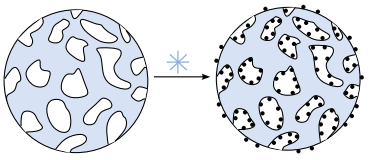

Figure 3.1: A schematic representation of the support material before and after loading the precursor material by incipient wetness impregnation and freeze drying.

25% Sigma Aldrich) was poured to form the precipitates and the resulting pH was 10-11. Afterward, 2L of Mill-Q water was used for washing and the resulting precipitates were obtained after filtration. This was followed by a vacuum drying at room temperature for 48 hrs and further by calcination at 250 °C with a heating rate of 5 °C/min and constant temperature at 250 °C for 12 hrs. After grinding the support material, the precursor solution of tetraammineplatinum(II) hydroxide ($(NH_3)_4Pt(OH)_2$, 8-11 wt% Pt VWR) was deposited by using IWI and freeze drying, and subsequently, calcination at 250 and 500 °C for another 12 hrs after the desired temperatures were reached with a heating rate of 5 °C/min. Around 1 wt% of Pt/maghemite and Pt/hematite were eventually obtained. The Pt/ceria and Pt/alumina samples with small and large particle sizes denoted Pt_{small}/alumina and Pt_{large}/alumina, were synthesized by IWI using platinum salts followed by drying and calcination at 500 °C for Pt/ceria and Pt_{small}/alumina, and at 800 °C for Pt_{large}/alumina.

3.2 Flow reactor measurements

Kinetics measured in a flow reactor provides a macroscopic view on the catalytic reaction. Reaction mechanisms could be further inferred based on the rate expression from proposed reaction pathways, which provides a microscopic view of the reacting molecules.

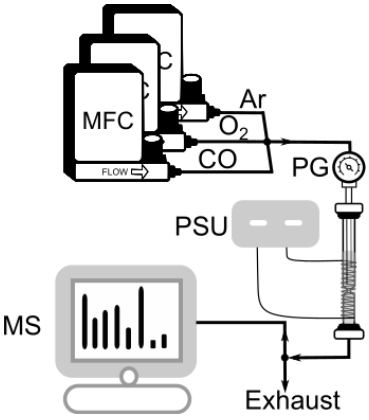

Figure 3.2: A schematic setup of flow reactor for CO oxidation, where MFC represents for mass flow controller, PG, for pressure gauge, PSU, for power supply unit, MS, for the mass spectrometer. The setup design is credited to Felix Hemmingsson.

3.2.1 Reactor configuration

The chemical reactor is at the heart of the chemical production process and the selection of the reactor can be associated strongly with the type of chemical reaction and catalyst. The reactors can be divided into two major types regarding the number of phases: homogeneous (single-phase) and heterogeneous (multi-phase). An example of heterogeneous reactors is fluid-solid which includes fixed-bed and fluidized-bed reactors [15]. They can be, operated in batch, semi-batch, and continuous modes. Batch operation is non-stationary, where the concentration of the reactants and products and the reaction rate vary with time. On the contrary, continuous operation is stationary, where the reactants are continuously fed into the reactor and the products are observed at a constant rate resulting in a time-independent concentration of all reactants and products and a constant reaction rate.

In this work, a fixed-bed flow reactor is first utilized for dry CO oxidation due to the suppression of the active sites blockage from binding material during monolith coating[1][63]. However,

1: A monolith is dipped and withdrawn in the slurry until a desired amount of washcoat is reached. The slurry is made of catalyst powder and a proper binder material mixed with an equal amount of water and ethanol

one needs to be aware and take precautions in regard to aspects such as pressure drop and hot zones, thus the pressure drop can be mitigated by increasing particle size and hot zones can be counteracted by decreasing the sample amount and/or mixing with inert materials as diluent. The speed of heat dissipation depends on the heat conductivity of the diluent material. The used experimental setup is schematically presented in Figure 3.2. The gas flow is controlled by several mass flow controllers (MFCs) and fed into the reactor top-down. A vertically placed 33 cm long quartz tube is used as the reactor with an inner diameter of 4 mm and an outer diameter of 6 mm. The reaction temperature is achieved through resistive heating by a metal coil twisted around the reactor and insulated by a quartz wool layer, while the rest of the tubing is surrounded by heating bands and wrapped by insulation. The catalyst with a particle size of 40–80 µm is diluted with crushed cordierite with a particle size of 300–355 µm to mitigate the pressure drop. The mixture with a dilution ratio of 1:30 is loaded into the reactor to even out the heat from the exothermic reaction. One thermocouple is used to regulate the inlet gas temperature placed 1-2 mm above the bed, and another inserted one placed 1 cm below the sample bed is applied to monitor the temperature of the sample bed, which can be influenced by heat from the reaction. Eventually, the effluent gas is analyzed by a mass spectrometer, which is described below. Water can be generated via humidifiers and water

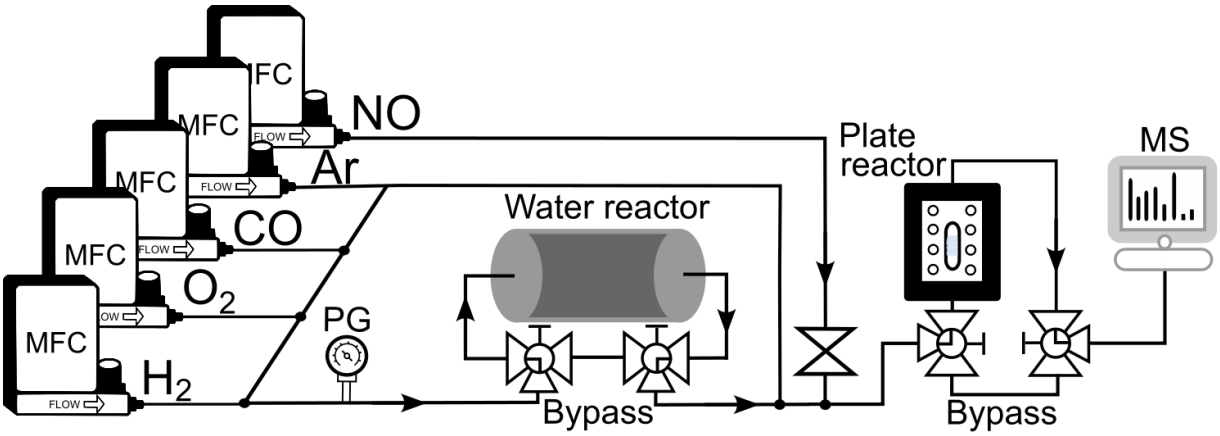

Figure 3.3: A schematic setup of flow reactor for CO/H_2O and CO/NO oxidation, where MFC is for mass flow controller, PG, for pressure gauge, MS, for the mass spectrometer. The setup design is credited to Felix Hemmingsson.

bubblers[2]. Another possibility is to use a controlled evaporation mixer (CEM), where an additional liquid pressurization chamber can be used to pressurize the liquid water, and liquid mass flow controllers (l-MFCs) can be applied to control and evaporate liquid water into the carrier gas [67]. However, the stability and precision may be limited by low water vapor concentrations with low gas flows. Impurities from the water reservoir and insufficient water purity coming from the dissolution of atmospheric gas components may be problematic. This can be solved by producing ultra-pure

2: The humidified gas flow can be delivered by passing over the surface of liquid water at a certain temperature and pressure or passing through it [64–66].

water using a water reactor by the catalytic oxidation of hydrogen, which can be achieved by dosing H_2 and O_2 over a platinum-coated monolith, and thus producing a well-controlled concentration from a range of 100 ppm to 3 vol.% [68]. The schematic setup is depicted in Figure 3.3. The gas flow controlled by multiple MFCs is from the bottom upwards. The H_2 and O_2 MFCs are directly connected to the water reactor before joining the mainstream with the possibility of bypassing to perform dry CO oxidation. The pipes are well insulated and heated to 180 °C before the reactor and to 120 °C after the reactor. The reactor is made of stainless steel with a height of 3 mm, a width of 5 mm, and a length of 17 mm, and a type K thermocouple is inserted inside the sample bed [69]. Resistive heating is used for the reactor by the metal block behind, which is controlled by another embedded type K thermocouple, and the whole reactor, together with the metal block, is insulated by quartz wool. A catalyst-cordierite mixture with a particle size of 100-300 µm and a dilution of 1:10 is loaded into the reactor. The effluent gases are analysed by the MS (Pfeiffer Vacuum GSD-350).

In this thesis, the catalytic activity measurements were carried out with a total flow of 150 ml/min under 0.2 vol.% CO, 1 vol.% O_2 and 2 vol.% H_2O, and Ar was used as a carrier gas throughout all the measurements. The temperature cycle, which consists of increasing temperature to 350 °C with a rate of 5 °C/min and maintaining for 1 hr for the extinction, then decreasing to 35 °C, was repeated three times.

3.2.2 Mass spectrometry

Mass spectrometry (MS) is generally used to identify and quantify the effluent gas composition. Different gas components are first ionized and subsequently separated according to their mass-to-charge ratio (*m/z*). The relative abundances of the charged gaseous ions are recorded. A common mass spectrometer includes an ion source, an analyzer, and a detection system. An ion source is produced from an electron beam ionisation. Before that, a high vacuum environment is needed. Ions are subsequently sorted by applying a magnetic field as the ions with the same *m/z* deflect in the same direction. Eventually, the separated ions are detected and an abundance spectrum is produced. However, some molecules have the same *m/z*, e.g., carbon monoxide and nitrogen, of 28, and the fragmentation can thus be used to distinguish them as nitrogen also gives a signal at 14 (*m/z*) with a considerably lower signal as compared to 28 (*m/z*).

3.2.3 Data evaluation

The nature of catalytic reactions combines the reaction and transport processes which are presented in Figure 3.4. Assuming a spherical and porous catalyst particle is surrounded by the gaseous reaction mixture, the steps of transforming the reactant, R, to the product, P, are below:

1. R is transported from the bulk through the boundary layer[3] to the catalyst surface,
2. R diffuses inside the pores of the catalyst particles to find the catalytic active sites,
3. R adsorbs at the active sites,
4. P is produced by chemical reaction,
5. P desorbs from active sites,
6. P diffuses through pores to the surface,
7. P is transported through the boundary layer to the bulk.

3: an (imaginary) film between the surface and the bulk in which the concentration differs from that of the bulk.

When the rates of the transport processes, 1,2 6, and 7, are faster than the intrinsic chemical reaction steps 3-5, the overall rate or the observed reaction rate is said to be kinetically controlled. Opposite to this, the observed rate can be controlled by internal diffusion. This occurs if the intrinsic chemical reaction rate is faster than the rate of intraparticle diffusion, which could result from a high inner specific surface area, and thus a concentration gradient is introduced inside the particles. If the external mass transfer controls the observed rate, the concentration at the outer surface is lower than the bulk concentration and the concentration profile will be more obvious inside a pellet. Weisz-Prater and Mears' criterion can be applied to examine internal and external diffusion, respectively (3.1 and 3.4), as shown below [70]:

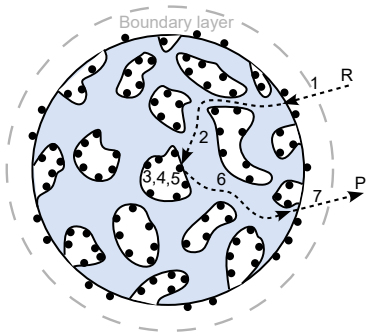

Figure 3.4: A schematic representation of transport processes on porous catalysts, where R and P represent reactants and products, respectively.

$$C_{wp} = \frac{r_{obs}\rho_c R_p^2}{D_{eff} C_s} \tag{3.1}$$

$C_{wp} = \eta\phi_1 = \frac{\text{Actual reaction rate}}{\text{A diffusion rate}}$
η is defined as effectiveness factor
$\eta = \frac{\text{Observed reaction rate}}{\text{Reaction rate evaluated at } C_s}$
ϕ_1 represents the Thiele modulus for a first order reaction
$\phi_1 = \frac{\text{Reaction order evaluated at } C_s}{\text{A diffusion rate}}$

where r_{obs} is the observed reaction rate (mol/kg_{cat}· s), and it can be calculated from:

$$r_{obs} = q\frac{p_{CO}}{RT}\frac{X_{CO}}{m_{cat}} \tag{3.2}$$

where q is the volumetric flow rate (m^3/s), p_{CO}, the CO partial pressure, R, the molar gas constant (8.314 J/(mol· K)), T, the temperature (K), m_{cat}, the mass of catalyst (kg), and X_{CO}, the conversion of CO. X_{CO} can be expressed as:

$$X_{CO} = \frac{(n_{CO,\,in} - n_{CO,\,out})}{n_{CO,\,in}} \tag{3.3}$$

R_p is catalyst particle radius (m), ρ_c, the bulk density of catalyst (kg/m^3)[4], ρ_b=(1-Φ)ρ_c (Φ is the void fraction)[5], D_{eff}, the effective

4: $\rho_c = \frac{\text{Mass of catalyst}}{\text{Volume of catalyst}}$

5:

$$\Phi = \frac{\text{Volume of catalyst}}{\text{Reactor volume}}$$

$$\rho_b = \frac{\text{Mass of catalyst}}{\text{Reactor Volume}}$$

diffusivity (m^2/s), and C_s, the gas concentration at the external surface of the catalyst (mol/m^3). Internal diffusion can be neglected when $C_{wp} \ll 1$. On the contrary, the internal diffusion influences the reaction rate when $C_{wp} \gg 1$. Furthermore, the influence of external diffusion can be determined by Mears' criterion:

$$C_{mr} = \frac{r_{obs}\rho_b R_p n}{k_c C_b} \tag{3.4}$$

where n is the reaction order, C_b, the bulk reactant concentration (mol/m^3), and k_c, the mass transfer coefficient (m/s). The reaction rate is not affected by external mass transport when $C_{mr} < 0.15$. Also, the influence of external mass transfer on observed reaction rate can be determined by comparing the estimated concentration gradient ($\triangle C_{CO}$) over the gas film with the bulk gas concentration (C^b_{CO}). $\triangle C_{CO}$ can be derived from the steady-state reaction rate for a fixed-bed reactor:

$$r = S_m k_c \triangle C_{CO} \tag{3.5}$$

where $S_m = \frac{3}{R_p \rho_c}$, and $k_c = \frac{Sh D_{eff}}{2R_p}$. Thus:

$$\triangle C_{CO} = \frac{2 r R_p^2 \rho_c}{3 Sh D_{AB}} \tag{3.6}$$

where r can be substituted by r_{obs} and using a reasonably low value for the Sherwood number[6] (Sh=1.5) will give the most significant concentration gradient, and D_{AB} is the binary gas diffusivity (m^2/s). Except for the influences from diffusion, the heat generated from the reaction is another concern. The amount of sample can be reduced to minimize the heat effect. The internal heat transfer can be examined by Anderson criterion [71]:

6: the ratio between the rate of convective mass transfer and the rate of diffusive mass transport

$$\frac{\mid \triangle H_r \mid r_{obs}\rho_d R_p^2}{\lambda_e T_s} < 0.75 \frac{R T_s}{E} \tag{3.7}$$

where λ_e is the effective thermal conductivity ($J/(s \cdot m \cdot K)$), T_s, the catalyst surface temperature (K), and E_a, the true activation energy (J/mol).

The kinetic measurements, of course, provide the information about the chemical reaction, but the focus can be shifted from the reaction to the catalyst using turnover frequency (TOF)[7]. It can be evaluated in terms of metal dispersion:

7: reactant molecules converted per catalytic site in unit time

$$TOF(s^{-1}) = r_{obs} \cdot \frac{M_{Pt}}{X_{Pt} D_{Pt}} \tag{3.8}$$

where M_{Pt} is the molecular weight of Pt (g/mol), X_{Pt}, the Pt loading, and D_{Pt}, the Pt dispersion, which can be measured by *chemisorption* described below.

In this work, in order to extract kinetic information from flow reactor measurements, the analysis needs to be performed in a kinetically controlled regime which is a generally low conversion region (below 20%). The apparent activation energy (E_a) and reaction orders are derived from the measurements between the reaction rates and temperatures or partial pressures.

3.3 Gas Sorption

Porous catalysts are widely used in heterogeneous catalysis and the structure of the porous catalysts can be probed by gas sorption techniques. Two types of sorption, *physisorption* and *chemisorption* are classified depending on how molecules adhere to the solid surfaces. Physisorption is associated with a weak non-specific interaction between adsorbate and adsorbent, e.g., van der Waals forces. Chemisorption involves a strong specific interaction of forming chemical bonds between adsorbate and adsorbent.

3.3.1 Physisorption

The surface area determines the accessible area for gaseous reactants and the space to disperse metal particles, which can be crucial for catalytic performance. The specific surface area (SSA) can be measured by *physisorption* using N_2 at 77K from the adsorption and desorption isotherms[8]. Other options for the probing molecules could be Ar, CO_2, Kr, and O_2, depending on the pore widths of the adsorbent and the cross-sectional area of the probing molecules. The widely used cross-sectional area[9] of N_2 is 16.2 $Å^2$, which could differ according to the adsorbent [72]. The SSA can be obtained from the isotherms when Braunauer, Emmett, and Teller (BET) theory is applied, which has generalized the Langmuir isotherm assumptions[10]. Multilayer adsorption has also been taken into consideration. The additional assumptions are made in the below [15]:

- The adsorption energy is constant within the first layer,
- The adsorption energy for the rest of the layers equals the molar heat of condensation,
- Considering infinite number of layers, the pressure, P, is equivalent to the saturation pressure, P_0.

Figure 3.5 shows an example of N_2 adsorption-desorption isotherms for Pt/alumina. At position 1, the adsorption of N_2 molecules starts at a rather low pressure. At position 2, a monolayer of N_2 molecules is formed and continued with multilayer adsorption. From position 3, multilayered adsorption transforms from a

8: the surface coverage changes of N_2 gas molecules with equilibrium pressure

9: the occupied area of a single N_2 molecule on the adsorbent

10: · Only one monolayer developed between gas and solid surface
· An uniform adsorbent surface with equal adsorption sites
· No adsorbate-adsorbate interaction

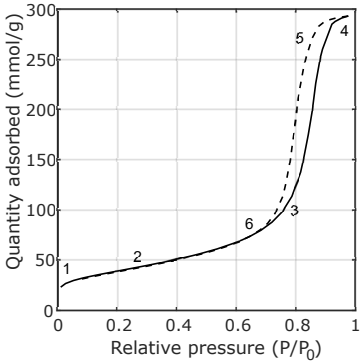

Figure 3.5: N_2 adsorption (solid line) and desorption (dash line) isotherms of Pt/alumina.

vapor phase to a liquid phase, called capillary condensation which occurs at a critical thickness. However, the reason this takes place before the saturation pressure (P_0) is because of the increased effect of van der Waals forces inside pores. The desorption process is represented with a dashed line. The hysteresis loop is classified as the H1 type, which exhibits a well-defined cylindrical pore [73].

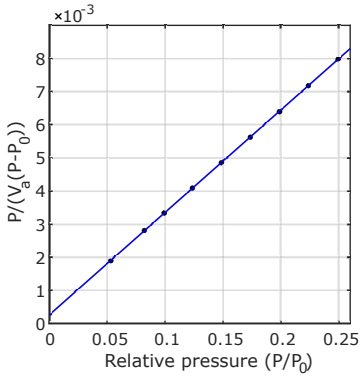

Figure 3.6: BET plot of Pt/alumina.

The SSA (m^2/g) can be calculated in the following:

$$\mathrm{SSA} = \frac{V_\mathrm{m}\sigma N_\mathrm{A}}{mV_{\mathrm{N_2}}} \tag{3.9}$$

where σ is the cross sectional area, N_A, the Avogadro constant, m the mass of adsorbent, and $V_{\mathrm{N_2}}$ the N_2 gas molar volume at standard temperature and pressure (STP). V_m is the adsorbed gas molar volume demanded to form a monolayer, which can be obtained from the BET equation as below:

$$\frac{P}{V_\mathrm{a}(P_0 - P)} = \frac{1}{cV_\mathrm{m}} + \frac{c-1}{cV_\mathrm{m}}\frac{P}{P_0} \tag{3.10}$$

where V_a is the total adsorbed gas volume, c a constant only related to the adsorption heat of the first layer, P the pressure, and P_0 the saturation pressure. An example of applying the BET equation with a defined pressure range is shown in Figure 3.6, where V_m and c can be retrieved from the slope or intercept of the linear regression.

In this thesis, the samples were dried overnight at 250 °C under a flow of N_2 before measurements, a Tristar 3000 (Micromeritics) instrument and the Brunauer-Emmett-Teller (BET) equation were employed to obtain the SSA.

3.3.2 Chemisorption

Efficient utilization of active precious metals with a high dispersion is economically crucial. *chemisorption* can be used to determine the metal dispersion, specific metal area, and particle size. The monolayer assumption is analogous to the *physisorption*. However, *chemisorption* involves electrons shared between the adsorbate and adsorbent, which is an irreversible process. After initial adsorption, a second isotherm is performed and a vacuum is applied in between to desorb physisorbed molecules [74]. One obtains the amount of chemisorbed molecules from their difference. An example of *chemisorption* isotherms using CO molecules for Pt/alumina is shown in Figure 3.7. The CO *chemisorption* is represented by the orange squares, and the last 8 points in the plateau region are used for linear regression. The quantity of chemisorbed CO monolayer

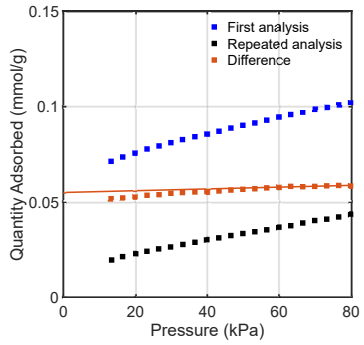

Figure 3.7: CO adsorption isotherms at 35 °C for Pt/alumina. Blue squares describe the first analysis containing *physisorption* and *chemisorption*, and the black ones depict only *physisorption* in the repeated analysis. The orange ones give the chemisorption after the subtraction of the repeated analysis from the first one.

per gram catalyst (Q_{CO}, mol/g) at STP, is determined from the intercept of linear regression in Figure 3.7. The monolayer volume (V_m) in cm^3/g can be derived from:

$$V_m = Q_{CO} V_{CO} \tag{3.11}$$

where V_{CO} is CO molar volume at STP in cm^3/mol. The metal dispersion (D_{metal}) describes the fraction of surface metal sites that are accessible to CO over the total metal sites. This can be expressed as:

$$D_{metal} = \frac{Q_{CO} M_{metal} F_s}{W_{metal}} 100\% \tag{3.12}$$

where M_{metal} is the metal molar mass in g/mol, W_{metal}, the weight percentage of active metal over sample, and F_s, stoichiometric factor. F_s represents the number of active metal atoms probed by one adsorbed CO molecule, which can be estimated from infrared spectroscopy upon CO adsorption. The specific metal area, A_{metal}, accessed by probing molecules, in $cm^2/(g\ of\ sample)$ can be formulated in below:

$$A_{metal} = Q_{CO} F_s \sigma_s N_A \tag{3.13}$$

where σ_s is cross-sectional area of Pt, which is 8 $Å^2$. Additionally, the particle diameter (d_{metal}), can be evaluated with a certain geometry, here, hemispheres:

$$d_{metal} = \frac{6 \cdot W_{metal}}{A_{metal} \rho_{metal}} \tag{3.14}$$

where ρ_{metal} is the density of the pure metal.

In this thesis, the Pt/ceria catalyst was pretreated with 100 vol.% O_2 at 500 °C for 1 h, and exposed to 100 vol.% H_2 for 1 h after cooling to 250 °C in O_2. Then, the sample was cooled to 35 °C in the presence of H_2 and kept in 100 vol.% CO_2 for another hour. Subsequently, the sample was flushed with 100 vol.% O_2 for 30 min and then flushed with 100 vol.% H_2 for 30 min. 10-20 min evacuation was applied in between introducing different gases. Afterward, CO chemisorption was performed by dosing 100 vol.% CO from 13 to 93 kPa. Worth to mention, the utilization of a CO_2 sequence was used before CO chemisorption measurements since CO can adsorb on interfacial sites after reduction pretreatment, which leads to a more than 100% dispersion, and these sites can be re-oxidized by CO_2. The subsequent O_2 and H_2 sequences were applied to remove any weakly adsorbed CO.

3.4 Electron microscopy

Electron microscopy has a higher resolving power than light-based microscopy and is one of the most versatile techniques to investigate surface topography, morphology, and crystallographic information. The elemental information can be revealed by the combination of energy-dispersive X-ray spectroscopy (EDX).

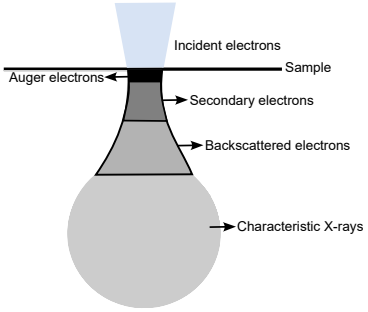

Figure 3.8: The incident electrons interact with the sample, where different types of electrons are produced from different sample volumes.

3.4.1 Scanning electron microscopy

Scanning electron microscopy (SEM) is capable of examining the bulk sample with a high resolution and a large field depth, which makes it possible to obtain topographic and crystallographic information with a resolution between a micrometer (μm) and a nanometer (nm) [75]. Compared to transmission electron microscopy (TEM), less sample preparation is demanded and a thicker sample can be analyzed. When the electrons impinge on the sample surface, the inelastic scattering termed secondary electrons (SE) for the primary electrons with an energy loss, the elastic scattering called back scattered electrons (BSE) when there is no energy loss for the primary electrons, and the characteristic X-rays formed are used in SEM as shown in Figure 3.8. The SE are detected at a lower energy (< 50 eV) with a shallower escape depth near the surface. The images from SE can thus provide topographic information because of a large field depth. Whereas the BSE are the ones with longer escape depth, and the intensity is heavily dependent on the atomic number. The images obtained from BSE can therefore give information about the atomic distribution. Characteristic X-rays are generated when electrons from the inner shell are knocked out by incident electrons to create vacancies that are refilled by the electrons from a higher inner shell. Meanwhile, *Auger electrons*[11] can be activated by the kinetic energy transfer. The generated characteristic X-rays can be used in EDX for analyzing the elemental composition of the first a few micrometers of the surface [75]. As depicted in Figure 3.8, X-rays exhibit a larger probe volume compared to BSE and SE, which makes it possible to measure the properties below the sample surface.

11: the inner-shell vacancy is refilled accompanied by the emission of an electron from the same atom

3.4.2 Transmission electron microscopy

Transmission electron microscopy (TEM) is one of the most intuitive tools to directly observe the shape and size of nanoparticles and crystallographic information. A typical transmission electron microscope contains three main parts: the illumination system, the lens, and the imaging system [76]. A field emission gun and LaB_6 filament can be applied for the illumination system. A field

emission gun exhibits a higher brightness[12] and a better vacuum in comparison with a LaB_6 filament. Our focus of using TEM is TEM imaging and scanning transmission electron microscopy (STEM) imaging with bright-field (BF) and dark-field (DF) images, but it could also be used for selected-area diffraction (SAD) and electron energy loss spectroscopy (EELS).

12: the number of electrons (or charge) per unit area per unit time

Figure 3.9 displays the difference between BF and DF images due to the selection of transmitted or scattered electrons after interacting within the specimen. This can be achieved by using apertures in TEM mode and different detectors are applied for the STEM mode. A parallel electron beam incidents on the specimen for TEM imaging, whereas a convergent electron beam is applied for STEM imaging. Various detectors are positioned at different locations: BF detector positioned at an angle less than 10 mrad, annular dark-field (ADF) detector located at a larger angle between 10 to 50 mrad, and high-angle annular dark-field (HAADF) detector fixed at the angles larger than 50 mrad in Figure 3.10. An example of TEM and STEM micrographs in BF and HAADF mode, respectively, are displayed in Figure 3.11. In TEM BF mode, the image contrast is mainly due to the mass-thickness contrast since a thicker sample or heavy element region will scatter more electrons thus less electrons are transmitted, which gives darker areas of an image [76].

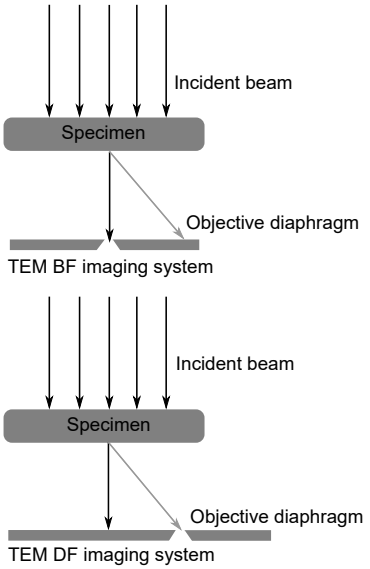

Figure 3.9: Simplified TEM scheme.

Analogously, the mass-thickness contrast contributes STEM-HAADF images to a large extent, which is strongly affected by atomic number. A higher atomic number and a thicker sample will allow more elastic scattering, and obtain a brighter area instead in STEM-HAADF images. As compared to TEM mode, STEM mode gives an overall better contrast and less noisy images due to the absence of using the lens for imaging.

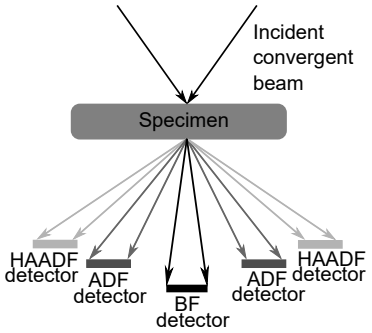

Figure 3.10: Simplified STEM scheme.

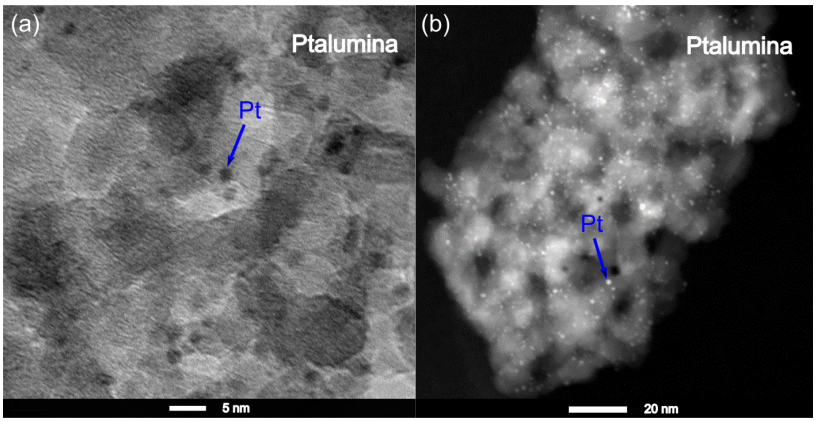

Figure 3.11: TEM (a) and STEM (b) image of Pt/alumina.

In this thesis, a Tecnai T20 microscope (FEI), as well as a Titan 80-300 microscope (FEI), were applied for high-resolution transmission electron microscopy (HRTEM) and STEM, respectively. The Tecnai T20 microscope was equipped with a LaB_6 filament at 200 kV and a high-angle annular dark-field STEM detector and a field emission

gun at 300 kV was employed for the Titan 80-300 microscope. Before that, the specimen was prepared by dispersing spent catalysts into ethanol and mixing them with ultrasonication. Afterward, a holey carbon film on a copper grid was used for loading a droplet of the obtained suspension.

3.5 Spectroscopy

3.5.1 Infrared spectroscopy

The infrared spectrum ranges from 0.8 µm to 1000 µm which constitutes near-infrared (0.8–2.5 µm), mid-infrared (2.5–25 µm) and far-infrared (25–100 µm). Mid-infrared is used to excite electrons for the molecular transitions between vibrational and associated rotational-vibrational energy levels. Diatomic molecular vibration can be classically depicted by Hook's law, and the oscillation frequency, w_e, can be expressed in cm^{-1}:

$$\omega_e = \frac{1}{2\pi c}\sqrt{\frac{k}{\mu}} \tag{3.15}$$

where k is the spring constant, c, the velocity of light, and μ, the reduced mass. The vibrational energy can be obtained considering a simple harmonic oscillator by solving the Schrödingar equation:

$$E_v = (v + \frac{1}{2})\omega_e \quad (v = 0, 1, 2, ...) \tag{3.16}$$

where v is termed as the vibrational quantum number and the emission frequency is equivalent to ω_e with the selection rule of $\Delta v = \pm 1$. Furthermore, a more complicated expression that is close to reality would be:

$$E_v = (v + \tfrac{1}{2})\omega_e - \underbrace{(v + \frac{1}{2})^2\omega_e\chi_e}_{\text{anharmonicity}} + \underbrace{B_e J(J+1)}_{\text{rigid rotator}} - \underbrace{D_e J^2(J+1)^2}_{\text{centrifugal distortion}} - \underbrace{\alpha_e(v + \frac{1}{2})J(J+1)}_{\text{rovibration interaction}} \tag{3.17}$$

where χ_e is an anharmonicity constant, and selection rules turn out to be $\Delta v = \pm 1, \pm 2$, etc. B_e, the rotation constant from a rigid rotational vibration and D_e, the additional centrifugal distortion constant. Vibrations and rotations are assumed to be independent with Born-Oppenheimer approximation, where α_e is the rovibrational coupling constant with selection rule of $\Delta v = \pm 1, \pm 2$, etc., and $\Delta J = \pm 1$.

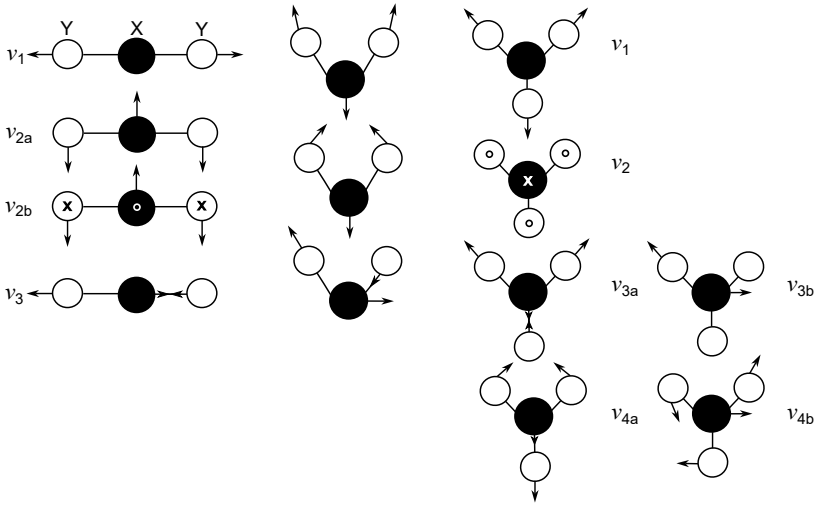

Figure 3.12: Normal modes of vibration of linear and bent YXY, and planar XY_3 molecules. O and X represent the molecules vibrating perpendicular to the plane upward and downward.

Vibration mode

The wavenumber of infrared absorption peaks depends on the vibration modes of the probed molecules, and the gaseous phases are generally detected. The number of fundamental vibrations can be figured out for polyatomic molecules. When the molecules are non-linear, the number of vibrations is 3N-6 with N-1 for stretching mode and 2N-5 for bending mode. When the molecules are linear, the number of vibrations is 3N-5 with N-1 for stretching mode and 2N-4 for bending mode [79]. The normal vibration modes of linear ($D_{\infty h}$) and bent YXY molecule (C_{2v}), and planar XY_3 molecule (D_{3h}) are shown in Figure 3.12. However, not all the vibrations can be probed by IR spectroscopy since this demands the vibrations to be IR active. For instance, homonuclear molecules, e.g., N_2 and O_2, are not observable for vibrational spectroscopy since they have neither permanent dipole moment nor induced dipole moment as the molecules vibrate. As for the linear YXY molecules in Figure 3.12, ν_1 depicts the symmetric stretch of not being IR-active. On the contrary, ν_2 and ν_3 are IR-active, which can be assigned to the bending and asymmetric stretch mode, where ν_{2a} and ν_{2b} are the doubly degeneracy[13] of the bending mode. For the bent YXY molecules, the same vibration modes are classified for ν_1, ν_2, and ν_3 in comparison with the linear one, and all the vibrations are IR active. Coming to the planar XY_3 molecules, the same structure as CO_3^{2-} or NO_3^{2-}, ν_1 is the nondegenerate symmetric stretch, ν_2, the nondegenerate asymmetric bend (perpendicular to the plane), ν_3, the doubly degenerate asymmetric stretch, and ν_4, the doubly degenerate symmetric bend. Among those, ν_2, ν_3 and ν_4 are IR active. The splitting observed in the wavenumber region of 1000-1700 cm^{-1} of IR spectra comes from the double degeneracy of ν_3. The further notations of the ν_3 splitting are assigned to a different group in the literature, where ν_{3a} and ν_{3b} are assignable to ν_{as} and ν_s of OCO group by Araiza et. al [80], or they are ascribed to

absorption coefficient is defined as the ratio of corresponding absorbances to the optical path length through the sample, and the molar absorption coefficient is the absorption coefficient normalised by the amount of concentration [77, 78]. However, the attenuation coefficient includes not only absorption coefficient but also the effects caused by scattering and luminescence, and it is interchangeable with the extinction coefficient [77, 78].

13: different states corresponding to the same energy level.

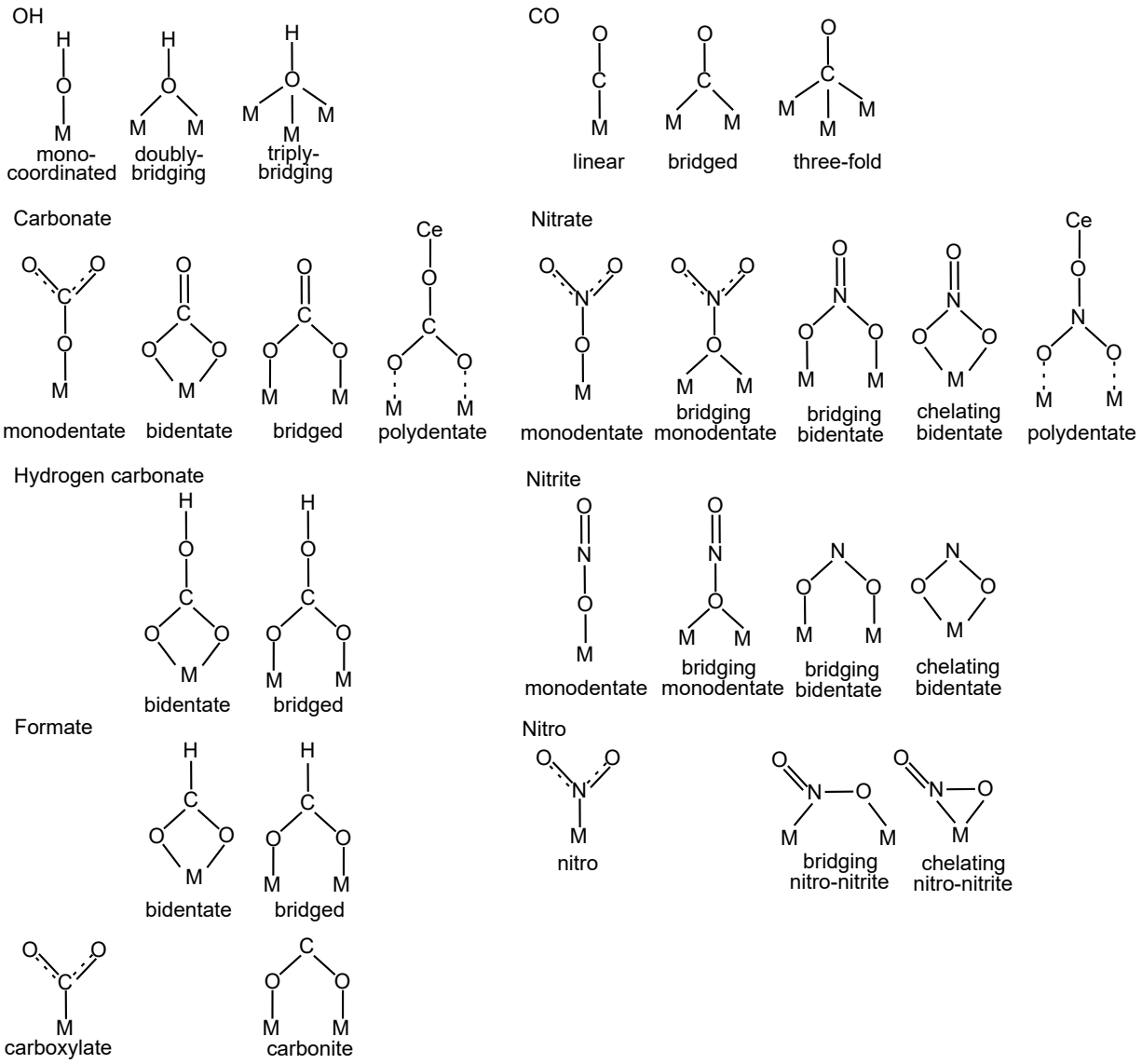

Figure 3.13: Adsorption configurations of surface carbonates with related species, surface nitrates with related species on metal oxides, as well as CO adsorption configuration on metals or metal oxides, where H represents for a hydrogen atom, O, for an oxygen atom, C, for a carbon atom, N, for nitrogen atom and M, for metal oxides and/or metals.

ν(C=O) and $\nu_{as}(CO_2^-)$ by Li et. al [81].

Adsorption configuration

The infrared peak position can also be affected by the adsorption configuration. The different adsorption configurations for OH, surface carbonates, and surface nitrate species adsorbed on metal oxides together with CO adsorbed on Pt are summarized in Figure 3.13. For OH species, three configurations with mono-coordinated, doubly-bridging, and triply-bridging OH species adsorbed on metal oxides or reduced oxides, ceria in our study, are found in the literature [82]. CO can adsorb on metals or metal oxides, Pt in our case, in linear, bridged, and three-fold configuration [83].

Carbonate species adsorbed on ceria are general in monodentate, bidentate, bridged, and polydentate configurations, which is analogous to nitrate species with monodentate, monodentate bridging, bridging bidentate (bridged), chelating bidentate (bidentate) and polydentate configurations [84, 85]. However, there is no such peak assignment found for the bridging monodentate species in the literature. Other carbonate and nitrate-related species can also be present during the CO/H_2O or CO/NO oxidation. Detailed peak assignments are listed and discussed in the *Result*.

Performing infrared measurements

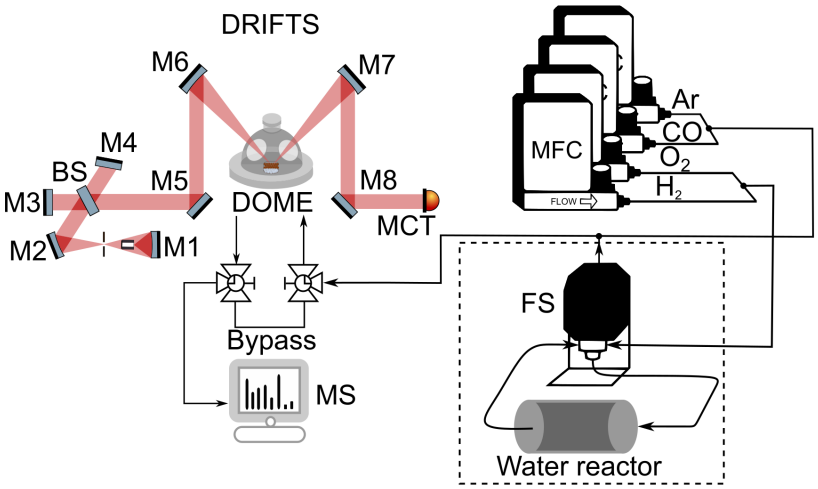

Figure 3.14: A schematic setup of DRIFTS, where M abbreviates for mirror with a movable mirror of M4, BS, for beam splitter, and MCT, for mercury-cadmium-telluride, FS, for fast switch, MFC, for mass flow controller, and MS, for the mass spectrometer. The setup design is credited to Felix Hemmingsson.

Transmission and reflectance modes can be performed in infrared spectroscopy. When the infrared beam incident on a rough sample surface, diffuse reflection occurs, which reflects in all directions rather than a specular direction. *In-situ* diffuse reflectance infrared Fourier transform spectroscopy (DRIFTS) is applied for probing adsorbed molecular species on the sample surface. In transmission mode, A can be expressed by Eq. 3.19, which is the logarithm of the reciprocal transmission. In diffuse reflectance mode, the pseudo absorbance, A', can be expressed in a similar way by Eq. 3.21. Infrared spectra are measured by a Michelson interferometer as shown in Figure 3.14, where a movable mirror can scan for $\Delta/2$ leading to a path difference of Δ, the intensities can be recorded for each mirror position. An interferogram can thus be generated and transformed into a spectrum using Fourier transform. Two instruments were used in this study, including VERTEX 70 and 80v. The major difference is that the optical bench of the 80v can be evacuated in order to remove atmospheric gases, e.g. CO_2 and H_2O, from the background. The feed gas was controlled by individual mass flow controllers (Bronkhorst) and a total gas flow of 100 ml/min was kept constant. IR spectra were collected in the range of 4400-700 cm^{-1} with a spatial resolution of 1 cm^{-1}. Background

$$T = \frac{I_0}{I_T} \tag{3.18}$$

$$A = \log_{10}\left(\frac{1}{T}\right) \tag{3.19}$$

$$R = \frac{I_0}{I_R} \tag{3.20}$$

$$A' = \log_{10}\left(\frac{1}{R}\right) \tag{3.21}$$

where T is transmittance, R, reflectance, I_0, the intensity of incident infrared light, I_T, the intensity of transmitted light, I_R, the intensity of reflected light, A, absorbance, and A', pseudo absorbance.

spectra were taken by averaging 100 scans, and sample spectra were 50 scans with a 6 mm aperture and 20 kHz scanner velocity. In order to perform water experiments, the water reactor was fitted into the 80v system, as shown in the dashed part of Figure 3.14. Only H_2 and O_2 gases were directly connected to the water reactor, and they were joined with the carrier gases Ar and CO after the water reactor and before the DRIFTS cell. An air-actuated high-speed gas valve (VICI Valco) was applied to switch between going through and bypassing the water reactor. When taking the background spectra, the system was in bypass, while the system was switched to the water reactor when the water experiments were carried out. All pipes were heated to 140 °C including the VICI Valco valve. The heating was crucial in order to avoid condensation of water in the gas line, which would lead to an unstable flow. Therefore, the stability of the water signal needed to be tested for a long duration since a slow condensation could also be expected from insufficient heating. Infrared spectra of adsorbates were obtained after subtracting a background taken at the same experimental condition but under a pure Ar flow.

Peak assignment

An example IR spectrum of CO adsorbed on Pt/alumina is presented in Figure 3.15. The vibrational band of gaseous CO is centered at 2150 cm^{-1} with P and R branches arising from $\triangle J = \pm 1$, and the rest of the peaks are assigned to different CO adsorption configurations depending on Pt particle size, and oxidation state [86]. The reason for the bridged configuration at a lower wavenumber compared to the linear one is an increased π-electron backdonation from larger Pt particles to CO molecules. In addition to the main characteristic peak, the splitting for ν_3, and overtones and combination modes can be used as criteria to assign the peaks [87].

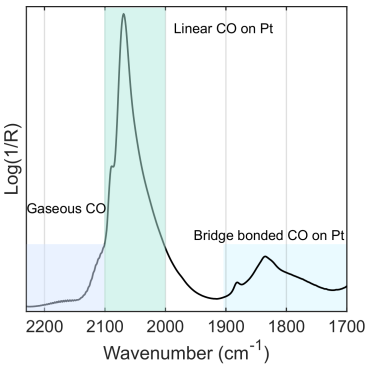

Figure 3.15: Infrared spectrum of CO adsorbed on Pt/alumina.

3.5.2 X-ray absorption spectroscopy

X-ray absorption spectroscopy (XAS), as a sample-averaged technique, unravels the structure and chemical state information on the atomic scale, and it can provide us with a deeper insight into the catalytic function. XAS is an absorption spectroscopy technique using X-rays with wavelengths around 0.1–50 Å. As displayed in Figure 3.16, multiple events are involved when X-rays incident on samples. The transmitted X-rays are detected in the same direction as the incident X-rays, and the core-holes[14] are generated after knocking out the inner shell electrons. If the core holes are filled by the electrons from higher energy levels, the energy difference between the energy levels is released in the form of emitted

14: the vacancy left after liberating the core electron of an atom

photons, named *fluorescence*, or this energy can also be transferred to other ejected electrons, termed *Auger electrons*. The production of *Auger electrons* can thus reduce the *fluorescence* yield. However, it can be increased with a higher atomic number. The radiation of *fluorescence* and *Auger electrons* can be detected in all directions. Other elastic and inelastic scattering events, such as diffraction by tightly or loosely bound electrons, could also happen. XAS could be operated in two modes, *transmission* and *fluorescence*. In *transmission* mode, the transmitted intensity, I, can be expressed by the *Beer-Lambert law*:

$$I(\lambda) = I_0(\lambda) \exp(-\mu x) \tag{3.22}$$

where I_0 is the incident X-rays intensity, λ, the corresponding wavelength, x, the sample thickness, and μ, the absorption coefficient of the sample, in cm^{-1}. A more general expression is in mass absorption coefficient, μ/ρ in cm^2/g, which is a wavelength-dependent coefficient. It decreases with decreasing incident wavelength, however, it increases dramatically at the energies which could eject inner-shell electrons to continuum state, thus an *absorption edge* is created. The absorption coefficient can also influence the intensity of *fluorescence* signal, I_f, and μ is proportional to I_f/I_0. Other characteristic emissions from the rest of the elements in the sample become the background of *fluorescence* signal, which can be removed by applying a proper detector with an appropriate wavelength range.

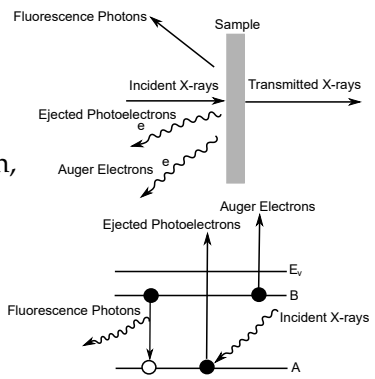

Figure 3.16: A schema of multiple events after X-ray absorption.

X-rays have enough energy to kick out inner shell electrons, and this energy is called the threshold energy of *absorption edge*, E_0. XAS can be divided into several regions in terms of the threshold energy, E_0 [88]:

- If $E < E_0$, the region is called *pre-edge*. Pre-peaks are generated by the transitions of core electrons to partially filled or unoccupied bound states,
- If $E \approx E_0$, the *edge* is introduced from the electronic transitions to empty energy levels and/or continuum states,
- If $E > E_0$, the X-ray absorption fine structure (XAFS) part is induced, and two regimes of X-ray absorption near edge structure (XANES) and extended X-ray absorption fine structure (EXAFS) are included. XANES is normally positioned around E_0 within ±10 eV, whereas EXAFS generally starts from 50 eV higher than E_0 [88]. The photoelectrons are knocked out with a kinetic energy of E_k=$E - E_0$, the wavelength of outgoing photoelectrons can thus be expressed in $\lambda_e = \frac{h}{\sqrt{2m_e(E-E_0)}}$, where m_e is the mass of an electron, and h the Planck constant.

The XAFS oscillation comes from the constructive and destructive

interference of the electromagnetic waves between the ejected photoelectrons and backscattered photoelectrons by the neighboring atoms. The constructive interference will increase the electron density, and a higher absorption probability can be achieved. Therefore, a transition from constructive to destructive interference gives an absorption variation from maximum to minimum. No XAFS can be observed for monoatomic gas due to the absence of neighboring atoms. Different regions are labeled in a XAS spectrum of liberating electrons from the 2p orbital of the Pt LIII edge in Figure 3.17 panel (a). Various information is provided by different regions. The *pre-edge* could provide information about coordination geometry,

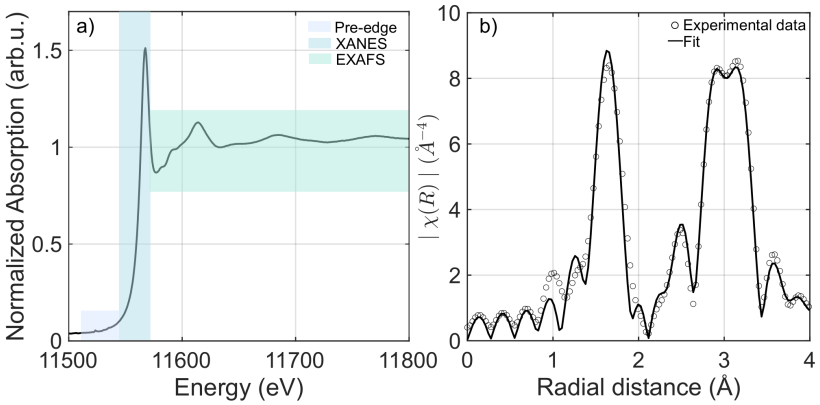

Figure 3.17: XAS spectra of PtO_2 powder sample in *fluorescence* mode (a) and its Fourier transformation with a fit (b).

and the position of the *absorption edge* in XANES, termed *whiteline*, could indicate a higher or lower oxidation state compared to standard references with a known oxidation state, such as metal foil. The inner shell electrons of the element with a higher oxidation state are attracted by more coulombic forces from nuclei than a lower oxidation state. More energy is required to liberate the inner shell electrons, and an increased absorption probability comes from additional unoccupied energy levels. Thus, the position of the *whiteline* shifts to higher energy and a stronger whiteline intensity (WLI) would be expected for a higher oxidation state.

EXAFS is sensitive to the local structure including the distance to the neighboring atoms and the coordination number of the near neighbors. The oscillation in EXAFS region, $\chi(k)$, can be quantitatively analysed by EXAFS equation:

$$\chi(k) = \sum_{j} A_j(k)\sin[2kR_j + \phi_j(k)] \tag{3.23}$$

where $A_j(k)$ is the backscattered amplitude from atoms in the jth shell, R_j, the distance between atoms in the jth shell and absorbing atom, and $\phi_j(k)$, the phase shift caused by coulomb interaction between atoms in the jth shell and absorbing atom, k, the wavenumber can be determined from $\frac{2\pi}{\lambda_e}$. Moreover, this equation can be extended after taking multiple scattering into

consideration:

$$\chi(k) = \sum_j \frac{N_j \cdot S_0^2(k)}{k \cdot R_j} \mid f_{eff}(k)_j \mid \cdot \exp(-2k^2\sigma_j^2) \cdot \exp[\frac{-2R_j}{\wedge(k)}]\sin[2kR_j + \phi_j(k)] \tag{3.24}$$

where N_j is the number of backscatters in *jth* shell, $S_0^2(k)$, the relaxation of the absorbing atom after the removal of the electron, $f_{eff}(k)_j$, the effective amplitude of single scattering path, σ_j, the Debye-Waller factor describing thermal disorder, and $\wedge(k)$, the mean free path of photoelectrons. EXAFS analysis is carried out by fitting theoretical scattering pathways into background subtracted experimental data. The theoretical paths are constructed based on the crystalline structure of metal or metal oxides, and several parameters in Eq. 3.24 are determined from *ab initio* theoretical calculations, $f_{eff}(k)_j$, $\phi_j(k)$, $\wedge(k)$, and R_j. Fine-tuning of parameters: R_j, N_j, and σ_j to mitigate the difference between experimental data and the theoretical model. S_0^2 is normally obtained by fitting a standard reference sample with a known crystalline structure under the same experimental setup, and this value is generally around 0.7- 1.1 [88]. Nonetheless, it can be higher in transmission mode because of a strong fluorescence signal or lower in fluorescence mode coming from the self-absorption effect. Furthermore, experimental conditions could also play a role. After the Fourier transform of the EXAFS spectrum, the contributions from heavy or light elements can be easily discerned. A Fourier transformed EXAFS spectrum of PtO_2 powder in the radial distance (without phase correction) is shown in Figure 3.17 panel (b). The Pt-O and Pt-Pt contributions are located at different radial distances. The Pt-O radial distance is positioned at 1–2 Å, and the Pt-Pt scattering paths are situated at around 3 Å.

Although XAS is an effective state-of-art technique of revealing catalytic structure, however, it is hard to qualitatively differentiate the XANES and EXAFS spectra for small oxidized platinum clusters in subnanometer and atomically dispersed platinum catalysts [89]. Therefore, a uniform sample containing an exclusive single platinum atom becomes difficult to examine.

3.6 Scattering

Scattering involves processes of moving particles being forced to deviate from their trajectories due to particles-particles collisions. It can be divided into elastic and inelastic scattering regarding the energy losses during collisions. X-ray diffraction can thus be classified as a coherent elastic scattering of X-rays by crystal atoms, and the terms “diffraction” and “scattering” are sometimes interchangeable.

3.6.1 X-ray diffraction

The diffraction pattern is formed from the intensity distribution when an optical wave transmits through an aperture. It originates from the constructive and destructive interference of the diffracted X-rays. The constructive interference is obtained at a specific angle, named *Bragg angle* θ. At this angle, the optical path difference of incident X-rays equals a multiple of the incident wavelength (λ), which can be expressed in Bragg's law:

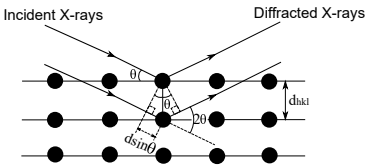

Figure 3.18: Scheme of Bragg's law.

$$n\lambda = 2d \sin\theta \tag{3.25}$$

where n is a positive integer, and d, the interplanar spacing. This phenomenon also occurs when the wavelength of X-rays is in the same order of magnitude as the interplanar spacing, termed X-ray diffraction (XRD), and the schema is presented in Figure 3.18. Further, the mean crystallite size, τ, can be calculated from the Scherrer equation:

$$\tau = \frac{K\lambda}{\beta \cos\theta} \tag{3.26}$$

where λ is X-ray wavelength (1.54 Å for Cu-Kα), β, the peak broadening of half-maximum intensity at 2θ, in radians, and K, a dimensionless shape factor. A perfect crystallinity without any instrumental broadening is assumed by the Scherrer equation, however, any crystalline defects, e.g., vacancies, dislocation, or substitution, could lead to additional broadening. Smaller particles with more crystalline defects can thus produce a broader linewidth as compared to larger particles.

3.6.2 High-energy X-ray diffraction

In XRD, the reciprocal lattice is commonly used to analyze periodic structures as the diffractograms can directly reflect the structure change regardless of instrumental light sources. The reciprocal vectors of the lattice, associated with the wavevector difference between incoming and diffracted X-rays, can be determined by the diffraction pattern of a crystal. The atomic arrangement can thus be inferred. The reciprocal lattice is the Fourier transform of the Bravais lattice[15], and it thus exists in the spatial frequency domain, termed reciprocal space or k space, where k is wavevector. The reciprocal space plays a similar role in obtaining a frequency domain from the Fourier transform of a time-dependent domain. Analogously, the periodicity of the real space can be represented by the wavevectors of reciprocal lattice in the k space. Therefore, the reciprocal space provides a way of visualizing the wavevectors which can be mathematically derived from Laue equations, where q_{hkl}

15: from specific directions, the lattice appears exactly in the same way from any of the discrete lattice points from any directions

$=k_{out}$-k_{in}, termed scattering vector, linking the difference between incoming and outgoing waves of an elastic scattering by a crystal lattice. The q_{hkl} can be further expressed as:

$$q_{hkl} = \frac{2\pi n}{d} \tag{3.27}$$

where n are natural integers, d, the interplanar spacing. This expression can be explained in such a way that the incoming and outgoing waves have the same phase at the lattice points where the oscillations of the crystal atoms are resonated with. The diffractograms become comparable in the way of wavelength/instrumental independence as compared to the expression of Bragg's law. q_{hkl} can be further derived from Bragg's law:

$$q_{hkl} = \frac{4\pi}{\lambda} \sin(\theta) \tag{3.28}$$

In this study, the Pt/FeO_x catalysts were studied by conventional lab X-ray sources and *in-situ* HEXRD using a synchrotron facility with the plate reactor described above. The oxidation and reduction pulsing experiments with 2 vol.% O_2 and 2 vol.% H_2, O_2 modulation with both 0.2 vol.% CO and 5 vol.% O_2, and 1 vol.% CO and 4 vol.% O_2, and CO modulation with 1 vol.% CO and 4 vol.% O_2 were performed at 150, 250 and 350 °C, respectively.

Results and discussion 4

In Paper I & III, as-prepared supported Pt catalysts with different Pt particle sizes on non-reducible and reducible supports, Pt_{small}/alumina, Pt_{large}/alumina and Pt/ceria, were investigated with respect to physicochemical properties and in Paper IV the spent catalysts after reaction with H_2O and NO were characterised. Kinetic studies together with theoretical calculations were carried out to investigate the possible reaction mechanisms for CO oxidation over Pt_{small}/alumina and Pt_{large}/alumina in Paper I, and over Pt/ceria in Paper II. The kinetic studies were performed solely for CO/H_2O oxidation and CO/NO oxidation over Pt/alumina and Pt/ceria in Paper IV. The evolution of surface species in terms of temperature was explored by infrared spectroscopy for CO oxidation in Paper III, and for CO/H_2O oxidation and CO/NO oxidation in Paper IV. The local structure and long-range order were scrutinized by XAS and HEXRD in Paper III & V, respectively.

4.1 Catalyst physicochemical properties 35
4.2 Kinetic behaviour . . . 39
4.2.1 Ignition and extinction behaviours 39
4.2.2 Linking to microscopic reaction mechanisms . 40
4.3 Catalytic functionality 43
4.3.1 Evolution of surface species 43
4.3.2 Local structure and long-range order 52
4.4 How to design CO oxidation catalysts? . . 57

4.1 Catalyst physicochemical properties

Before the investigation on the kinetics and catalytic functionality, a description of the basic characteristics of the as-prepared 1 wt% Pt/ceria and reference 2 wt% Pt_{small}/alumina and Pt_{large}/alumina catalysts are summarized in Table 4.1 in Paper I & III, and the comparison with the properties of spent catalysts after the CO/H_2O and CO/NO oxidation are discussed in Paper IV.

Table 4.1: Specific surface area (SSA) of catalysts and metal (SSA_{Pt}), Pt loading (X_{Pt}), metal dispersion (D_{Pt}), Pt particle size (d_{Pt}), and support particle size ($d_{support}$) for Pt/ceria and Pt/alumina.

	SSA /$m^2g_{cat}^{-1}$	X_{Pt} /wt%	$d_{support}$ /nm	d_{Pt}^{a} /nm	SSA_{Pt} /$m^2g_{cat}^{-1}$	D_{Pt} /%	d_{Pt}^{b} /nm	d_{Pt}^{c} /nm
1wt% Pt/ceria	131	1.06	8	/	1.92	73	1.5	1.0± 0.2
2wt% Pt_{small}/alumina	140	1.91	6	/	2.65	56	2.0	1.3± 0.4
2 wt% Pt_{large}/alumina	132	1.80	6	20	0.12	2.7	42	/

[a] Pt crystallite size; Calculated from XRD measurements
[b] Pt particle size; Obtained from CO chemisorption
[c] Pt particle size; Analysed from STEM images

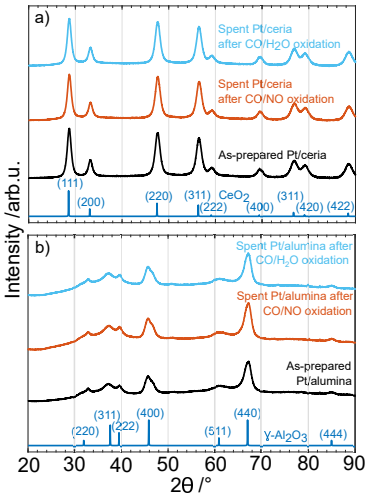

Figure 4.1: XRD patterns of the spent Pt/ceria in (a) and Pt/alumina in (b) after CO oxidation with H_2O (blue) and NO (orange), and as-prepared Pt/ceria and Pt/alumina catalysts (black). Reflection assignments are assigned using reference patterns (blue) from the Powder Diffraction File^{TM} (PDF) database for CeO_2 (PDF 00-004-0593) and γ-Al_2O_3 (PDF 00-010-0425).

The SSA for the Pt/ceria, Pt_{small}/alumina and Pt_{large}/alumina sample is 131, 140 and 132 m^2/g_{cat}, respectively. These values match with the typical values for microporous materials, which mainly contribute to the SSAs. The lower SSA for Pt_{large}/alumina might be due to a higher calcination temperature. The Pt loadings of Pt/ceria, Pt_{small}/alumina and Pt_{large}/alumina are close to the expected ones. Figure 4.1 shows the diffractogram for as-prepared Pt/ceria and Pt_{small}/alumina is analogous to the pattern for the spent Pt/ceria and Pt_{small}/alumina, which matches the reference pattern for γ-alumina (PDF 00-010-0425) and fluorite CeO_2 (PDF 00-004-0593), respectively. No noticeable changes are observed in crystallinity before and after reactions. The apparent crystallite sizes for the support materials are calculated using the Scherrer equation, to be 8 nm for ceria and around 6 nm for alumina before and after reactions. More specifically, the crystallite size for Pt_{small}/alumina is determined to be 6 nm after CO/H_2O oxidation and to be 7 nm after CO/NO oxidation. Also, the crystallite size of support materials can be imaged by TEM in Figure 4.2. Around 10 nm crystallite sizes are revealed for ceria and alumina for the as-prepared samples, and after reactions, the crystallite sizes of 7 and 10 nm are observed for ceria and alumina, respectively. A larger deviation could be expected from TEM due to the selected analysis regions and further complicated by the arbitrary orientations of the powder grains and the polycrystallinity nature of the agglomerated particles with different orientations of crystal planes. Further, the employed Scherrer equation is used assuming no instrumental broadening and a perfect crystallinity. Nonetheless, the crystallite sizes calculated from PXRD are in good agreement with the observations from TEM. Regarding the Pt phase, a clear Pt phase is observed for the diffractogram of Pt_{large}/alumina, which is reckoned to be 20 nm. No visible Pt phase can be observed for the rest of the diffractogram, indicating the majority of the Pt crystallites could either be too few to be detectable or too small and/or amorphous to produce diffraction [90]. From the CO chemisorption, the specific Pt area for as-prepared Pt/ceria is 1.92 m^2/g_{cat} with 73% dispersion. Whereas, a higher specific Pt area for as-prepared Pt/ceria with a lower dispersion of 56%. The averaged Pt particle size is 1.5, 2, and 42 nm for as-prepared Pt/ceria, Pt_{small}/alumina and Pt_{large}/alumina, respectively. The presence of Pt particles can also be observed by electron microscopy measurements. Figure 4.2 displays the micrographs of TEM and STEM before and after reactions where the Pt particle size distribution (PSD) is analysed. For Pt/ceria catalysts, the Pt particles are not clearly revealed in TEM images. This partially comes from the small mass difference between Pt and Ce, and in part, due to a poor mass-thickness contrast. Whereas, the Pt particles can be discerned from STEM

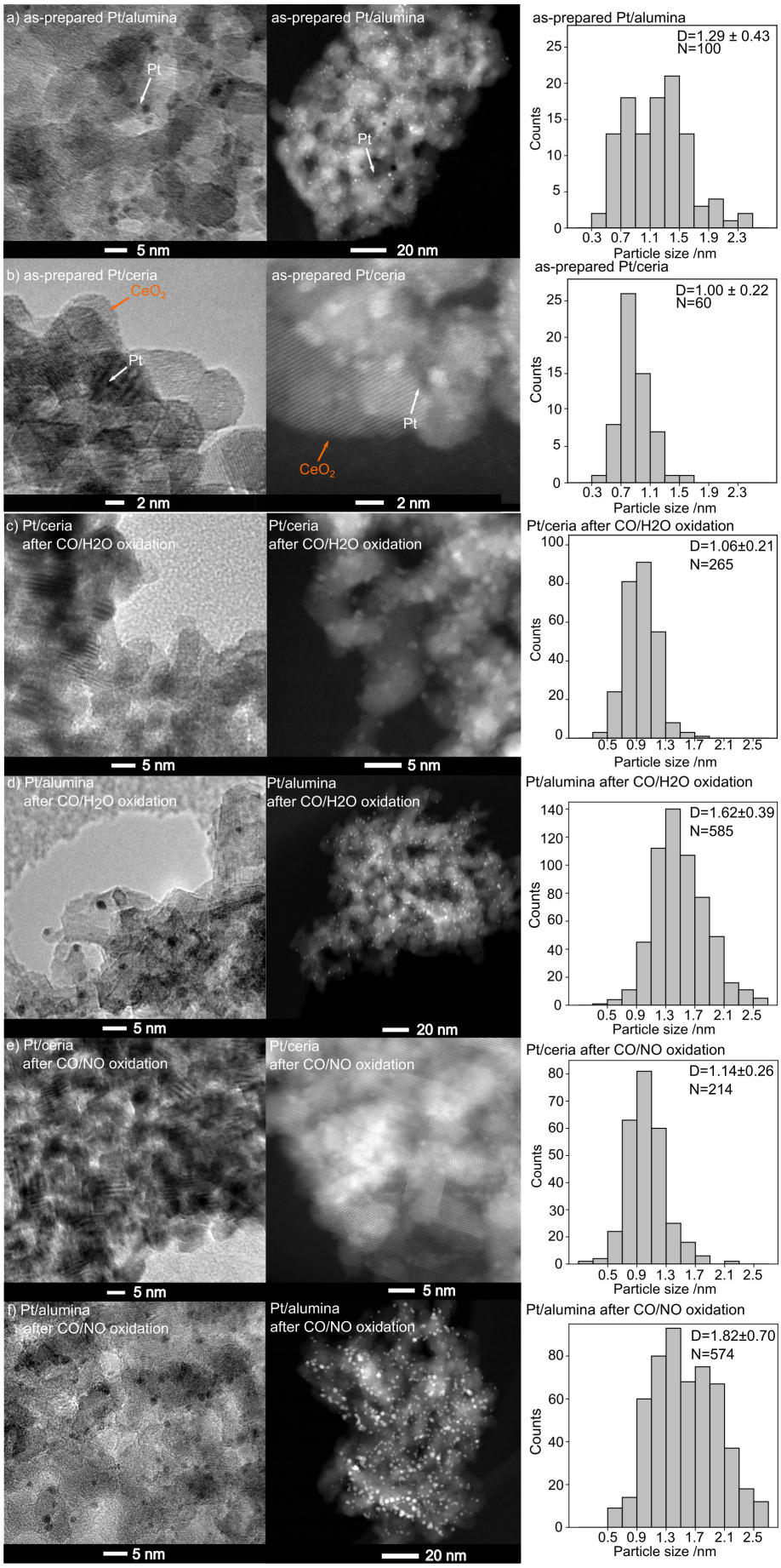

Figure 4.2: High-resolution TEM and STEM-HAADF micrographs of the as-prepared Pt/ceria (panel a) and Pt/alumina (panel b), the spent Pt/ceria (panel c) and Pt/alumina (panel d) catalysts after CO oxidation with H_2O, and the spent Pt/ceria (panel e) and Pt/alumina (panel f) after CO oxidation with NO.

images thanks to the difference in the Z number. The majority of Pt particles range from 0.8 to 1.2 nm with a mean Pt particle size of 1 nm for as-prepared Pt/ceria. The Pt particles appear in a wider range within 0.7-1.5 nm. After reactions, the majority of the Pt particles are in the range of 0.5-1.3 nm with the same mean Pt particle size of 1 nm in comparison with as-prepared Pt/ceria. As for Pt/alumina after reactions, the Pt particles mainly fall in a broader range of 0.7-2.5 nm with a larger mean particle size of 1.62 and 1.82 nm for CO/H_2O and CO/NO oxidation, respectively. This could be as a result of a potential agglomeration after the reactions. The results from PSD analysis agree with the results of the Pt phase of not being visible from PXRD. Therefore, there is no such observation of sintering for Pt particles and significant change for the support.

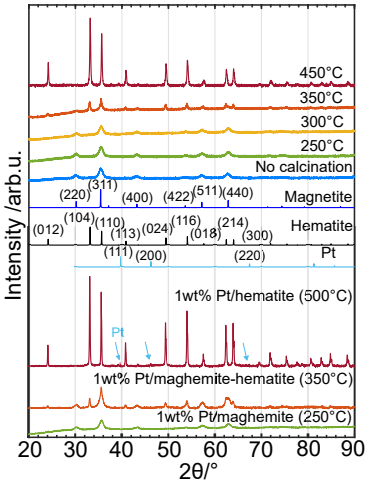

Figure 4.3: XRD patterns of the iron oxide without calcination and calcined at different temperatures, and subsequent calcination at different temperatures after loading Pt. Reflection assignments are assigned using reference patterns from the Powder Diffraction File^{TM} (PDF) database for Pt (PDF 00-004-0802), magnetite (PDF 00-065-0731), and hematite (PDF 04-003-2900).

Commenting on the properties of iron oxide described in Paper V, different types of drying methods including rotation evaporator at 40 °C, freeze drying, vacuum drying at room temperature or 60 °C were used. Among these, vacuum drying at room temperature and freeze drying exhibit the highest surface area of around 120 m^2/g, and the rest show a slightly lower surface area of roughly 110 m^2/g. After drying, the precipitates are further calcined at 250, 300, and 350 °C resulting in a surface area of 120±0.8, 103±0.2 and 67±0.6 m^2/g. The diffractograms of iron oxides calcined at different temperatures as well as the reference patterns of magnetite (PDF 00-065-0731) and hematite (PDF 04-003-2900), are displayed in Figure 4.3. One can clearly see that different iron oxide phases are present as a result of different calcination temperatures. The diffractograms of iron oxides without calcination, calcined at 250 and 300°C match the phase of magnetite and maghemite. Maghemite exhibits an analogous XRD pattern to the one of magnetite coming from a similar crystal structure but with a different oxidation state after oxidation. Whereas, the diffractogram of iron oxides calcined at 350°C displays a mixed phase between maghetite and hematite, and the one calcined at 450 °C matches the reference pattern of hematite, which signifies a complete phase transition from maghemite to hematite at 450°C. Based on the diffractograms, the crystallite sizes of different types of iron oxides are calculated to be 12, 13, 20, and 27 nm for iron oxide without calcination, calcined at 250, 300, and 350°C, respectively. After loading the Pt precursor on the support of maghemite, the Pt loading for 1 wt% Pt/maghemite is measured to be 1.2 wt% and for 1 wt% Pt/hematite is 0.8 wt%. Further calcination after loading Pt is carried out at 250, 350, and 500 °C. The resulting diffractograms show a maghemite, maghemite-hematite, and hematite phase, respectively. No visible Pt phase for a calcination temperature at 250 and 350°C and a weak Pt phase is observed when calcined at 500 °C. SEM micrographs display a different morphology for iron

oxides calcined at different temperatures and the Pt particles can be observed for both Pt/maghemite and Pt/hematite from STEM images.

4.2 Kinetic behaviour

4.2.1 Ignition and extinction behaviours

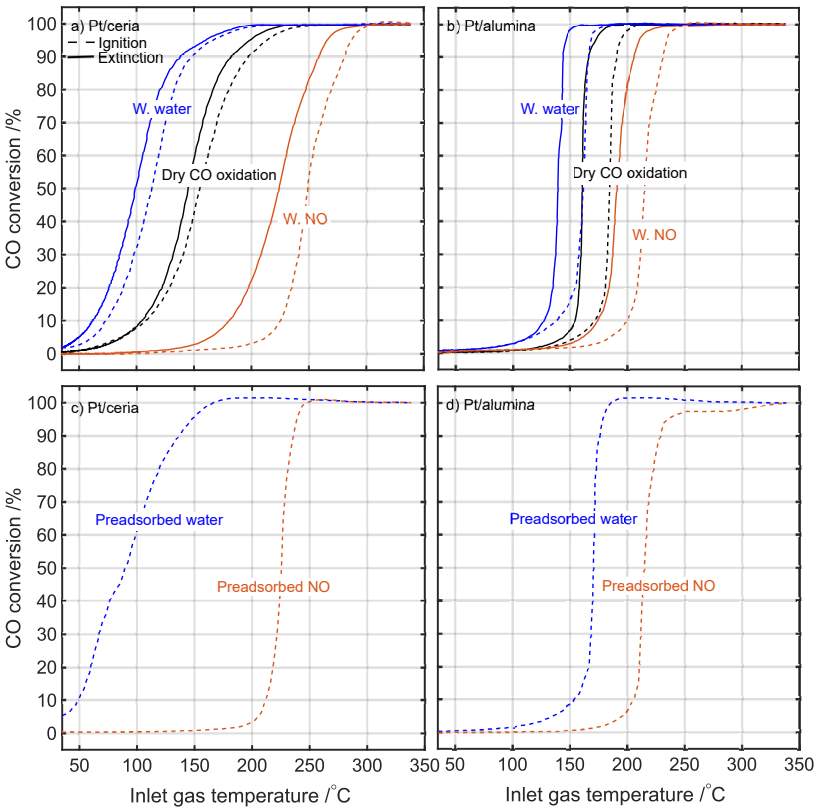

Figure 4.4: Ignition (dashed lines) and extinction (solid lines) profile over Pt/ceria (panel a) and Pt/alumina (panel b) for dry CO oxidation (black) with 0.2 vol.% CO and 1 vol.% O_2, CO oxidation with 2 vol.% H_2O (blue) and 300 ppm NO (orange). Ignition profile over Pt/ceria (panel c) and Pt/alumina (panel d) with pre-adsorbed H_2O (blue) and NO (orange) followed by dry CO oxidation with 0.2 vol.% CO and 1 vol.% O_2.

The kinetics of CO oxidation over the catalysts is reflected by the ignition and extinction behaviors in Paper IV. Figure 4.4 shows the CO conversion profiles in the presence of either H_2O or NO, dry CO oxidation as a reference, over Pt/ceria (panel a) and Pt/alumina (panel b) during heating (ignition)-cooling (extinction) ramps, and the CO oxidation profiles after H_2O or NO pre-adsorption are displayed in panel c and d. It is clear that the hysteresis moves to a lower temperature for CO/H_2O oxidation over Pt/ceria as compared to dry CO oxidation. On the contrary, the hysteresis shifts towards a higher temperature for CO/NO oxidation. The temperatures where 50% conversion is reached, termed T_{50}, which is 155 °C for dry CO oxidation during ignition. This is shifted to 114 °C by H_2O and to 248 °C by NO. For the extinction process, the T_{50} decreases from 145 °C for dry CO oxidation to 99 °C by H_2O and increases to 224 °C by NO. The differences between T_{50}s from ignition and extinction is 10, 15 and 24 °C for dry CO oxidation,

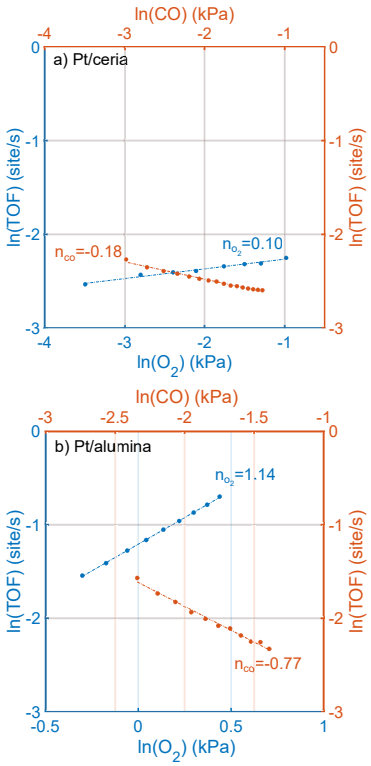

Figure 4.5: CO and O_2 pressure dependencies of the turnover frequency over Pt/ceria (panel a) performed at 125 °C and Pt/alumina (panel b) at 145 °C. The reaction orders were obtained by linear fitting.

CO/H_2O and CO/NO oxidation, respectively. The activity of CO oxidation is significantly enhanced by H_2O and inhibited by NO for Pt/ceria, which is in line with the previous studies [36, 91]. The enhanced activity from H_2O suggests that H_2O can surpass the CO self-poisoning by the complementary reaction pathways from the interfacial sites. One possibility is that the strong CO adsorption on ionic platinum, considered as spectator species, can be weakened by the co-adsorption of H_2O and OH species. Another possibility is the reaction occurs via other reaction pathways with a lower activation barrier. Whereas, the NO inhibition may come from the competitive adsorption between CO and NO on Pt sites. A further blockage for the interface sites may proceed from the formation of the nitrate and carbonate species. The H_2O promotion can also be manifested by the CO oxidation profile after pre-adsorbed H_2O with a noticeable CO conversion at 35 °C. The T_{50} is 90 °C, which is lower than the one with co-feeding H_2O. This can be explained by the higher availability of OH species at the interfacial sites for pre-adsorbed H_2O, whereas competitive adsorption between CO and H_2O on Pt particles may proceed when co-feeding CO and H_2O. Likewise, a lower T_{50} is expected for the pre-adsorption with NO as compared to co-feeding with NO since NO desorbs at critical temperatures for pre-adsorbed NO. As opposed to Pt/ceria, a sudden change in the ignition-extinction profiles and lower conversion are observed at low temperatures because of more prone to CO self-poisoning for Pt/alumina. The T_{50}s are, in general, at higher temperatures for Pt/alumina as compared to Pt/ceria. For extinction, T_{50} deviates from 161 to 139 °C by H_2O and to 191 °C by NO exhibiting an identical influences by H_2O and NO but to a less extent. This signifies the support effect where the interface sites provide the possibility of other reaction pathways by H_2O as well as the probability of being blocked by nitrates. Therefore, the lower activation by H_2O and deactivation by NO for Pt/alumina are largely due to the absence of interface sites. This can also be evidenced by a similar T_{50} of ignition profile with pre-adsorbed NO and co-feeding NO. Coming to the ignition, T_{50} moves from 185 to 161 °C by H_2O and to 215 °C by NO. The T_{50} of ignition after the H_2O pre-adsorption appears to be 171 °C, which is lower than for dry CO oxidation but higher than for CO/H_2O oxidation. This can be an indication that H_2O may play a distinctive role in CO oxidation for Pt/ceria and Pt/alumina.

4.2.2 Linking to microscopic reaction mechanisms

The reaction order measurements are performed for dry CO oxidation over Pt/ceria and Pt/alumina in a low conversion region below 22%, where the reaction rate is controlled by kinetics in

Paper II. The O_2 and CO reaction order for CO oxidation for Pt/ceria is measured to be 0.10 and -0.18, respectively, in Figure 4.5. This could be an indication for the Mars-van Krevelen mechanism and can be further validated by kinetic Monte Carlo simulations with parameters evaluated from DFT calculations based on a rod model with 32 Pt atoms exposing Pt(111) surface to CeO_2 (111) surface. The detailed reaction pathways include CO adsorption, desorption, and diffusion, and O_2 dissociative adsorption and desorption, and diffusion. CO_2 could be formed from the reaction between adsorbed CO and adsorbed atomic oxygen or lattice oxygen. Oxygen vacancies are thus created and can be refilled by the molecularly adsorbed oxygen, which further reacts with adsorbed CO to generate CO_2. Opposite to Pt/ceria, the reaction orders for CO oxidation over Pt/alumina are 0.62 for O_2 and -1.09 for CO, which follows the Langmuir-Hinshelwood mechanism. The

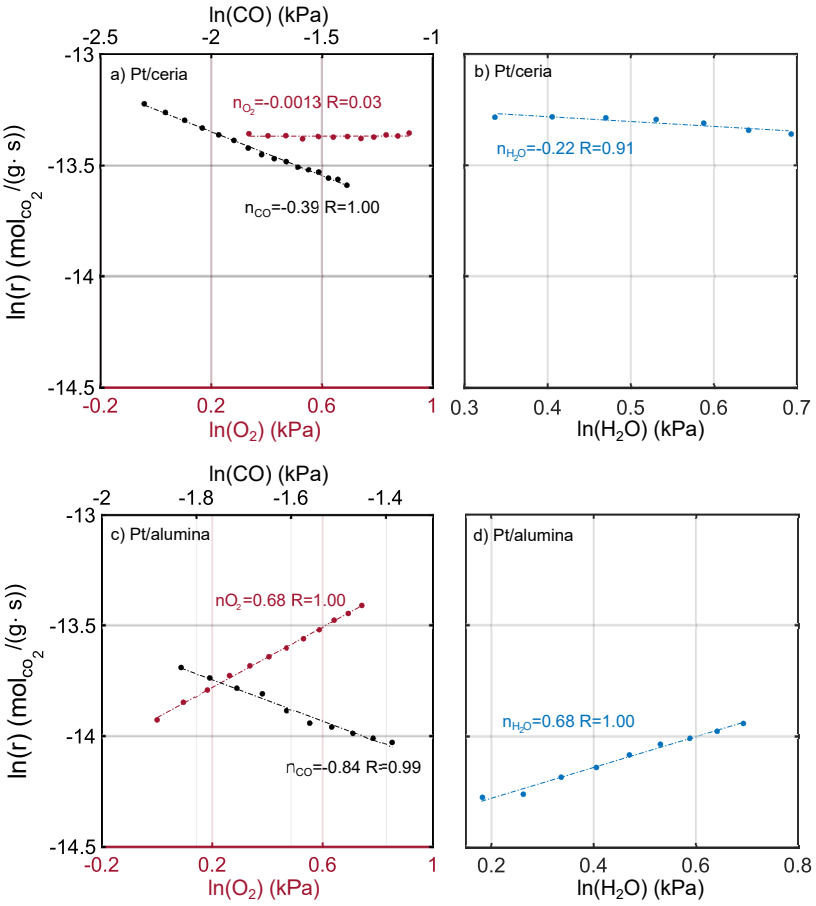

Figure 4.6: CO, O_2 and H_2O pressure dependencies of the reaction rates over Pt/ceria (panel a,b) performed at 45 °C and Pt/alumina (panel c,d) at 127 °C. The reaction orders were obtained by linear fitting.

reaction order measurements are further performed for CO/H_2O oxidation over Pt/ceria and Pt/alumina with respect to CO, O_2 and H_2O as shown in Figure 4.6. The CO, O_2, and H_2O reaction order is -0.39, 0.0013, and -0.08, respectively, for CO oxidation over Pt/ceria. These results suggest a promoted Mars-van Krevelen mechanism via new reaction pathways [92, 93], which includes adsorbed CO reacting with OH species from H_2O dissociation forming carboxyl (COOH) on Pt. CO_2 and H_2O can be generated

by a further reaction with $O_{lat}H$ using the lattice oxygen at the interface. Afterward, the vacancies can be refilled in a similar way as mentioned above. However, these reaction pathways show there is no H_2O consumed in the reaction cycle. This is in line with our measurements of the H_2O reaction order of -0.08, which is close to 0. The H_2O concentration exhibits barely dependency on the reaction rate, however, it is crucial for the availability of OH species. This can be the explanation for a lower ignition temperature with pre-adsorbed H_2O than co-feeding with H_2O since competitive adsorption between CO and H_2O on the Pt particles may hinder the CO oxidation reaction rate. As for Pt/alumina, the CO reaction order is -0.84 and O_2 reaction order is 0.68, and H_2O reaction order is 0.25. This suggests a Langmuir-Hinshelwood reaction mechanism for Pt/alumina and the influence of the amount of H_2O on the reaction rate when the H_2O concentration is between 0.8 to 2 vol.%. One possible reaction mechanism is that the suggested COOH still can be formed but CO_2 is generated via proton exchange with H_2O and OH [94]. Another explanation is that H_2O can probably weaken the CO adsorption on Pt sites and lower the reaction barrier of CO/H_2O oxidation [95, 96]. Although unlikely, the CO_2 production can also be generated from the decomposition of bridged hydrogen carbonate (br-(CO_2)OH) species. Therefore, H_2O may play a distinctive role for CO oxidation over Pt/ceria and Pt/alumina.

Additionally, the reaction order measurements are performed for Pt_{small}/alumina and Pt_{large}/alumina under lean and rich conditions, and the reaction orders are summarized in Table 4.2 in Paper I. The lean reaction order for CO and O_2 at 145 °C is -0.75 and 0.68, respectively. For the rich conditions at 265 °C, the CO reaction order is -0.76, whereas the O_2 reaction order becomes 1.01, as same as the one observed at 275 °C. The discrepancy in O_2 reaction order might come from a low CO conversion of 6-16% for the lean and rich conditions. However, for the rich conditions, the O_2 conversion is 27-30%, which means oxygen mass transfer limits the CO conversion, and the O_2 reaction order can thus become 1. For the Pt_{large}/alumina catalyst, the lean reaction order for CO is -0.77 at 215 °C and -0.78 at 235 °C. The O_2 reaction order is 1.03 at 195 °C and 1.14 at 215 °C. In rich conditions at 325 and 340 °C, the CO reaction order is -0.9 and -0.99, respectively, while the O_2 reaction order is 1.16 at 325 °C. The reaction orders under rich conditions are measured below 10% CO conversion, which leads to an O_2 conversion of 7-12%. No matter whether under lean or rich conditions, an O_2 reaction order of around 1 is obtained, and the CO reaction order becomes closer to -1 from lean to rich conditions. In order to validate this, computational analysis of reaction orders is performed using micro-kinetic modeling based on different reaction paths and different types of assumptions for adsorbate-adsorbate interaction. The

Catalysts	Conditions				Reaction orders	
	Mixture	p(CO) (kPa)	p(O_2) (kPa)	Temperature (°C)	n_{co}	n_{o_2}
Pt_{small}/alumina	Lean	0.14-0.335	2	418	-0.75	
	Lean	0.05	0.63-1.11	145		0.68
	Rich	0.21-0.37	0.1	265	-0.76	
	Rich	0.2	0.02-0.07	265		1.01
	Rich	0.2	0.02-0.06	275		1.01
Pt_{large}/alumina	Lean	0.095-0.245	2	215	-0.77	
	Lean	0.17-0.305	2	235	-0.78	
	Lean	0.05	0.73-2.03	195		1.03
	Lean	0.05	0.73-1.53	215		1.14
	Rich	0.22-0.33	0.1	325	-0.90	
	Rich	0.21-0.37	0.1	340	-0.99	
	Rich	0.2	0.015-0.085	325		1.16

Table 4.2: Reaction orders over Pt_{small}/alumina and Pt_{large}/alumina under lean and rich conditions.

reaction pathways include the classical Langmuir-Hinshelwood mechanism with only dissociatively adsorbed oxygen, extended Langmuir-Hinshelwood including both dissociative and molecular oxygen adsorption, and one site O_2 adsorption and dissociation. Different models for adsorbate-adsorbate interactions of linear and non-linear dependency on coverage for the adsorption energy are considered. Another possibility is to employ a quasi-chemical approach, which describes the ad-species arrangement caused by lateral interactions.

4.3 Catalytic functionality

The ad-species during reaction conditions with decreasing temperatures (extinction) are explored by IR spectroscopy in Paper III for dry CO oxidation, and both ignition and extinction are investigated in Paper IV for CO/H_2O and CO/NO oxidation. Detailed peak assignments based on different adsorption configurations employed in this study are listed in Table 4.3.

4.3.1 Evolution of surface species

CO oxidation

In Figure 4.7, panel a and c display the wavenumber region for CO_2 gas phase as a product of catalytic reaction with CO conversions measured by mass spectroscopy, panel b and d show a spectral region of different CO ad-species on Pt/ceria and Pt/alumina. Starting from the highest temperature for the Pt/ceria catalyst, an obvious CO_2 production together with a maximum intensity of $\tilde{\nu}_{gas}^{CO_2}$ can be observed. Meanwhile, an absorption peak at 2107 cm^{-1} with a fwhm of 20-30 cm^{-1} can be clearly noticed and can be assigned to linear CO adsorbed on ionic platinum ($\tilde{\nu}_{lin}^{CO}(Pt^{2+})$). This species can be considered as a spectator in the presence of CO and O_2, and the CO gas phase appears to be in equilibrium with the band intensity, which increases with lowering temperatures.

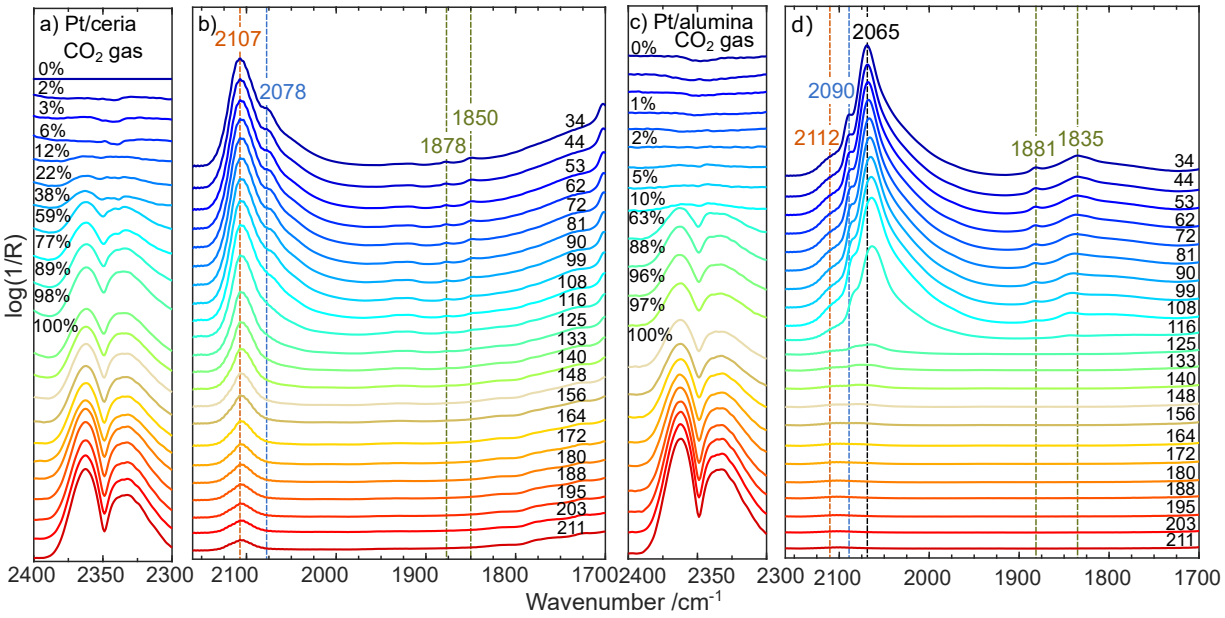

Figure 4.7: *Operando* spectroscopic results for Pt/ceria (panel a,b) and Pt/alumina (panel c,d) during catalytic CO oxidation extinction. CO_2 gas phase spectra with noted CO conversions measured with mass spectrometry (panel a,c) and spectral region for CO adsorbed on Pt (panel b,d) with sample temperatures in °C in presence of 0.2 vol.% CO and 1 vol.% O_2.

However, the assignment of this peak is ambiguous since the difficulties lie in the distinguishing atomically dispersed platinum and oxidised platinum clusters or PtO_x patches on particles experimentally due to the non-uniformity of sample [89, 97]. This peak can be assigned to CO adsorbed on atomically dispersed platinum due to the character of being catalytically inactive, however, a sharper peak is expected for this species prepared by a sol-gel method and incipient wetness impregnation with a hydrothermal post-treatment [98, 99]. Contradictorily, the IR peak at 2095 cm^{-1} is assigned to CO adsorbed on oxidised platinum clusters [89] rather than atomically dispersed platinum. Whereas, the bond between CO and atomically dispersed platinum is shown to be weak for catalysts prepared by incipient wetness using strong electrostatic adsorption, which is more comparable to the catalysts used in this study [89]. Likewise, CO adsorbed on rather oxidised platinum particles at 2112 cm^{-1} appears to be close to the peak in this study [26]. Therefore, the peak in our study is closer to the case of CO adsorbed on oxidised platinum clusters and/or PtO_x patches on particles, where the CO adsorbed on platinum could react with the O from platinum oxides for CO oxidation, although the present result is proved to catalytically inactive platinum oxides [100]. With decreasing temperatures, a smooth decay is observed for the intensity of the $\tilde{\nu}_{gas}^{CO_2}$ band together with a continuous grow of $\tilde{\nu}_{lin}^{CO}(Pt^{2+})$ band. Reaching 125 °C, less CO_2 is produced, and a shoulder at 2078 cm^{-1} starts to appear, which can be assigned to CO linearly bonded to partially oxidized platinum ($\tilde{\nu}_{lin}^{CO}(Pt^{\delta+})$) and indicates the reduction of oxidized platinum by CO during the extinction.

At 81 °C, the CO_2 production is almost vanished. This extinction behavior signifies that partially oxidised platinum particles are the active phase for CO oxidation in the high activity region, which is in line with the previous studies [100, 101]. Continuing with the reference Pt/alumina sample, an obvious CO_2 formation with 100% CO conversion can be observed at 211 °C whereas no CO ad-species can be seen showing that the catalyst is exempt from CO poisoning. Upon decreasing temperature, a continuous decrease until 116 °C in the intensity of the $\tilde{\nu}_{gas}^{CO_2}$ band is seen before it drops. An abrupt change rather than a smooth decay in the intensity of $\tilde{\nu}_{gas}^{CO_2}$ band is observed, which is correlated with the sudden drop in CO_2 production. At 133 °C, from where the $\tilde{\nu}_{lin}^{CO}$ bands start to be discerned when there is CO_2 formation, which can be explained by the variety of Pt particle size associated with a different activity. Reaching 108 °C, the $\tilde{\nu}_{gas}^{CO_2}$ band becomes hardly visible, and the $\tilde{\nu}_{lin}^{CO}$ bands continue to grow as well as the $\tilde{\nu}_{br}^{CO}$ bands start to evolve. Simultaneously, the CO oxidation activity drops reflecting the Pt sites get CO self-poisoned. With a further decrease in temperature, three peaks at 2112, 2090, and 2069 cm^{-1} can be assigned to CO linearly adsorbed on ionic platinum ($\tilde{\nu}_{lin}^{CO}(Pt^{2+})$), partially oxidized platinum ($\tilde{\nu}_{lin}^{CO}(Pt^{\delta+})$) and metallic platinum ($\tilde{\nu}_{lin}^{CO}(Pt^{0})$), respectively. The peaks at 1881 and 1835 cm^{-1} are assigned to CO adsorbed on platinum particles in bridged configuration ($\tilde{\nu}_{br}^{CO}$). During the extinction, a red-shift of the $\tilde{\nu}_{lin}^{CO}(Pt^{0})$ band might be expected due to the reduction of oxidised platinum particles, however, this is not clearly observed as it can be counteracted by the blue-shift from increased CO coverage.

CO/H_2O oxidation

Moving to the CO/H_2O oxidation, an obvious $\tilde{\nu}_{gas}^{CO_2}$ band with around 29% CO_2 production is observed at 37 °C for Pt/ceria where the catalyst is circumvented from CO self-poisoning. Although a considerable CO_2 formation, $\tilde{\nu}_{lin}^{CO}(Pt^{\delta+})$ and $\tilde{\nu}_{lin}^{CO}(Pt^{0})$ band at 2081 and 2058 cm^{-1} can be clearly seen [54, 83]. However, the peak at 2081 cm^{-1} can also be ascribed to CO bonded to Pt kink sites surrounded with OH ($\tilde{\nu}_{lin}^{CO}(Pt(OH))$ for Pt/alumina [102], and this band appears to be active for low-temperature CO/H_2O oxidation. Although unlikely, this band has been shown to be CO bonded to Ce^{3+} on hydroxylated CeO_2 for single-atom Au on ceria [103], as CO binds strongly to Pt and a fast O_2 replenishment would be expected for the oxygen vacancies [104, 105]. A minor peak at 1832 cm^{-1} is assignable to bridge-bonded CO on larger platinum particles ($\tilde{\nu}_{br}^{CO}$). During the ignition, the intensity of the $\tilde{\nu}_{gas}^{CO_2}$ band continuously grows whereas the $\tilde{\nu}_{lin}^{CO}(Pt^{0})$ band starts to disappear and almost vanish at 125 °C. $\tilde{\nu}_{lin}^{CO}(Pt^{0})$ has been shown to be active species for dry CO oxidation [106]. At 134 °C, a roughly 10 cm^{-1}

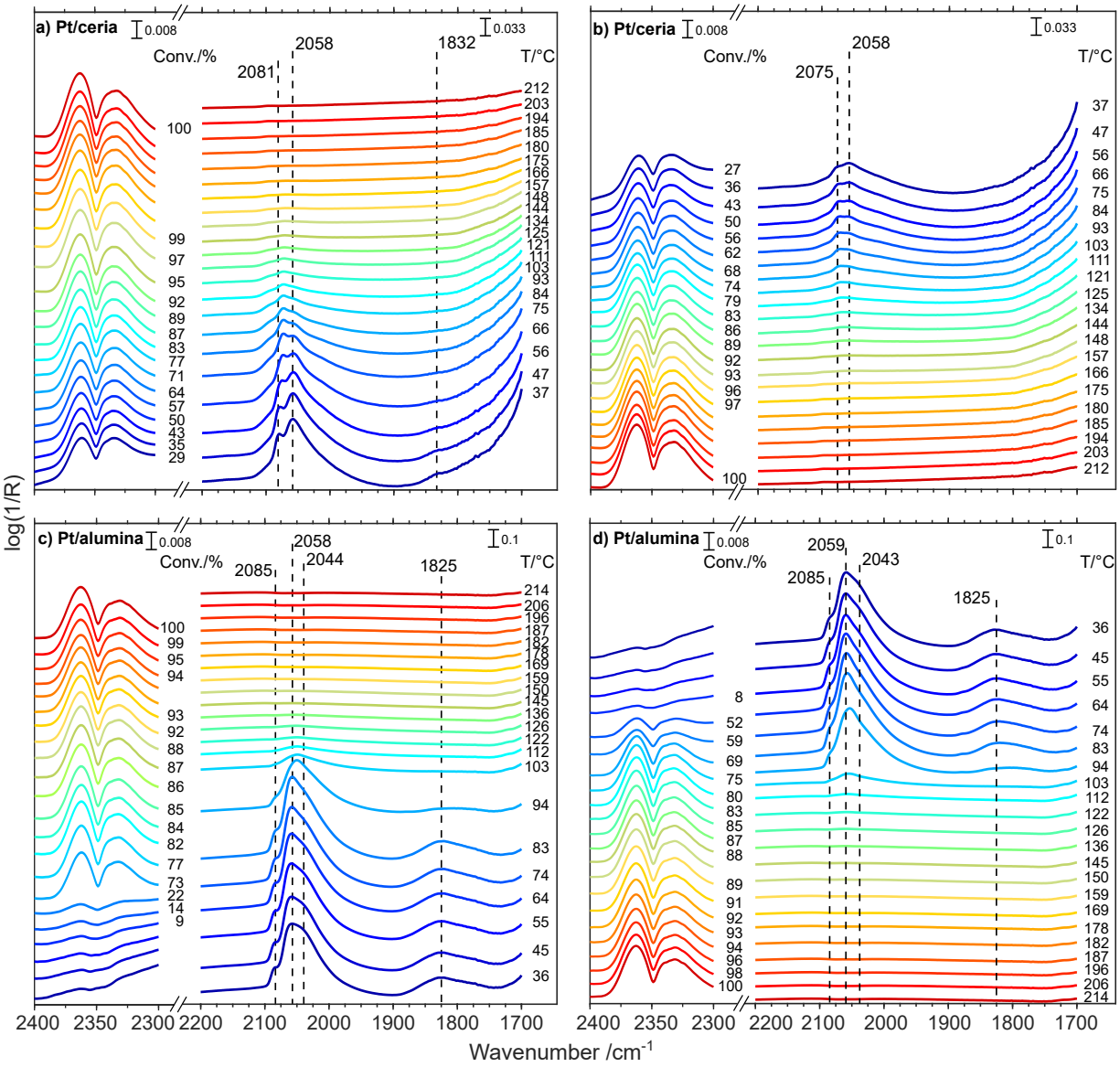

Figure 4.8: *In situ* infrared difference spectra (hydrogen treated sample as reference) collected at indicated sample temperatures while increasing (panel a and c) and decreasing (panel b and d) the sample temperature in steps in the presence of 0.2 vol.% CO, 1 vol.% O_2 and 2 vol.% H_2O (Ar as balance). The measured global CO conversion is indicated at each temperature.

red-shift can be observed for the 2081 cm^{-1} peak. This is partly due to an increased electron donation from Pt to the $2\pi^*$ orbital of adsorbed CO, and partly because of a less dipole-dipole coupling with decreased CO coverage [107]. Reaching 157 °C, the CO adspecies are hardly visible with 100% CO conversion. During the extinction, the intensity of $\tilde{\nu}_{gas}^{CO_2}$ gradually decreases. At 125 °C, the $\tilde{\nu}_{lin}^{CO}(Pt^{\delta+})$ and/or $\tilde{\nu}_{lin}^{CO}(Pt(OH))$ band start to evolve. Reaching 103 °C, a shoulder at 2058 cm^{-1} starts to appear. At 37 °C, a red-shift of 6 cm^{-1} is observed for the $\tilde{\nu}_{lin}^{CO}(Pt^{\delta+})$ and/or $\tilde{\nu}_{lin}^{CO}(Pt(OH)$ band coming from CO coverage effect. A red-shift but to a different extent obtained during ignition and extinction might be a result of a slower CO coverage build-up for extinction, which might be

associated with H_2O and OH coverage. Interestingly, there is no shift for the $\tilde{\nu}_{lin}^{CO}(Pt^0)$ band during the extinction. This signifies some CO ad-species on Pt could be isolated by H_2O and/or OH [108]. For the Pt/alumina catalyst, no $\tilde{\nu}_{gas}^{CO_2}$ band is observed at 36 °C whereas CO ad-species are clearly noticed in Figure 4.8 panel c when the catalyst is CO self-poisoned. Analogous to Pt/ceria, the peak at 2085 cm^{-1} could be assigned to $\tilde{\nu}_{lin}^{CO}(Pt^{\delta+})$ or $\tilde{\nu}_{lin}^{CO}(Pt(OH))$, and the peaks at 2058 and 2044 cm^{-1} are assigned to $\tilde{\nu}_{lin}^{CO}(Pt^0)$ [86, 109, 110]. More evident $\tilde{\nu}_{lin}^{CO}(Pt^0)$ bands indicate a less strong support effect in comparison with ceria. The peak at 1825 cm^{-1} is assigned to $\tilde{\nu}_{br}^{CO}$ [26]. During the ignition, an evident $\tilde{\nu}_{gas}^{CO_2}$ band is suddenly noted at 94 °C. This abrupt intensity change in $\tilde{\nu}_{lin}^{CO}$ and $\tilde{\nu}_{br}^{CO}$ bands is associated with the sudden change in CO_2 production showing catalyst starts to be free from CO poisoning. Simultaneously, the $\tilde{\nu}_{lin}^{CO}(Pt^0)$ band red-shifts by 7 cm^{-1}. At 103 °C, the $\tilde{\nu}_{br}^{CO}$ band is hardly visible, and minor $\tilde{\nu}_{lin}^{CO}(Pt^0)$ bands are discernible, which reflect the particle size effect on the activity for CO oxidation. Reaching 136 °C, hardly any CO ad-species are visible and the Pt sites are free from CO poisoning. During the extinction, the $\tilde{\nu}_{gas}^{CO_2}$ band reaches the maximum intensity until 103 °C from where it drops and $\tilde{\nu}_{lin}^{CO}$ bands start to evolve. A considerable decrease in CO_2 production at 83 °C is associated with the intensity increase of the $\tilde{\nu}_{lin}^{CO}$ and $\tilde{\nu}_{br}^{CO}$ bands. At 64 °C, the $\tilde{\nu}_{gas}^{CO_2}$ band is almost vanished whereas the $\tilde{\nu}_{lin}^{CO}(Pt^0)$ bands become even stronger. During the extinction, one would expect a red-shift of the bands for CO ad-species due to the reduction of oxidised Pt particles. However, this can be seen at 94 °C for the $\tilde{\nu}_{lin}^{CO}(Pt^0)$ band with a red-shift of 1-2 cm^{-1}. This band is further blue-shifted by 5 cm^{-1} due to increased CO coverage. A comparison between dry CO oxidation and CO/H_2O oxidation is made to explore the H_2O influence based on unaffected extinction coefficients of CO ad-species for these two reactions [111]. Compared to dry CO oxidation, the absorption peaks for adsorbed CO over Pt/ceria red-shifts from 2107 to 2075 cm^{-1} by 32 cm^{-1} and from 2078 to 2058 cm^{-1} by 20 cm^{-1} together with intensity transfer from high to low wavenumber. This is in line with the observations in literature [112, 113]. A likely explanation is an increased $2\pi^*$ back donation from Pt to CO coming from an increased electron density of Pt, which is caused by a less metal-support interaction due to the presence of H_2O/OH species on ceria [113]. Moreover, the co-adsorption between H_2O/OH species and CO on Pt can weaken the binding between CO and Pt [103]. Analogously, the absorption band for CO ad-species in atop for Pt/alumina red-shifts by 20-30 cm^{-1} but a lower linear to bridge ratio as compared to Pt/ceria. This can be explained by the difference in particle size between the two samples. Additionally, the bands for CO ad-species in bridged configuration red-shift 10 cm^{-1} since H_2O/OH species is co-adsorbed in an opposite-

pointing dipole configuration. However, it appears to be less energetically favorable due to a larger induced dipole for bridged CO adsorption.

CO/NO oxidation

The CO/NO oxidation over Pt/ceria and Pt/alumina is first investigated by time-resolved spectra at 35 °C in Figure 4.9 panel a and b. Starting from Pt/ceria, CO ad-species at 2104 and 2090 cm^{-1} are assigned to $\tilde{\nu}_{lin}^{CO}(Pt^{2+})$ and $\tilde{\nu}_{lin}^{CO}(Pt^{\delta+})$. With increasing time, the $\tilde{\nu}_{lin}^{CO}(Pt^{2+})$ band is blue-shifted by 25 cm^{-1} as well as an intensity transfer from low to high wavenumber indicating that oxidized platinum particles are formed in the presence of NO already at 35 °C. A possible explanation is that nitrate species formed from NO/NO_2 at around the platinum-support boundary sites, thus taking the electrons from Pt. A less likely is that the produced NO_2 as a strong oxidant can adsorb molecularly and subsequently dissociate [114] with oxidation and reduction of NO_x at the same time. Although unlikely under oxygen access conditions, the surface platinum oxides can be formed by a direct NO dissociation on Pt [115, 116] . Table 4.3 displays a summary of the peaks at lower wavenumbers based on the literature. However, some peaks are still not straightforward to assign. At the beginning, the peaks at 1606, 1393, 1218, 1037, and 3617 cm^{-1} (not shown) are assigned to bridged hydrogen carbonate (br-(CO_2)OH) species adsorbed on ceria where the 1606 and 1393 cm^{-1} bands originate from the asymmetric stretch splitting ($\tilde{\nu}_{as}$) of CO_3^{2-} and 1037 cm^{-1} belongs to the symmetric stretch ($\tilde{\nu}_s$), while the bending (δ) and vibrational ($\tilde{\nu}$) modes of OH are at 1218 and 3617 cm^{-1} [82, 84]. At 30 min, the peak at 1186 cm^{-1} starts to evolve, which could be nitroxyl anion (NO^-) or $\tilde{\nu}_{as}$ of bidentate chelating nitrite (b-NO_2) adsorbed on ceria as they are not spectroscopically distinguishable [117]. The corresponding $\tilde{\nu}_s$ band can be masked by adsorbed nitrate and carbonate species. However, the presence of the combination band of $\tilde{\nu}_{as}$ and $\tilde{\nu}_s$ at 2477 cm^{-1} signifies the existence of b-NO_2. Simultaneously, two weak bands appears at 1361 and 1058 cm^{-1} attributed to the *cis*-hyponitrite (*cis*-$N_2O_2^{2-}$). New peaks show up at the expense of the disappearance of *cis*-$N_2O_2^{2-}$ band. After two hrs, the maxima of new peaks reach at 1605, 1591, 1581, 1551, 1475, 1433, 1322, 1276, 1240, 1212, 1033 and 1010 cm^{-1}. Among those, peaks at 1605 and 1322 cm^{-1} can possibly be due to adsorbed NO_2 due to a fast disappearance after the increasing temperature in Figure 4.9 panel c. The peaks at 1591, 1212, and 1010 cm^{-1} belong to the bridged nitrate (br-NO_3) adsorbed on the ceria. The assignment for the peak at 1433 cm^{-1} is not straightforward. One possibility is polydentate (p-NO_3) or water-solvated nitrate (NO_3(OH)) as well as the

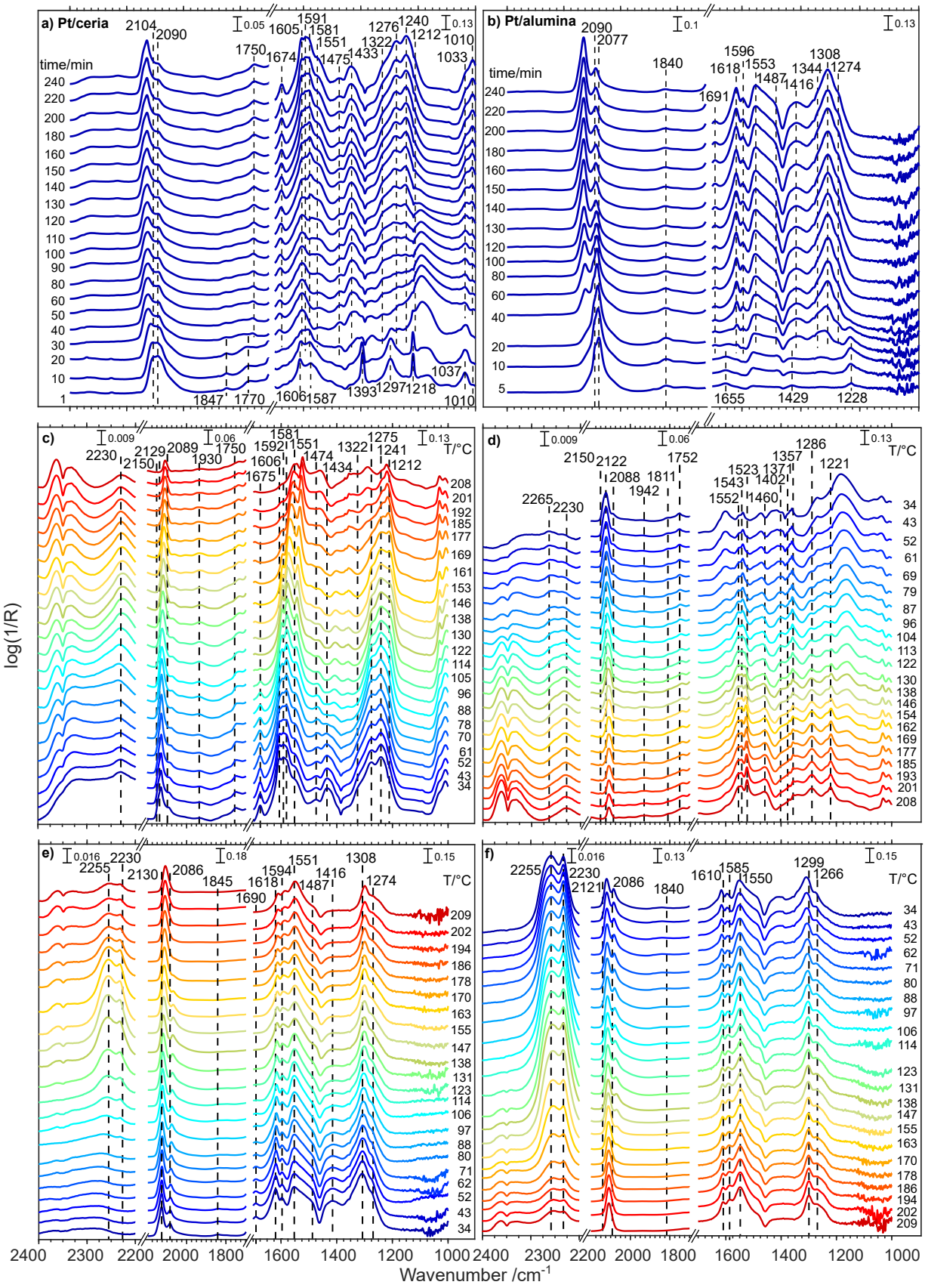

Figure 4.9: CO oxidation with NO from Pt/ceria (panel a) and Pt/alumina (panel b) at 35 °C with time-resolved spectral region for CO adsorbed on Pt and nitrates/carbonates. This is followed by increasing (panel a and c) and decreasing (panel b and d) the sample temperature in steps in the presence of 0.2 vol.% CO, 1 vol.% O_2 and 300 ppm NO Ar as balance).

Table 4.3: Assignment of Species in wavenumber range of 1000-2200 cm^{-1} the over Pt/ceria and Pt/alumina during CO/NO oxidation

Wavenumber /cm^{-1}	Assignment	Species	Notation	Reference
2112,2107,2104	linear CO adsorbed on oxidic Pt	lin-CO-Pt^{2+}	$\tilde{\nu}$(CO)	[54, 86, 110, 118]
2090,2081,2078	linear CO adsorbed on partially oxidized Pt	lin-CO-$Pt^{\delta+}$	$\tilde{\nu}$(CO)	[83, 86, 110, 118]
2069,2058	linear CO adsorbed on metallic Pt	lin-CO-Pt^{0}	$\tilde{\nu}$(CO)	[86, 110, 118]
1843,1832	bridge CO adsorbed on Pt	br-CO	$\tilde{\nu}$(CO)	[26]
1930	CO adsorbed on interface site linear NO adsorbed on oxidized Pt	CO-Pt(Ce^{3+}) NO-Pt^{2+}	$\tilde{\nu}$(CO),$\tilde{\nu}$(NO)	[83, 119]
1750	linear NO adsorbed on metaillic Pt	lin-NO-Pt^{0}	$\tilde{\nu}$(NO)	[119]
1675,1691	bridged NO adsorbed on metallic Pt	br-NO-Pt^{0}	$\tilde{\nu}$(NO)	[120, 121]
1606,1393,1037	bridged hydrogen carbonate on ceria	br-(CO_2)OH	$\tilde{\nu}_{as}(CO_3^{2-})$ splitting, $\tilde{\nu}_s(CO_3^{2-})$	[82, 84]
1587,1297,1010	bidentate carbonate on ceria	b-CO_3	$\tilde{\nu}_{as}(CO_3^{2-})$ splitting, $\tilde{\nu}_s(CO_3^{2-})$	[122]
1218,3617	bridged hydrogen carbonate on ceria	br-(CO_2)OH	δ(OH),$\tilde{\nu}$(OH)	[82, 84]
1186	nitrosyl anion on ceria	NO^-	$\tilde{\nu}$(NO)	[123, 124]
1361,1058	*cis* -hyponitrite on ceria	*cis* -N_2O_2	$\tilde{\nu}$(N=N), $\tilde{\nu}$(NO)	[124, 125]
1605,1322	gaseous or weakly adsorbed NO_2 on ceria	NO_2	$\tilde{\nu}_{as}$(NO),$\tilde{\nu}_s$(NO)	[125]
1591,1212,1010	bridged nitrate on ceria	br-NO_3	$\tilde{\nu}_{as}(NO_3^{2-})$ splitting, $\tilde{\nu}_s(NO_3^{2-})$	[85, 87]
1581,1240,1033	bidentate nitrate on ceria	b-NO_3	$\tilde{\nu}_{as}(NO_3^{2-})$ splitting, $\tilde{\nu}_s(NO_3^{2-})$	[85, 87]
1551,1276,1010	monodentate nitrate on ceria	m-NO_3	$\tilde{\nu}_{as}(NO_3^{2-})$ splitting, $\tilde{\nu}_s(NO_3^{2-})$	[85, 87]
1433, 1322	polydentate nitrate/ water-solvated nitrate nitro compound/*trans*-hoponitrite on ceria	p-NO_3/ NO_3^-(OH) NO_2/ *trans*-N_2O_2	$\tilde{\nu}_{as}(NO_3^{2-})$ splitting/$\tilde{\nu}_{as}(NO_3^{2-})$ splitting $\tilde{\nu}_{as}$(NO),$\tilde{\nu}_s$(NO)/$\tilde{\nu}$(N=N)	[87, 125, 126]
1475,1033	monodentate nitrite/polydentate carbonate on ceria	m-NO_2/p-CO_3	$\tilde{\nu}$(N=N),$\tilde{\nu}$(NO),$\tilde{\nu}$(C=O)	[122, 126]
1655,1228,(1429)	bridged carbonate/bridged hydrogen carbonate on alumina	br-CO_3/br-(CO_2)OH	$\tilde{\nu}_{as}(CO_3^{2-})$ splitting/$\tilde{\nu}$(CO),δ(COH), $\tilde{\nu}_s(CO_3^{2-})$	[127]
1618,1274	bridged nitrate on alumina	br-NO_3	$\tilde{\nu}_{as}(NO_3^{2-})$ splitting	[127, 128]
1596,1308	bidentate nitrate on alumina	b-NO_3	$\tilde{\nu}_{as}(NO_3^{2-})$ splitting	[127, 128]
1553,1308	monodentate nitrate on alumina	m-NO_3	$\tilde{\nu}_{as}(NO_3^{2-})$ splitting	[127, 128]
1416, 1344	polydentate nitrate/ water-solvated nitrate nitro compound/*trans*-hoponitrite on alumina	p-NO_3/NO_3(OH) NO_2/ *trans*-$N_2O_2^{2-}$	$\tilde{\nu}_{as}(NO_3^{2-})$ splitting/$\tilde{\nu}_{as}(NO_3^{2-})$ splitting $\tilde{\nu}_{as}$(NO),$\tilde{\nu}_s$(NO)/$\tilde{\nu}$(N=N)	[87, 129]
1487	monodentate nitrite on alumina	m-NO_2	$\tilde{\nu}$(N=N)	[127, 128]
1738,1402,1220	bridged carbonate adsorbed on ceria	br-CO_3	$\tilde{\nu}_{as}(CO_3^{2-})$ splitting, $\tilde{\nu}_s(CO_3^{2-})$	[[81]]
1490,1371	monodentate carbonate adsorbed on ceria	m-CO_3	$\tilde{\nu}_{as}(CO_3^{2-})$ splitting	[82, 84]
1460,1357	polydentate carbonate adsorbed on ceria	p-CO_3	$\tilde{\nu}_{as}(CO_3^{2-})$ splitting	[122]
1544,1255	bidentate carbonate adsorbed on alumina	b-CO_3	$\tilde{\nu}_{as}(CO_3^{2-})$ splitting	[130]
1459,1352	polydentate carbonate adsorbed on alumina	p-CO_3	$\tilde{\nu}_{as}(CO_3^{2-})$ splitting	[130]

peak at 1322 cm^{-1}. Although less likely due to the presence of O_2, this could be nitro species (NO_2) adsorbed on ceria. This peak could also be $\tilde{\nu}_{as}$ of *trans*-hyponitrite. However, the absence of a $\tilde{\nu}_s$ band makes this assignment unlikely. A minor peak at 1475 cm^{-1} could be $\tilde{\nu}_{as}$ of monodentate nitrite (m-NO_2) together with peak at 1033 cm^{-1}. A more likely assignment is polydentate carbonate (p-CO_3), however, the splitting band might be too weak to observe. The peaks at 1750 and 1674 cm^{-1} are assigned to linear and bridged NO adsorbed on Pt ($\tilde{\nu}^{NO}_{lin}(Pt^0)$, $\tilde{\nu}^{NO}_{br}(Pt^0)$) [114]. A less likely possibility for the 1750 cm^{-1} band is $\tilde{\nu}_{as}$ of bridged carbonate (br-CO_3). However, the rest of the vibration modes are not observed. The minor peak at 1930 cm^{-1} could be either CO molecules adsorbed on the interface sites of Pt/ceria ($\tilde{\nu}^{CO}_{lin}$(Pt-Ce^{3+}) or NO adsorbed on oxidic platinum ($\tilde{\nu}^{NO}_{lin}(Pt^{2+})$) [83, 119]. Eventually, the ceria surface is mainly covered by nitrates. For the Pt/alumina catalyst, the peaks at 2077 and 2090 cm^{-1} are ascribed to $\tilde{\nu}^{CO}_{lin}(Pt^{\delta+})$. With increasing time, the $\tilde{\nu}^{CO}_{lin}(Pt^{\delta+})$ bands are shifted to 2088 and 2130 cm^{-1}, respectively. Analogously, the nitrate species prevail on the surface and continuously replace the carbonates, which are produced during pretreatment, and thereby more and more negative peaks show up. At 5 min, peaks at 1655 and 1228 cm^{-1} are assigned to br-CO_3 or bridged hydrogen carbonate (br-(CO_2)OH) with the peak at 1429 cm^{-1}. Reaching 40 min, nitrate species start to build up on the alumina surface and the detailed assignments are listed in Table 4.3.

Moving to the ignition of CO/NO oxidation for Pt/ceria in Figure 4.9 panel c, the $\tilde{\nu}_{CO_2}$ band is discernible at 52 °C and the peak at 2230 cm^{-1} is assigned to isocyanate ($\tilde{\nu}_{NCO}$) formed on Pt, which then spills over to ceria. Weakly adsorbed N_2O could also be possible, however, it is not expected to be seen at high temperatures [131]. The formation of adsorbed isocyanate requires the surface first to be covered by NO [132]. During the ignition, the intensity of the $\tilde{\nu}_{CO_2}$ and $\tilde{\nu}_{NCO}$ bands gradually grows until 130 °C. The $\tilde{\nu}_{NCO}$ band starts to desorb with elevated temperature. Simultaneously, the intensity of the $\tilde{\nu}^{CO}_{lin}(Pt^{2+})$ band increases until 88 °C and then starts to decay smoothly. The increased intensity can be caused by the sites for CO adsorption being partially blocked by NO as well as the reduction of oxidized platinum particles by CO, which leads to a red-shift. However, this can be compensated by the coverage effect. The carbonates species on ceria start to appear at 105 °C with the corresponding assignment in Table 4.3. The $\tilde{\nu}^{CO}_{lin}(Pt^{\delta+})$ band vanishes at 192 °C and the $\tilde{\nu}^{CO}_{lin}(Pt^{2+})$ band is still visible at 208 °C although some formation of CO_2 is observed. A minor peak at 2150 cm^{-1} can be assigned to CO bound to reduced ceria ($\tilde{\nu}_{CO}(Ce^{3+})$), which indicates that the ceria surface is covered by the nitrates hindering the O_2 replenishment. During the extinction, the intensity of the $\tilde{\nu}_{CO_2}$ band continuous to decrease whereas

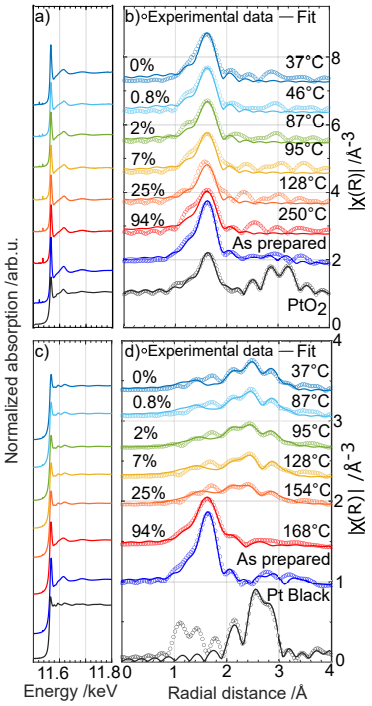

Figure 4.10: XANES spectra (panel a,c) and FT k^2-weighted EXAFS spectra with corresponding CO conversions (panel b,d) in the presence of 5 vol.% CO and 5 vol.% O_2. The spectrum for PtO_2 and Pt black were recorded *ex-situ* in ambient air at room temperature as a reference.

the $\tilde{\nu}_{NCO}$ band increases until 130 °C. The $\tilde{\nu}_{CO}(Ce^{3+})$ band grows until 162 °C from where it drops and almost disappears at 130 °C. This suggests that the formed isocyanate reacts with the lattice oxygen from ceria. With a further lowering in temperature, the $\tilde{\nu}_{NCO}$ band starts to disappear and is blue-shifted by 6 cm^{-1}. Whereas, the peak at 2253 cm^{-1} becomes evident with a blue-shift of 8 cm^{-1}. The intensity of the $\tilde{\nu}^{CO}_{lin}(Pt^{2+})$ band continuously increases and is blue-shifted by 14 cm^{-1}. The peak at 2086 cm^{-1} is blue-shifted by around 30 cm^{-1} showing more influence on larger particles. During the extinction in the low wavenumber regime, the intensity of the $\tilde{\nu}^{NO}_{br}(Pt^0)$ band gradually diminishes whereas the $\tilde{\nu}^{NO}_{br}(Pt^0)$ band increases with lowering the temperatures. During the ignition for Pt/alumina, the intensity of the $\tilde{\nu}^{CO}_{lin}(Pt^{2+})$ increases until 123 °C from where it decreases. The $\tilde{\nu}_{CO_2}$ band becomes visible at 131 °C. At 88 °C, a $\tilde{\nu}_{NCO}$ band shows up with increasing intensity until 138 °C. Meanwhile, both the $\tilde{\nu}^{NO}_{lin}(Pt^0)$ and $\tilde{\nu}^{NO}_{br}(Pt^0)$ bands vanish. The formed nitrate species gradually desorb with increasing temperatures and appear to be stable on alumina. Starting from 209 °C, the $\tilde{\nu}_{CO_2}$ and $\tilde{\nu}_{NCO}$ bands are noticeable. During the extinction, the intensity of the $\tilde{\nu}_{CO_2}$ band drops until 131 °C is reached where the intensity of the $\tilde{\nu}_{NCO}$ band is the highest. When the $\tilde{\nu}_{CO_2}$ band disappears at 114 °C, the intensity of the $\tilde{\nu}_{NCO}$ band starts to decrease marginally and stabilizes without any peak shift in comparison with ceria. The isocyanate species appear to be more stable on alumina than ceria. Upon decreasing temperature, the intensity of the $\tilde{\nu}^{CO}_{lin}(Pt^{2+})$ band continuously increases and the $\tilde{\nu}^{CO}_{lin}(Pt^{\delta+})$ band starts to evolve when 170 °C is reached. At 34 °C, the $\tilde{\nu}^{CO}_{lin}(Pt^{2+})$ and the $\tilde{\nu}^{CO}_{lin}(Pt^{\delta+})$ band is blue-shifted by around 11 and 20 cm^{-1}, respectively. In summary, competitive adsorption between CO and NO on Pt sites can clearly be revealed, and the support covered by nitrates and platinum particles are oxidized at 34 °C by the nitrates at the platinum-support boundary. Additionally, the production of CO_2 is correlated with the isocyanate formation.

4.3.2 Local structure and long-range order

Local structure

The local structure of Pt for Pt/ceria and Pt/alumina is investigated by XAS in Paper III. Looking at the XANES spectra of Pt/ceria in Figure 4.10 panel a and b, it is hard to observe any obvious changes in the intensity of Pt L_3 edge during the extinction. Therefore, looking at the FT k^2-weighted EXAFS spectra, an oxidised state of the Pt phase can be observed during the extinction, and a clear peak at 1.5–2 Å and a negligible peak at 2.5–3 Å can be assigned to Pt-O and Pt-Pt contribution, respectively. Platinum in the Pt/ceria

sample remains in an oxidised state even at 37 °C when there is barely CO conversion. The clear Pt-O coordination signifies the presence of highly dispersed platinum, including small Pt particles and possibly atomically dispersed Pt, which makes most of the Pt atoms bind to the oxygen from the support. Considering the intensity evolution of the Pt L_3 edge over Pt/alumina in Figure 4.10 panel c and d, an obvious decrease can be observed in WLI between 168 and 154 °C during the extinction. Likewise, the EXAFS spectra show a pronounced Pt-O contribution at 168 °C when a high CO conversion is achieved. Upon decreasing the temperatures, a noticeable Pt-Pt contribution shows up at the expense of the Pt-O contribution. Together with the DRIFTS spectra, the oxidised state of Pt at high temperature is due to the O_2 dissociation on Pt particles, and a reduction of platinum oxides can be caused by a preferential CO adsorption on Pt sites with decreasing temperature. The platinum oxide formation at high temperatures agrees with the classical Langmuir-Hinshelwood mechanism [26, 91]. However, the oxidised character at low CO conversions is likely due to the presence of smaller Pt particles in oxygen.

Furthermore, the WLI is plotted against temperature for Pt/ceria and Pt/alumina as shown in Figure 4.10 panel a. The WLI of Pt/ceria appears to be at a considerably high value. More specifically, it first drops from 1.85 to 1.7, then it remains until the reaction extincts and increases thereafter. The slight decrease provides the possibility to envisage the reaction between adsorbed CO and lattice oxygen from the ceria support in the vicinity of Pt particles. When the extinction occurs, the created oxygen vacancies in the ceria support are replenished by the gas phase O_2 at low temperatures [105]. From this explanation, the reactions at the platinum-ceria interface become possible at low temperatures from the interaction between ceria and Pt particles. For the Pt/alumina catalyst, the as-prepared sample exhibits the maximum WLI, and close to that of PtO_2. During reaction conditions, the WLI is always higher than that for Pt black and lower than PtO_2, and it decreases during extinction. The lowest WLI is slightly high than that of Pt black reflecting a small interaction from the alumina support. The influence caused by the supports on the Pt particles can be clearly revealed by looking at the local structure. The Pt-O and Pt-Pt coordination number (CN) and bond distance are plotted against temperatures for Pt/ceria and Pt/alumina as displayed in Figure 4.11 panel b and c. The Pt-O CN for Pt/ceria during the reaction exhibits the same trend as the WLI, which implies the Pt-O species mainly contribute to the changes of WLI. The Pt-O species are likely formed from the binding of lattice oxygen, thus creating a stable Pt-O structure, which gives a high Pt oxidation state. This can be further evidenced by the unaltered Pt-O distance of

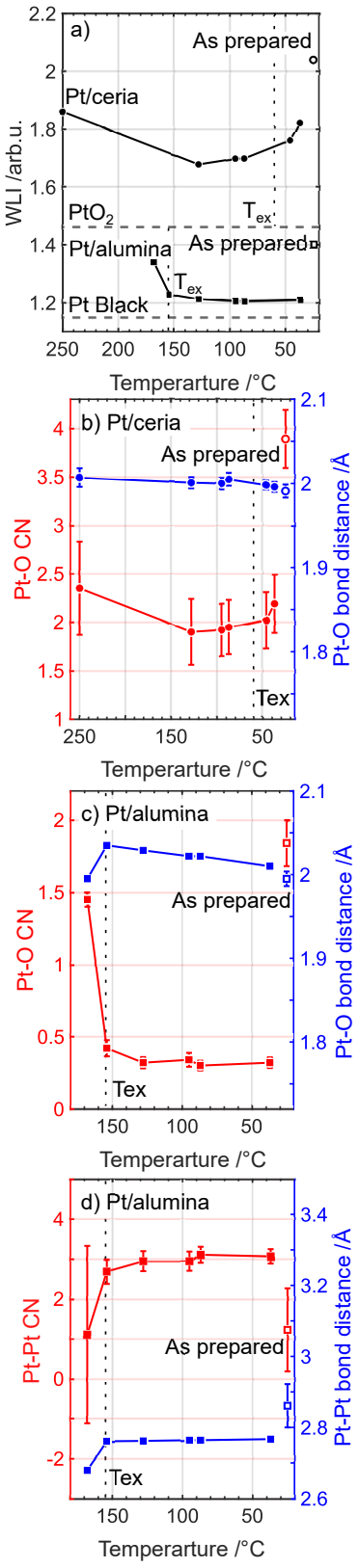

Figure 4.11: The whiteline intensity (WLI) for Pt/alumina and Pt/ceria (panel a) against temperature, coordination number (CN), and radial distance (R) without phase correction for Pt-O and Pt-Pt scattering of Pt/ceria (panel b) and Pt/alumina (panel c and d).

about 2 Å, which agrees with the studies of platinum nanoparticles dispersed on nanosized ceria [133]. The Pt-O distance becomes slightly longer at elevated temperatures, likely stemming from the thermal expansion. Moreover, the charge transfer from Pt particles to cerium supplemented with the lattice oxygen spillover to the vicinity of Pt has been proposed [84, 134], which gives an impact on the Pt oxidation state [135, 136]. These effects can be observed by XAS as a bulk averaging technique. Likewise, for the Pt/alumina catalyst, the trend of Pt-O CN is the same as that of WLI where the highest Pt-O CN is noticed at 168 °C and a low Pt-O CN is observed at lower temperatures during the reaction conditions. The Pt-O bond distance for the as-prepared Pt/alumina sample and during reaction conditions is shorter than that of PtO_2, which indicates a deformed platinum oxide [101]. On the contrary, the lowest Pt-Pt CN is obtained at 168 °C and a generally high Pt-Pt CN is noted at lower temperatures. Meanwhile, the Pt-Pt bond distance is close to that of Pt black and lower than the as-prepared sample.

Long-range order

The crystalline structure of 1 wt% Pt/maghemite and 1 wt% Pt/hematite are unraveled by *in-situ* HEXRD during redox reactions and CO oxidation in Paper V. The measurements are carried out during transient O_2 and H_2 pulses and O_2 modulation of CO. Figure 4.12 shows the time-resolved measurements during the periodic switch between 2 vol.% O_2 and 2 vol.% H_2 at 350 °C (panel a,b,e,f) and periodic change of 4 vol.% O_2 for 5 min with a constant flow of 1 vol.% CO at 350 °C (panel c,d,g,h) over Pt/maghemite and Pt/hematite, respectively. Each cycle is repeated five times. The difference diffractograms, after subtracting a reference diffractogram, e.g., the first one, are displayed to clearly distinguish the variations under different gas components. Some evident changes can be observed along the number of scans and selected diffractograms of the initial state (blue), under O_2 (green), and H_2 (red) are shown at the bottom. Among these, the reflection of around 3 $Å^{-1}$ is highlighted in the inset due to the possible reflection from the Pt crystal plane. The catalysts begin with a reduced state and are then under the gas sequences. From the difference diffractogram, an explicit increase in the peak intensity is depicted by blue color, whereas the red color describes a reduction in peak intensity in comparison with the first one. The appearance of the red and blue colors in pairs illustrates a peak shift towards a higher q (larger d spacing). This signifies the Fe seems to be in an oxidised state under O_2 since the Fe^{2+} has a larger ionic radius than Fe^{3+}. The diffractograms of the initial state and under H_2 resemble

the reference pattern of maghemite (00-065-0731), whereas the diffractogram under O_2 is a mixed phase of maghemite and hematite. Interestingly, a weak reflection is noticed at around q= 3.25 Å^{-1} for the reduced sample rather than the oxidised sample. This q value corresponds to a d spacing between the lattice planes of 1.93 Å, which is close to the interplanar distance of metallic Pt (200) planes of the FCC crystal structure (1.96 Å) [137]. The small discrepancy in q value is likely because of a strong metal-support interaction between the small Pt particles and the iron oxide support. Another possibility for the smaller d spacing is that some Fe atoms are incorporated in the Pt lattice structure. The absence of the Pt phase in the presence of O_2 can be caused by the sample being in an oxidised state. Shallow reflections would be expected from oxidised Pt crystal planes. Whereas, it can be difficult to observe any as they overlap with the iron oxide phase. Moving to the O_2 modulation, the difference diffractogram is obtained by subtracting the 500th diffractogram for better visualization. Weak changes in the peak position and intensity can be observed under the different gas environment. Since the sample begins with a reduced state, the first diffractogram closely resembles the reference pattern of maghemite as well as a weak and broad reflection likely from the Pt (200) crystal plane. The sample starts to be oxidised in the presence of both O_2 and CO, which can be evidenced by a clear peak shift to a higher q and the appearance of the hematite phase. However, it seems to be hard to reduce the sample back to the initial phase by solely CO than H_2. Some minor changes in peak position and peak intensity can be noticed between O_2 and CO pulses but this is not any significant phase change. Still, the diffractogram under O_2 is dominated by the maghemite phase and mixed with hematite phase. For Pt/hematite, a clear variation can be observed between the different gas components after subtracting the 500th diffractogram. The sample with a reduced state shows the peaks at 3.2 Å and 3.25 Å in addition to the major maghemite phase. The peak at 3.25 Å has previously been assigned to small platinum particles strongly influenced by the support. Nonetheless, the peak at 3.2 Å giving a d spacing is relatively closer to the interplanar distance of Pt (220), which signifies the presence of larger platinum particles that are less influenced by the iron oxide. One can speculate that platinum particles inside the iron oxide or the presence of large platinum particles could lead to this result. Analogously, the peak at 3.25 Å appears under H_2 and vanishes under O_2. In the presence of O_2, the diffractogram is still dominated by the maghemite phase with some peaks shifted to a higher q. Coming to the O_2 modulation, the difference diffractogram is obtained from subtracting the 1000th diffractogram. Some changes can be revealed with the periodic O_2 variation. During the whole modulation, the maghemite phase is the major phase in the diffractograms, and

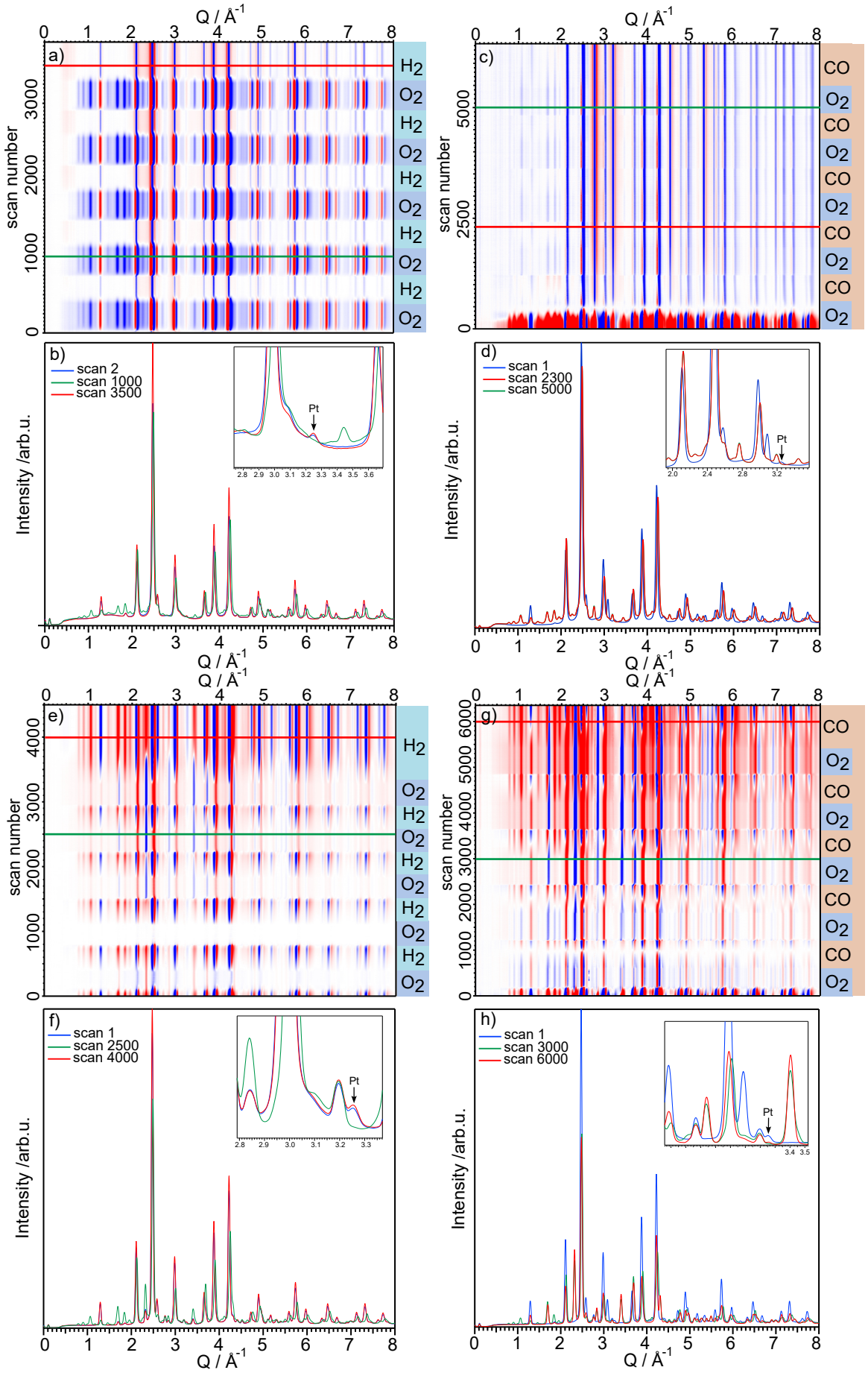

Figure 4.12: *in-situ* HEXRD of 2 vol.% O_2 and 2 vol.% H_2 pulsing at 350 °C (panel a,b,e,f), and O_2 modulation with 1 vol.% CO and 4 vol.% O_2 (panel c,d,g,h) over Pt/maghemite and Pt/hematite.

it tends to be oxidised under O_2 and CO environment. Likewise, the peak at 3.2 Å remains constant and the peak at 3.25 Å becomes more obvious when the sample is reduced.

4.4 How to design CO oxidation catalysts?

For CO oxidation, it is important to surpass the CO self-poisoning at low temperatures. This can be achieved in multiple ways, e.g., by using bimetallic or mixed metal oxide catalysts [138]. Our way is to employ a reducible support material to supply extra oxygen at low temperatures or even through other reaction pathways. As for the support material, it is crucial to have a sufficiently high surface area to achieve a high metal dispersion with low loading and proper thermal stability for the reaction. A metal-support interaction could also play a decisive role in stabilizing the metal particles, where the particle size can be further optimized for the catalytic activity through after-treatment. Also, electron transfer between the metal and the support could be significant for oxygen reverse spillover from the support to Pt. However, the metal-support interaction can not be too strong since the single platinum atoms or small platinum clusters strongly bound to the support seems to be spectators for CO oxidation. The strong metal-support interaction can be somehow weakened in the presence of H_2 at a proper temperature. From an economic and industrial consideration, the abundance of support material and the amount of precious metal in use, and the possibility of up-scaling need to be taken into account. In our specific case, iron oxides are selected as a candidate due to their redox properties, abundance, and low cost. The difficulty lies in their structure dynamics caused by the interaction between Pt and iron oxides and the complexity of the iron oxide phase during reaction conditions. On the other hand, the complexity seems to be appealing for the investigation of catalytic function, and further modification of the catalytic design.

5 Conclusions and future work

In this thesis, the reaction mechanism for CO oxidation over Pt/ceria and Pt/alumina is investigated. The chemical and structure dynamics under reaction conditions are explored for the catalysts. Furthermore, the influence of water and nitrogen oxide on CO oxidation is kinetically and spectroscopically scrutinized for Pt/ceria and Pt/alumina catalysts. In addition, the structural dynamics of Pt/FeO_x are examined under redox and reaction conditions. For the Pt/alumina catalyst with large Pt particles, in average 42 nm, the reaction order with respect to O_2 and CO is close to 1 and -1, respectively, under both lean and rich reaction conditions. For the Pt/alumina catalyst with small Pt particles, in average 2 nm, the corresponding reaction orders are 0.68 and -1 under lean conditions. For the latter catalyst, the reaction order for O_2 is 1 under rich conditions, which in part can be explained by higher O_2 conversion dominated by O_2 diffusion. The reaction orders obtained from micro-kinetic calculations lead to the conclusion that the reaction orders can not uniquely infer the reaction mechanisms. Moving to the Pt/ceria catalyst, both the experiments and calculations strongly support that the reaction proceeds via the Mars-van Krevelen mechanism with complementary reaction pathways on the boundary sites. The Pt/ceria catalyst has a size range of platinum particles of 1-2 nm, which is a norrower distribution than for Pt/alumina. CO oxidation under dry conditions over Pt/ceria shows a smooth decay in CO conversion, whereas a sudden drop is observed for Pt/alumina during extinction. Combining *operando* infrared and X-ray absorption spectroscopy, the $\tilde{\nu}_{lin}^{CO}(Pt^{2+})$ band for Pt/ceria signifies a spectator species, which is due to the strong bond between small platinum particles and ceria, and the Pt-O bond distance is unaltered during the catalytic extinction process. Furthermore, water promotes the catalytic activity of CO oxidation over both Pt/ceria and Pt/alumina through a Mars-van Krevelen mechanism and Langmuir-Hinshelwood mechanism, respectively. The hydroxyl groups formed at the interface sites of Pt/ceria seem to contribute to the low-temperature activity without any dependency on water concentration, and water and/or hydroxyl groups can significantly reduce CO bound to platinum particles. In contrast, the reaction rate is dependent on water concentration for Pt/alumina. Nitrogen oxide suppresses the CO oxidation over both catalysts by competitive adsorption with NO and the nitrate species on the support. The platinum particles already get oxidized at room temperature in the presence of nitrogen oxide and CO_2 production at high temperatures is associated with isocyanate species. In addition, different types of iron oxides are synthesized

and maghemite is selected to be the support due to proper surface area and thermal stability. The reduction by H_2 proceeds at lower temperature for Pt/maghemite than for Pt/hematite signifying a stronger interaction between Pt and the support for Pt/maghemite. For Pt/maghemite, high-energy X-ray diffraction shows a clear reflection for Pt under reducing conditions, which disappears under oxidizing environments. This suggests the presence of platinum particles significantly influenced by the reaction conditions. As for Pt/hematite, reflections from Pt are unaltered when changing gas environment from oxidising to reducing. This is suggested to be a result of different redox properties and inetraction with the platinum particles.

5.1 Extended understanding on industrial relevant catalysts

In this thesis, the assignment of spectator species of the platinum particles strongly bound to ceria needs further investigations, for example by using uniform single platinum atoms dispersed on ceria. Its catalytic function might be interesting to explore. The promotion effect from water has been clearly revealed over industrial relevant catalysts, Pt/ceria, and Pt/alumina, in this work. Whereas, the role of how water interacts with CO ad-species and the explicit reaction pathways are still unclear. These questions might be figured out by theoretical calculations in combination with experimental evidence. Experimentally, it might also be interesting to see how the evolution of Pt-O bond in the presence of water by *operando* XAS as compared to the dry CO oxidation. Definitely, other gas components, e.g., sulfur oxides, can also be included in the feed. Of course, a comprehensive comparison is desirable to make between Pt/ceria and Pd/ceria as three-way catalysts in the presence of a complex gas stream.

5.2 Further improvements in catalytic design

Iron oxides have been shown as an appealing but also challenging support material due to their abundance and redox properties, however, the complexity increased under the reaction conditions coming from the phase transition at relatively mild temperatures. To generalize this material to apply to More complicated catalytic screening is worth investigating with the help of computational modeling, e.g., platinum-iron and platinum-tin alloyed nanoparticles on reducible support materials.

Acknowledgements

This research was carried out at Competence Centre for Catalysis (KCK), and Division of Applied Chemistry, Chalmers University of Technology, Göteborg, Sweden. Part of research was performed at beamline P65 and P21.1 at PETRA III, Deutsches Elektronen-Synchrotron (DESY) in Hamburg, Germany, and at Chalmers Materials Analysis Laboratory (CMAL). The beamtime is much appreciated and special thanks for all the technical support.

This work is financially supported by the Swedish Energy Agency and the member companies: Johnson Matthey, Perstorp, Powercell, Preem, Scania CV, Umicore, and Volvo Group. First of all, I believe all the choices I made were the best at that moment. For this Ph.D. journey, I would also like to thank:

My main supervisor Per-Anders Carlsson for the effective support during my whole Ph.D. study. I appreciated the opportunities to learn XAS, microscopy techniques, and participation in the beamtimes. Thank you so much for helping me reach here to defend myself for the doctorate.

My co-supervisor Henrik Grönbeck, and examiner, Magnus Skoglundh, thank you for the stimulating discussions from different perspectives. Your dedication to science encourages me when I feel frustrated.

My collaborators, Noemi Bosio, Felix Hemmingsson, Andreas Schaefer, and Yanyue Feng. I enjoyed all the meetings and scientific discussions with all of you. Thank Noemi for such a great collaboration. Special thanks to Felix not only for building the setups but also the knowledge of the instruments. Thank Andreas for the effort in the measurements and the motivation for the work. I appreciated the company of Yanyue and Ghodsieh. I enjoyed the badminton after-work with David, Yingxin, Shivangi, and Alex. Thank David Thompsett and Tamsin Bell for all the constructive meetings, supportive input, and creative ideas for my research. Lasse Urholm and Lenart Norberg, a big thank you for all the maintenance of all the equipment. I would like to thank all my colleagues in the department: (in alphabet order) Carl-Robert, Chris, Guido, Peter, Radhika, Ting, Yifei, and Zhihang... I appreciated all the support from all my friends in life: Ace, Chunyan, Chi, Hao, Jieling, Jihao, Lisa, Naichen, Tingting, Wensi, Xiaoxi, Xingyun, Zhoutong, and Zhe...

Last but not the least, I would like to thank my boyfriend, Xiao, for your endless love and tolerance. I would like to express my sincerest gratitude to my mom for her constant support, love, and encouragement over the years. There is nowhere that can be called home without you.

Mengqiao Di, Göteborg, [March] 2023

Bibliography

[1] R. M. Heck, R. J. Farrauto, *Applied Catalysis A: General* **2001**, *221*, 443–457.

[2] M. Shelef, R. W. McCabe, *Catalysis Today* **2000**, *62*, 35–50.

[3] T. J. Crowley, *Science* **2000**, *289*.

[4] T. R. Karl, K. E. Trenberth, *Science* **2003**, *302*.

[5] H. Arakawa, M. Aresta, W. Armor, John N. Tumas, *Chemical Reviews* **2001**, *101*, 953–996.

[6] R. P. Turco, *Earth under siege: from air pollution to global change*, **1997**.

[7] Dieselnet, *Dieselnet* **2015**, 1.

[8] World Energy Outlook 2019 – Analysis - IEA.

[9] IEA, The future of trucks - Implications for energy and the environment. International Energy Agency (IEA), **2017**.

[10] I. Manisalidis, E. Stavropoulou, A. Stavropoulos, E. Bezirtzoglou, *Frontiers in Public Health* **2020**, *8*.

[11] G. Ertl, H. Knözinger, J. Weitkamp, *Handbook of Heterogeneous Catalysis*, *Vol. 1-5*, **2008**, pp. 1–2497.

[12] International Energy Agency (IEA), World Energy Outlook 2019 – Analysis - IEA, **2019**.

[13] news: European Commission proposes Euro 7/VII emission standards.

[14] I. Chorkendorff, J. W. Niemantsverdriet, *Concepts of Modern Catalysis and Kinetics* **2003**.

[15] M. Beller, A. Renken, R. A. van Santen, *Focus on Catalysts* **2012**, *2012*, 8.

[16] S. J. Green, *Industrial catalysis*, Macmillan Company, **1928**.

[17] J. Wisniak, *Educacion Quimica* **2010**, *21*, 60–69.

[18] S. A. Topham, *Chapter 1. The History of the Catalytic Synthesis of Ammonia*, **2022**.

[19] A. Mittasch, W. Frankenburg, *Advances in Catalysis* **1950**, *2*, 81–104.

[20] H. Heinemann, *Catalysis Reviews* **1981**, *23*, 315–328.

[21] G. C. Koltsakis, I. P. Kandylas, A. M. Stamatelos, *Chemical Engineering Communications* **1998**, *164*.

[22] H. S. Gandhi, G. W. Graham, R. W. McCabe, *Journal of Catalysis* **2003**, *216*, 433–442.

[23] T. R. Board, N. R. Council, *The Ongoing Challenge of Managing Carbon Monoxide Pollution in Fairbanks, Alaska*, National Academies Press, **2002**.

[24] P. G. Boulter, *Enviromental traffic management: A review of factors affecting cold-start emissions*, Transport Research Laboratory.

[25] R. L. BURWELL, **1977**, *8*, 1–55.

[26] P. Carlsson, L. Österlund, P. Thormählen, A. Palmqvist, E. Fridell, J. Jansson, M. Skoglundh, *Journal of Catalysis* **2004**, *226*, 422–434.

[27] A. T. Bell, *Science* **2003**, *299*, 1688–1691.

[28] I. Langmuir, *Trans. Faraday Soc.* **1922**, *17*.

[29] T. Engel, G. Ertl, *Advances in Catalysis* **1979**, *28*.

[30] Y. Y. Yeo, L. Vattuone, D. A. King, *Journal of Chemical Physics* **1997**, *106*, 392–401.

[31] W. A. Brown, R. Kose, D. A. King, *Chemical Reviews* **1998**, *98*.

[32] V. P. Zhdanov, B. Kasemo, *Surface Science Reports* **1997**, *29*.

[33] S. Johansson, L. Österlund, B. Kasemo, *Journal of Catalysis* **2001**, *201*.

[34] D. A. Frank-Kamenetskii, *Diffusion and heat transfer in chemical kinetics*, *Vol. p.487*, New York, **1969**.

[35] A. Schwartz, L. L. Holbrook, H. Wise, *Journal of Catalysis* **1971**, *21*, 199–207.

[36] P. A. Carlsson, M. Skoglundh, *Applied Catalysis B: Environmental* **2011**, *101*, 669–675.

[37] A. Trovarelli, *Catal. Rev.: Sci. Eng.* **1996**, *38*, 439–520.

[38] F. C. Meunier, D. Tibiletti, A. Goguet, D. Reid, R. Burch, *Appl. Catal. A* **2005**, *289*, 104–112.

[39] A. Bruix, J. A. Rodriguez, P. J. Ramírez, S. D. Senanayake, J. Evans, J. B. Park, D. Stacchiola, P. Liu, J. Hrbek, F. Illas, *J. Am. Chem. Soc.* **2012**, *134*, 8968–8974.

[40] Y. Lu, S. Zhou, C. T. Kuo, D. Kunwar, C. Thompson, A. S. Hoffman, A. Boubnov, S. Lin, A. K. Datye, H. Guo, A. M. Karim, *ACS Catal.* **2021**, *11*, 8701–8715.

[41] H. Wang, J.-X. Liu, L. F. Allard, S. Lee, J. Liu, H. Li, J. Wang, J. Wang, S. H. Oh, W. Li, M. Flytzani-Stephanopoulos, M. Shen, B. R. Goldsmith, M. Yang, *Nat. Commun.* **2019**, *10*, 1–12.

[42] A. M. Gänzler, M. Casapu, P. Vernoux, S. Loridant, F. J. Cadete Santos Aires, T. Epicier, B. Betz, R. Hoyer, J. D. Grunwaldt, *Angew. Chem. Int. Ed.* **2017**, *56*, 13078–13082.

[43] A. M. Gänzler, M. Casapu, F. Maurer, H. Störmer, D. Gerthsen, G. Ferré, P. Vernoux, B. Bornmann, R. Frahm, V. Murzin, M. Nachtegaal, M. Votsmeier, J.-D. Grunwaldt, *ACS Catal.* **2018**, *8*, 4800–4811.

[44] A. D. Allian, K. Takanabe, K. L. Fujdala, X. Hao, T. J. Truex, J. Cai, C. Buda, M. Neurock, E. Iglesia, *Journal of the American Chemical Society* **2011**, *133*, 4498–4517.

[45] R.H. Julian, *Focus on Catalysts* **2019**, *2019*, 7.

[46] H. H. Liu, Y. Wang, A. P. Jia, S. Y. Wang, M. F. Luo, J. Q. Lu, *Applied Surface Science* **2014**, *314*, 725–734.

[47] M. Cargnello, V. V. Doan-Nguyen, T. R. Gordon, R. E. Diaz, E. A. Stach, R. J. Gorte, P. Fornasiero, C. B. Murray, *Science* **2013**, *341*, 771–773.

[48] M. Zlokarnik, *Stirring: Theory and practice*, **2008**.

[49] H. Grönbeck, J. M. Thomas, *Chemical Physics Letters* **2007**, *443*.

[50] O. S. Bezkrovnyi, P. Kraszkiewicz, W. Mista, L. Kepinski, *Catalysis Letters* **2021**, *151*.

[51] Y. Chen, S. Lerch, Z. Say, C. Tiburski, C. Langhammer, K. Moth-Poulsen, *RSC Advances* **2021**, *11*, 11642–11650.

[52] K. Liu, A. Wang, T. Zhang, *ACS Catalysis* **2012**, *2*, 1165–1178.

[53] M. Ferrandon, *Department of chemical engineering and technology; Chemical reaction engineering* **2001**, *PhD*.

[54] L. Nie, D. Mei, H. Xiong, B. Peng, Z. Ren, X. I. P. Hernandez, A. DeLaRiva, M. Wang, M. H. Engelhard, L. Kovarik, A. K. Datye, Y. Wang, *Science* **2017**, *358*, 1419–1423.

[55] G. R. Hong, K. J. Kim, S. Y. Ahn, B. J. Kim, H. R. Park, Y. L. Lee, S. S. Lee, Y. Jeon, H. S. Roh, *Catalysts* **2022**, *12*, 1670.

[56] J. K. Aldridge, L. R. Smith, D. J. Morgan, A. F. Carley, M. Humphreys, M. J. Clarke, P. Wormald, S. H. Taylor, G. J. Hutchings, *Catalysts* **2020**, *10*, 1–15.

[57] N. M. Martin, M. Skoglundh, G. Smedler, A. Raj, D. Thompsett, P. Velin, F. J. Martinez-Casado, Z. Matej, O. Balmes, P. A. Carlsson, *Journal of Physical Chemistry C* **2017**, *121*.

[58] A. P. Jia, S. Y. Jiang, J. Q. Lu, M. F. Luo, *Journal of Physical Chemistry C* **2010**, *114*, 21605–21610.

[59] N. K. Soliman, *Journal of Materials Research and Technology* **2019**, *8*, 2395–2407.

[60] B. G. Krishna, G. S. Rathore, N. Shukla, S. Tiwari, *Perovskite solar cells: A review of architecture, processing methods, and future prospects*, Elsevier, **2020**, pp. 375–412.

[61] C. M. Kalamaras, S. Americanou, A. M. Efstathiou, *Journal of Catalysis* **2011**, *279*, 287–300.

[62] A. O. Dada, F. A. Adekola, E. O. Odebunmi, F. E. Dada, O. S. Bello, A. S. Ogunlaja, *MethodsX* **2020**, *7*, 100976.

[63] P. Velin, C. R. Florén, M. Skoglundh, A. Raj, D. Thompsett, G. Smedler, P. A. Carlsson, *Catalysis Science and Technology* **2020**, *10*.

[64] J. L. Hartley, *Review of Scientific Instruments* **1978**, *49*, 1647–1649.

[65] T. Huthwelker, V. Zelenay, M. Birrer, A. Krepelova, J. Raabe, G. Tzvetkov, M. G. Vernooij, M. Ammann, *Review of Scientific Instruments* **2010**, *81*.

[66] S. T. Kelly, P. Nigge, S. Prakash, A. Laskin, B. Wang, T. Tyliszczak, S. R. Leone, M. K. Gilles, *Review of Scientific Instruments* **2013**, *84*.

[67] C. N. Millet, R. Chédotal, P. Da Costa, *Applied Catalysis B: Environmental* **2009**, *90*.

[68] P. Velin, U. Stenman, M. Skoglundh, P. A. Carlsson, *Review of Scientific Instruments* **2017**, *88*, 115102.

[69] C. Zhang, J. Gustafson, L. R. Merte, J. Evertsson, K. Norén, S. Carlson, H. Svensson, P. A. Carlsson, *Review of Scientific Instruments* **2015**, *86*.

[70] H. F. Scott, *Elements of chemical reaction engineering*, Prentice Hall, **2016**.

[71] J. Nilsson, P. A. Carlsson, N. M. Martin, E. C. Adams, G. Agostini, H. Grönbeck, M. Skoglundh, *Journal of Catalysis* **2017**, *356*, 237–245.

[72] J. Zou, C. Fan, X. Liu, *Langmuir* **2020**, *36*, 14656–14665.

[73] F. Ambroz, T. J. Macdonald, V. Martis, I. P. Parkin, *Small Methods* **2018**, *2*, 1800173.

[74] P. A. Webb, *MIC Technical Publications* **2003**, *13*, 1–4.

[75] J. I. Goldstein, D. E. Newbury, J. R. Michael, N. W. Ritchie, J. H. J. Scott, D. C. Joy, *Scanning electron microscopy and X-ray microanalysis*, Springer, **2017**.

[76] D. B. Williams, C. B. Carter, *Transmission Electron Microscopy*, Springer US, **2009**, pp. 3–22.

[77] H. P. Lehmann, X. Fuentes-Arderiu, L. F. Bertello, *Pure and Applied Chemistry* **1996**, *68*, 957–1000.

[78] I. Mills, R. Jones, *Vibrational Spectroscopy* **1990**, *1*.

[79] C. N. Banwell, C. N. Banwell, *Fundamentals of molecular spectroscopy*, McGraw-Hill, **1994**.

[80] D. G. Araiza, A. Gómez-Cortés, G. Díaz, *Catalysis Science and Technology* **2017**, *7*, 5224–5235.

[81] C. Li, Y. Sakata, T. Arai, K. Domen, K. I. Maruya, T. Onishi, *Journal of the Chemical Society Faraday Transactions 1: Physical Chemistry in Condensed Phases* **1989**, *85*, 929–943.

[82] C. Binet, M. Daturi, J. C. Lavalley, *Catalysis Today* **1999**, *50*, 207–225.

[83] P. Bazin, O. Saur, J. C. Lavalley, M. Daturi, G. Blanchard, *Physical Chemistry Chemical Physics* **2005**, *7*, 187–194.

[84] G. N. Vayssilov, Y. Lykhach, A. Migani, T. Staudt, G. P. Petrova, N. Tsud, T. Skála, A. Bruix, F. Illas, K. C. Prince, V. Matolín, K. M. Neyman, J. Libuda, *Nature Materials* **2011**, *10*, 310–315.

[85] M. Y. Mihaylov, V. R. Zdravkova, E. Z. Ivanova, H. A. Aleksandrov, P. S. Petkov, G. N. Vayssilov, K. I. Hadjiivanov, *Journal of Catalysis* **2021**, *394*, 245–258.

[86] J. Raskó, *Journal of Catalysis* **2003**, *217*, 478–486.

[87] K. Hadjiivanov, *Catalysis Letters* **2000**, *68*, 157–161.

[88] J. Farideh, *Structure of Hydrated Ions and Cyano Complexes by X-Ray Absorption Spectroscopy "Structure of Hydrated Ions and Cyano Complexes by X-Ray Absorption*, Prism 2000, **2000**.

[89] J. Resasco, L. DeRita, S. Dai, J. P. Chada, M. Xu, X. Yan, J. Finzel, S. Hanukovich, A. S. Hoffman, G. W. Graham et al., *Journal of the American Chemical Society* **2019**, *142*, 169–184.

[90] A. L. Patterson, *Journal of the American Chemical Society* **1955**, *77*, 2030–2031.

[91] P. A. Carlsson, V. P. Zhdanov, B. Kasemo, *Applied Surface Science* **2005**, *239*, 424–431.

[92] C. Wang, X. K. Gu, H. Yan, Y. Lin, J. Li, D. Liu, W. X. Li, J. Lu, *ACS Catalysis* **2017**, *7*, 887–891.

[93] Y. Wang, J. Ma, X. Wang, Z. Zhang, J. Zhao, J. Yan, Y. Du, H. Zhang, D. Ma, *ACS Catalysis* **2021**, *11*, 11820–11830.

[94] J. Saavedra, H. A. Doan, C. J. Pursell, L. C. Grabow, B. D. Chandler, *Science* **2014**, *345*, 1599–1602.

[95] X. Q. Gong, P. Hu, R. Raval, *Journal of Chemical Physics* **2003**, *119*, 6324–6334.

[96] H. Y. Su, M. M. Yang, X. H. Bao, W. X. Li, *Journal of Physical Chemistry C* **2008**, *112*, 17303–17310.

[97] F. C. Meunier, *J. Phys. Chem. C* **2021**, *125*, 21810–21823.

[98] M. Kottwitz, Y. Li, R. M. Palomino, Z. Liu, G. Wang, Q. Wu, J. Huang, J. Timoshenko, S. D. Senanayake, M. Balasubramanian, D. Lu, R. G. Nuzzo, A. I. Frenkel, *ACS Catalysis* **2019**, *9*, 8738–8748.

[99] F. Maurer, J. Jelic, J. Wang, A. Gänzler, P. Dolcet, C. Wöll, Y. Wang, F. Studt, M. Casapu, J. D. Grunwaldt, *Nat. Catal.* **2020**, *3*, 824–833.

[100] F. C. Meunier, L. Cardenas, H. Kaper, B. Smíd, M. Vorokhta, R. Grosjean, D. Aubert, K. Dembélé, T. Lunkenbein, *Angewandte Chemie International Edition* **2021**, *60*, 3799–3805.

[101] E. Alayon, J. Singh, M. Nachtegaal, M. Harfouche, J. A. van Bokhoven, *Journal of Catalysis* **2009**, *263*, 228–238.

[102] Y. Chen, Y. Feng, L. Li, J. Liu, X. Pan, W. Liu, F. Wei, Y. Cui, B. Qiao, X. Sun, X. Li, J. Lin, S. Lin, X. Wang, T. Zhang, *ACS Catalysis* **2020**, *10*, 8815–8824.

[103] S. Zhao, F. Chen, S. Duan, B. Shao, T. Li, H. Tang, Q. Lin, J. Zhang, L. Li, J. Huang, N. Bion, W. Liu, H. Sun, A. Q. Wang, M. Haruta, B. Qiao, J. Li, J. Liu, T. Zhang, *Nature Communications* **2019**, *10*, 1–9.

[104] N. Bosio, M. Di, M. Skoglundh, P. A. Carlsson, H. Grönbeck, *Journal of Physical Chemistry C* **2022**, *126*, 16164–16171.

[105] R. Kopelent, J. A. Van Bokhoven, J. Szlachetko, J. Edebeli, C. Paun, M. Nachtegaal, O. V. Safonova, *Angewandte Chemie - International Edition* **2015**, *54*, 8728–8731.

[106] K. Ding, A. Gulec, A. M. Johnson, N. M. Schweitzer, G. D. Stucky, L. D. Marks, P. C. Stair, *Science* **2015**, *350*, 189–192.

[107] F. Maugé, C. Binet, J. C. Lavalley, *Catalysis by Metals*, Springer Berlin Heidelberg, **1997**, pp. 1–17.

[108] N. Kizhakevariam, X. Jiang, M. J. Weaver, *The Journal of Chemical Physics* **1994**, *100*, 6750–6764.

[109] C. Lentz, S. P. Jand, J. Melke, C. Roth, P. Kaghazchi, *Journal of Molecular Catalysis A: Chemical* **2017**, *426*, 1–9.

[110] E. Becker, P. A. Carlsson, L. Kylhammar, M. A. Newton, M. Skoglundh, *Journal of Physical Chemistry C* **2011**, *115*, 944–951.

[111] A. Bourane, O. Dulaurent, D. Bianchi, *Langmuir* **2001**, *17*, 5496–5502.

[112] S. D. Ebbesen, B. L. Mojet, L. Lefferts, *Journal of Catalysis* **2007**, *246*, 66–73.

[113] P. V. Menacherry, G. L. Haller, *Catalysis Letters 1997 44:3* **1997**, *44*, 135–144.

[114] B. A. Morrow, R. A. McFarlane, L. E. Moran, *Journal of Physical Chemistry* **1985**, *89*, 77–80.

[115] Q. Ge, M. Neurock, *Journal of the American Chemical Society* **2004**, *126*, 1551–1559.

[116] M. A. Van Spronsen, J. W. Frenken, I. M. Groot, *Nature Communications 2017 8:1* **2017**, *8*, 1–7.

[117] M. Y. Mihaylov, E. Z. Ivanova, G. N. Vayssilov, K. I. Hadjiivanov, *Catalysis Today* **2020**, *357*, 613–620.

[118] N. M. Martin, M. Skoglundh, G. Smedler, A. Raj, D. Thompsett, P. Velin, F. J. Martinez-Casado, Z. Matej, O. Balmes, P.-A. Carlsson, *J. Phys. Chem. C* **2017**, *121*, 26321–26329.

[119] E. Ivanova, M. Mihaylov, F. Thibault-Starzyk, M. Daturi, K. Hadjiivanov, *Journal of Molecular Catalysis A: Chemical* **2007**, *274*, 179–184.

[120] B. Azambre, L. Zenboury, A. Koch, J. V. Weber, *Journal of Physical Chemistry C* **2009**, *113*, 13287–13299.

[121] S. H. Chien, M. C. Kuo, C. H. Lu, K. N. Lu, *Catalysis Today* **2004**, *97*, 121–127.

[122] F. Hemmingsson, A. Schaefer, M. Skoglundh, P. A. Carlsson, *Catalysts* **2020**, *10*.

[123] M. Y. Mihaylov, E. Z. Ivanova, G. N. Vayssilov, K. I. Hadjiivanov, *Catalysis Today* **2020**, *357*, 613–620.

[124] M. Y. Mihaylov, E. Z. Ivanova, H. A. Aleksandrov, P. S. Petkov, G. N. Vayssilov, K. I. Hadjiivanov, *Molecular Catalysis* **2018**, *451*, 114–124.

[125] G. Qi, R. T. Yang, R. Chang, *Applied Catalysis B: Environmental* **2004**, *51*, 93–106.

[126] L. Zhang, J. Pierce, V. L. Leung, D. Wang, W. S. Epling, *Journal of Physical Chemistry C* **2013**, *117*, 8282–8289.

[127] T. J. Toops, D. B. Smith, W. S. Epling, J. E. Parks, W. P. Partridge, *Applied Catalysis B: Environmental* **2005**, *58*, 255–264.

[128] B. Westerberg, E. Fridell, *Journal of Molecular Catalysis A: Chemical* **2001**, *165*, 249–263.

[129] A. Zecchina, *Spectrochimica Acta Part A: Molecular Spectroscopy* **1991**, *47*, 823–824.

[130] H. Du, C. T. Williams, A. D. Ebner, J. A. Ritter, *Chemistry of Materials* **2010**, *22*, 3519–3526.

[131] Z. M. El-Bahy, *Modern Research in Catalysis* **2013**, *02*, 136–147.

[132] R. L. Keiski, M. Härkönen, A. Lahti, T. Maunula, A. Savimäki, T. Slotte, *Studies in Surface Science and Catalysis* **1995**, *96*, 85–96.

[133] S. Gatla, D. Aubert, G. Agostini, O. Mathon, S. Pascarelli, T. Lunkenbein, M. G. Willinger, H. Kaper, *ACS Catal.* **2016**, *6*, 6151–6155.

[134] J. Ke, W. Zhu, Y. Jiang, R. Si, Y. J. Wang, S. C. Li, C. Jin, H. Liu, W. G. Song, C. H. Yan, Y. W. Zhang, *ACS Catal.* **2015**, *5*.

[135] Y. Lykhach, S. M. Kozlov, T. Skála, A. Tovt, V. Stetsovych, N. Tsud, F. Dvořák, V. Johánek, A. Neitzel, J. Mysliveček, S. Fabris, V. Matolín, K. M. Neyman, J. Libuda, *Nat. Mater.* **2015**, *15*, 284–288.

[136] M. Nolan, Y. Lykhach, N. Tsud, T. Skála, T. Staudt, K. C. Prince, V. Matolín, J. Libuda, *Phys. Chem. Chem. Phys.* **2012**, *14*, 1293–1301.

[137] Z. Huang, Y. Yao, Z. Pang, Y. Yuan, T. Li, K. He, X. Hu, J. Cheng, W. Yao, Y. Liu, A. Nie, S. Sharifi-Asl, M. Cheng, B. Song, K. Amine, J. Lu, T. Li, L. Hu, R. Shahbazian-Yassar, *Nature Communications* **2020**, *11*.

[138] W. Yu, M. D. Porosoff, J. G. Chen, *Chemical Reviews* **2012**, *112*, 5780–5817.